ABSTRACT

SONG, YU. Effects of Filter Structures on Particle Capturing and Dust Holding Capacity. (Under the direction of Dr. Eunkyoung Shim).

Carded/through-air and melt-blown nonwovens were produced to respectively prepare the coarse and fine filter media. Dynamic filtration properties of these fibrous nonwoven filter media were tested by loading standard dust particles. Filter samples loaded with particles were prepared and sent to the X-ray micro-computed tomographic (XMCT) scan for three-dimensional imaging. The image processing and image analysis method were developed to visualize and analyze both the filter structure and particle deposition distribution across the filter depth.

The clogging process of coarse nonwoven filter media is first reported. At the beginning of the depth filtration stage, most of the particles are captured by the top part. After that, particles are deposited everywhere across the whole filter depth. Unlike the particle deposition of fine filter media that follows the exponential decay across the filter depth reported in the literature, the clogging of coarse nonwoven filter media is first found in the bottom part and it follows a bottom-top clogging process inside the filter structure.

For melt-blown nonwoven filter media, the benefit of dynamic filtration efficiency during particle loading due to the increase in the basis weight cannot compensate the increase in resistance. A real fabric solidity can be obtained from XMCT imaging to overcome the underestimation of melt-blown nonwoven with textured structure. Despite the basis weight of melt-blown nonwoven filters deposited with the same mass of particles, most of the particles are captured by a top part with certain depth (around 250 μm in this study), and the rest part of the filter structure is not contributing to the mass capturing and filter lifetime. Besides, at the same ratio of filter depth, more particles are captured by the filter with a higher basis weight.

Effects of Filter Structures on Particle Capturing and Dust Holding Capacity

By
Yu Song

A dissertation submitted to the Graduate Faculty of
North Carolina State University
in partial fulfillment of the
requirements for the degree of
Doctor of Philosophy

Fiber and Polymer Science

Raleigh, North Carolina
2020

APPROVED BY:

_____	_____
Dr. Eunkyoung Shim Committee Chair	Dr. Benoît Mazé
_____	_____
Dr. Joel Pawlak	Dr. Behnam Pourdeyhimi

DEDICATION

To my beloved family （づ￣3￣）づ ╭❤️～

BIOGRAPHY

Yu Song was born on February 18th, 1993 in Peixian county, Xuzhou city, Jiangsu province, China (People's Republic of). Peixian is a small county with 1.3 million population, but 2.4 million staple yarn spindles and 0.4 million metric tons production capacity of viscose rayon yarns. Yu had a couple of family members working in spinning mills. With the early enlightenment of textiles from the local spinning industry, he joined Donghua University, which was China Textile University previously, in 2011 with a Textile Engineering major. Yu considered nonwovens as the future of the textile industry and he chose nonwovens as his undergraduate concentration. He joined the 3 + X program and started his graduate studies at NC State University in August 2014. He studied compact yarn spinning for his Masters' thesis under the direction of Dr. William Oxenham and received a Master of Science degree in Textile Engineering in May 2016. After summer, he continued his studies as a Ph.D. student. Supervised by Dr. Eunkyoung Shim (Textile Engineering, Chemistry and Science Department, College of Textiles), Yu received a Ph.D. degree in Fiber and Polymer Science. During his Ph.D. study, he also accomplished the Nonwoven Science and Technology certificate from the Nonwovens Institute and the Technology Entrepreneurship and Commercialization certificate from the Jenkins MBA, NC State University. After graduation, he returned to China and stayed in the nonwoven industry.

ACKNOWLEDGMENTS

A ‘thank you’ is not enough for my advisor, Dr. Eunkyoung Shim. Without her help, I might be somewhere else on the earth now, doing some boring things like selling yarns. Her supervision and guidance have been leading me to overcome those difficulties in research.

Many thanks to my committee members, Dr. Benoît Mazé, Dr. Joel Pawlak, and Dr. Behnam Pourdeyhimi for their generous help and guidance to this dissertation.

The methodology part of this work can be divided into two parts, particle loading, and imaging. For particle loading, I will never forget Dr. Loganathan Rangasamy, from whom I learned the biggest lesson in my Ph.D. Special thanks to Bruce Anderson who works as a fire captain and Amy Minton who is always nice and patient to my long-time test and stay in the lab. For imaging, I’d like to thank my previous roommate, Dr. Li Xi, for his guidance in using Avizo.

I’d like to express my acknowledgment to other employees from the Nonwoven Institute, who helped me with many things all these years. Thomas Daugherty, William Barnes, Angelo Corino, Mo Dunston, John Fry, Mike Haskins, Eric Lawrence, Bradley Scroggins, and Jimei Wang.

I’d also like to thank the lovely workmates from the Nonwovens Institute student group, especially my officemates, Mehran Jafari, Rahim Jindani, Rebecca Ruckdashel, Yang Yu, Lanjun Yin, Imon Khan, and Majid Johataei. Thanks for the precious memories that we share.

TABLE OF CONTENTS

LIST OF TABLES ix

LIST OF FIGURES x

Chapter 1. Introduction 1

1.1. Introduction 1

1.2. Problem statement 3

1.3. Research objectives 3

1.4. Dissertation overview 3

References 6

Chapter 2. Literature Review 7

2.1. Nonwoven structures 7

2.1.1. Carding/through air bonding technique 7

2.1.2. Meltblown technique 8

2.1.3. Nonwoven structural properties 8

2.2. Air filtration 9

2.2.1. Air filtration properties 9

2.2.2. Air filtration mechanisms 12

2.2.3. Filter clogging 13

2.3. Filter structure-filtration relationship 15

2.3.1. Effects of filter structure properties on filtration and particle loading behaviors 15

2.3.2. Effect of structural gradient on filtration and particle loading behaviors 16

2.4. Loaded filter structure characterization with imaging tools 17

2.4.1. 2D imaging: optical microscopy 18

2.4.2. 2D imaging: scanning electronic microscopy (SEM) 20
2.4.3. 3D imaging: digital volumetric imaging (DVI) 21
2.4.4. 3D imaging: X-ray micro-computed tomography (XMCT) 24
2.4.4.1. Basics of XMCT 24
2.4.4.2. Filter structure characterization with XMCT 27
2.4.4.3. Metal artifact 28
2.5. Image processing and image analysis 30
2.5.1. Image pre-processing 31
2.5.2. Segmentation 33
2.5.3. Skeletonization 35
References 37
Chapter 3. Structure Characterization of the Clogging Process of Coarse Fibrous Nonwoven Filter Media during Solid Particle Loading with X-ray Micro -Computed Tomography **43**
Abstract 43
3.1. Introduction 44
3.2. Materials and methods 47
3.2.1. Characterization of clean filter media 47
3.2.2. Loading filter media with standard solid particles 49
3.2.3. Imaging of clean and loaded filter media 51
3.2.3.1. Optical microscopy 51
3.2.3.2. X-ray micro-computed tomography 51
3.2.3.3. Image processing and image analysis 53

3.3. Results and discussion 55
3.3.1. Evolution of filtration properties during the particle loading process 55
3.3.2. Surface and cross-section observations of the filters at different clogged stages 56
3.3.3. 3D structure visualization of clean and loaded filter media 58
3.3.4. Fiber and particle solidity distribution analysis 59
3.3.5. Pore diameter distribution analysis 65
3.4. Conclusions 68
References 70
Chapter 4. Effect of Basis Weight of Meltblown Nonwoven Filter Media on Filtration Properties and Particle Deposition Distribution 73
Abstract 73
4.1. Introduction 74
4.2. Materials and methods 75
4.2.1. Meltblown filter media sample production 75
4.2.2. Filter media characterization 76
4.2.3. Particle loading process 77
4.2.4. 3D structure acquisition of particle-loaded melt-blown filter media 78
4.2.5. Image processing and 3D structure characterization 79
4.3. Results and discussion 81
4.3.1. Characterization of structure properties 81
4.3.2. Particle loading behaviors 83
4.3.3. 3D structure visualization of particle-loaded filters 85
4.3.4. Analysis of filter structures 87

4.3.5. Analysis of particle deposition distribution 90
4.4. Conclusions 91
References 93
Chapter 5. Effect of Fiber Diameter and Die-to-Collector Distance (DCD) on the Loading Behaviors of Meltblown Nonwoven Filter Media 95
Abstract 95
5.1. Introduction 95
5.2. Materials and methods 96
5.2.1. Meltblown filter media sample production 96
5.2.2. Filter media characterization 96
5.2.3. Particle loading process 97
5.3. Results and discussion 97
5.3.1. Effect of fiber diameter on particle loading behaviors 97
5.3.2. Effect of DCD on particle loading behaviors 100
5.4. Conclusions 102
References 103
Chapter 6. Overall Conclusions 104
Chapter 7. Future Recommendations 105
APPENDIX 106
Characterization of the Loading Behaviors of Gradient Filter with Multilayered Pre-Filters 107
Conclusions 111

LIST OF TABLES

Chapter 3

Table 3.1. Structure parameters of studied fibrous nonwoven coarse filter TA.....48

Table 3.2. Average fiber and particle solidity of clean and loaded filter media from XMCT images.....60

Table 3.3. Dimensionless time of loaded mass and particle solidity 63

Chapter 4

Table 4.1. Structure properties of melt-blown filter media with different basis weight.....82

Chapter 5

Table 5.1. Structure parameters of melt-blown filter media with different fiber diameter.....99

Table 5.2. Structure parameters of melt-blown filter media with different DCD 101

LIST OF FIGURES

Chapter 2

Figure.2.1. Schematics of (a) carding [2] and (b) through-air boding [3].....7

Figure.2.2. Schematic of the melt-blown process [4] 8

Figure.2.3. Schematic of air filtration mechanisms: inertial impaction, browning diffusion, interception and electrostatic [6].....12

Figure.2.4. Schematic of dendrite formation under solid aerosol loading [8].....14

Figure.2.5. An example of the evolution of filter clogging [9] 15

Figure.2.6. Example of filter structure gradient design [13] 17

Figure.2.7. Particle penetration profile of soda fluorescein particles inside the filter for two values of filtration time [11] 18

Figure.2.8. Example of imaging clogged filter structure using an optical microscope [22].....19

Figure.2.9. Example of imaging filter structures using SEM [11].....20

Figure.2.10. Example of imaging clogged filter structure using SEM (SEM/EDX):
(a) Illustration of the packing density measurement using SEM/EDX.
(b) mean particle penetration profile in the thickness of the flat filter and the pleated filter [23] 21

Figure.2.11. Schematic of the image capturing system of the DVI microimager® [24].....22

Figure.2.12. Exporting 2D sections [24].....23

Figure.2.13. Schematic of synchrotron X-ray micro-computed tomography (XMCT) system [31] 25

Figure.2.14. (a) The physical basis of transmission tomography inside a slice, (b) value of the mass attenuation coefficient for carbon and iron [30].....26

Figure.2.15. Gray values of particle penetration profile (black curve) and fitted exponential decay [38] 28
Figure.2.16. Medical CT image affected by the metal artifact [40] 29
Figure.2.17. Noise removal with a median filter: (a) original image, (b) image (a) with 10% of pixels randomly selected and set to black, and another 10% randomly selected and set to white, (c) result of median filtering using a 3*3 square region, (d) result of median filtering using a 5*5 octagonal region [47] 32
Figure.2.18. Combing erosion and dilation to produce an opening or a closing. Colors indicate pixels that are removed (magenta) or added (green) in each step [47] 33
Figure.2.19. Example of thresholding an image based on a peak in the histogram: (a) metal surface imaged in a microscope, (b) real-world photography of a 3D flower using ambient light [47] 34
Figure.2.20. Diagram of the skeleton of a feature with five endpoints (red), four nodes (blue), four terminal segments (yellow), four internal segments (green) [47] 35

Chapter 3

Figure.3.1. Equipment set-up for particle loading 50
Figure.3.2. Image processing and image analysis procedures of XMCT images 53
Figure.3.3. Evolution of filtration properties of filter media TA: (a) differential pressure vs. loaded mass, (b) number efficiency vs. loaded mass, (c) mass efficiency vs. loaded mass, (d) fractional efficiency vs. particle size 56
Figure.3.4. Optical microscopic images of studied filter media at different clogging stages for surface observation: (a) 10 Pa, (b) 30 Pa, (c) 50 Pa, (d) 100 Pa and cross-section observation: (e) 10 Pa, (f) 30 Pa, (g) 50 Pa and (h) 100 Pa 57

Figure.3.5. 3D structure visualization of clean and loaded filter media from XMCT images: (a) 7Pa-clean, (b) 10Pa-9.2g/m^2, (c) 30Pa-39.6g/m^2, (d) 50Pa-52.6g/m^2, and (e) 100 Pa-84.4g/m^2 58

Figure.3.6. Fiber solidity distribution through the filter depth of clean filter TA 59

Figure.3.7. Fiber and particle solidity distribution through filter depth of filter TA at different particle loading stages: (a) 10 Pa, (b) 30 Pa, (c) 50 Pa and (d) 100 Pa 62

Figure.3.8. Progress ratio of loaded mass and particle solidity 63

Figure.3.9. Evolution of particle solidity distribution through filter depth 65

Figure.3.10. Pore diameter distribution of clean filter media from (a) PMI liquid porosimetry (b) XMCT image analysis 66

Figure.3.11. (a) Average pore diameter and (b) ratio of average pore size change 68

Chapter 4

Figure.4.1. Equipment set-up for particle loading test 77

Figure.4.2. Image processing and image analysis procedures 81

Figure.4.3. Structure properties of melt-blown filter media with different structure compactness: (a) SEM image, (b) fiber diameter distribution, and (c) pore diameter distribution 83

Figure.4.4. Effect of structure compactness on particle loading behaviors. (a) differential pressure vs. loaded mass, (b) number efficiency vs. loaded mass (c) quality factor vs. loaded mass, and (d) dust holding capacity at the end 500 Pa differential pressure 85

Figure.4.5. 3D melt-blown nonwoven filter media structures respectively captured 5g/m^2 dust: (a) BW-100gsm, (b) BW-150gsm, and (c) BW-200gsm 86

Figure.4.6. Image processing approach to acquire an adjusted structure despite the original textured structure: (a) original 3D structure, (b) 1 of the 16 divided equal individual part, (c) individual part with the top section cropped, (d) individual part being shifted up. 87

Figure.4.7. Fiber solidity distribution across filter depth of (a) original structures from imaging, (b) reorganized structures from imaging. 88

Figure.4.8. Comparison of (a) filter thickness and (b) filter solidity based on experimental measurements, original imaging structures, and reorganized imaging structures.....89

Figure.4.9. Particle solidity distribution of melt-blown nonwoven filter media with different basis weight loaded with the same 5 g/m^2 dust particles. (a) Particle solidity distribution across filter depth, (b) cumulative particle solidity across filter depth, (c) particle solidity distribution across dimensionless filter depth, and (d) cumulative particle solidity across dimensionless filter depth 91

Chapter 5

Figure.5.1. SEM image and fiber diameter distribution of melt-blown filter media produced with (a), (b) 1,200 m^3/hr, and (c), (d) 1,900 m^3/hr airflow 98

Figure.5.2. Effect of fiber diameter on particle loading behaviors. (a) differential pressure vs. loaded mass, (b) number efficiency vs. loaded mass, (c) quality factor vs. loaded mass, and (d) dust holding capacity at the end of 500 Pa.....100

Figure.5.3. Effect of DCD on particle loading behaviors. (a) differential pressure vs. loaded mass, (b) number efficiency vs. loaded mass, (c) quality factor vs. loaded mass, and (d) dust holding capacity at the end 500 Pa.....102

Appendix

Figure.A.1. Comparison of the loading behaviors between single layer Pre-filter TA and Filter MB nonwoven filter media, (a) differential pressure vs. loaded mass, (b) number efficiency vs. loaded mass, (c) mass efficiency vs. loaded mass, (d) quality factor vs. loaded mass (based on number efficiency)..... 108

Figure.A.2. Loading behaviors of multilayered pre-filter TA, (a) differential pressure vs. loaded mass, (b) number efficiency vs. loaded mass, (c) mass efficiency vs. loaded mass, (d) quality factor vs. loaded mass (based on number efficiency) 109

Figure.A.3. Loading behaviors of gradient filters composted of multilayered pre-filter TA and one single layer of MB, (a) differential pressure vs. loaded mass, (b) number efficiency vs. loaded mass, (c) mass efficiency vs. loaded mass, (d) quality factor vs. loaded mass (based on number efficiency)..... 111

CHAPTER 1. Introduction

1.1. Introduction

Nonwoven air filters are widely used in various air filtration applications. A typical nonwoven air filter consists of a mat of fine fibers that captures small contaminants from the air stream when the air flows through the filter. As the contaminants are captured by the air filter during the filtration process and deposited in the filter structure, these contaminants will gradually reduce the openness of the filter and block the airflow. Eventually, reaching the maximum resistance leads to the end of the filter life.

Three typical filtration properties, filtration efficiency, pressure drop, and dust holding capacity, are used to evaluate the performance of air filter media. Filtration efficiency is the ratio of contaminants being captured. Pressure drop evaluates the resistance when the airflow exists. Dust holding capacity is referred to the weight of contaminants being captured at the extreme pressure drop when the resistance of the filter is too high to use.

One challenge for the nonwoven filter design is the contradiction among these filtration properties. It is well known in the filtration filed that the filtration efficiency could easily be improved by using fiber with a small diameter [1]. However, small fibers lead to a high initial pressure drop. Besides, filters with small fibers are also easy to be clogged during filtration, thus increasing the work pressure drop and reducing filter dust holding capacity, which leads to increased operational cost, such as high energy consumption and frequent filter replacement.

As a result, it would be ideal for the designing and engineering of the nonwoven air filter if the comprehensive filtration properties could be maximized at the same time. Then studying the

relationship between the filter structures and the filtration properties during the filtration or particle loading process becomes extremely important.

Studies proved that the filter structural properties such as fiber diameter [2], fiber orientation distribution [3], fiber solidity (solid volume fraction) [4]/ nonwoven porosity, and pore size [5] affect the filtration efficiency and pressure drop of the nonwoven filter media. However, these studies only focused on clean filters, and the evolution of filtration properties during the particle loading process was not reported. As the particles are captured and the filter gets clogged, the filter structural properties such as the effective fiber diameter, nonwoven porosity, and the pore size also change over time. The change in these structural properties affects the dynamic filtration properties in turn. Then obviously, the initial filtration efficiency and pressure drop cannot completely evaluate and predict the performance of a filter media through its lifetime. As a result, it is of great importance to study the effect of filter structures on the evolution of filtration properties during the particle loading process. However, limited studies have been done in this area.

One typical way applied by the industry to maximize the filtration efficiency and the dust holding capacity together is to utilize the structural gradient of different filters. For example, a coarse filter and a fine filter can be stacked to form a composite filter. In this case, the coarse filter layer offers limited efficiency and low pressure drop, but it can hold lots of particles due to its open structure. The fine filter layer enables the high filtration efficiency, but also high pressure drop and limited dust holding capacity. Overall, studies have proved that the comprehensive improvement of filtration properties can be realized by applying structural gradient [6]. However, the effect of structural gradient on filtration and particle loading behaviors is not yet fully discovered.

1.2. Problem statement

As stated in section 1.1, a contradiction exists among the three filtration properties, i.e. filtration efficiency, pressure drop, and dust holding capacity, that all these three filtrations properties cannot be maximized at the same time. It is ideal and desired by the industry to solve the following problem.

Problem statement: How 3D filter media structures influence all the filtration properties, in particular, dust loading behavior?

1.3. Research objectives

The main objective of this research is to investigate the relationship between filter structure properties and filtration properties during the air filtration process. Objectives of this study can be subcategorized into the following:

- Experimental study on the effects of nonwoven filter media structures on particle capturing and dust holding capacity.
- Structure characterization of nonwoven filter media loaded with particles based on the visualization and analysis from imaging.
- Study of the effect of the structural gradient on the filtration and particle loading behaviors.

1.4. Dissertation overview

This document introduces contents about this research in different chapters. Following is a brief overview of chapters included in this document.

Chapter 1: This chapter talks about an introduction to this research, the problem this research wants to solve and the research objectives of this research. It introduces the basic ideas and importance of the management of contradictory filtration properties during the filtration process.

Chapter 2: This chapter reviews the prior art. It introduces background knowledge of nonwoven structures and air filtration. It also reviews the filter structure-filtration property relationship during the filtration process. It further reviews some imaging tools to characterize the filter structures as wells as the frequently used methods regarding how to process and analyze the acquired images.

Chapter 3: This chapter discusses the structure characterization of particle-loaded carding/through-air nonwoven filter media at various clogging stages using optical microscope and X-ray micro-computed tomography, which refers to a part of the second research objective. The loaded filter structures were visualized and analyzed based on the acquired images. The fiber and particle solidity distribution profile across the filter depth and the pore diameter distribution of filters at different particle loading stages were discussed.

Chapter 4: This chapter introduces the effect of structure compactness of melt-blown nonwoven filter media on filtration properties and particle deposition. The structure compactness was controlled by changing the basis weight of melt-blown nonwovens. The filtration properties were characterized by particle loading experiments, and the particle deposition of filters with different structure compactness was investigated with X-ray microscopy.

Chapter 5: The effect of fiber diameter and die-to-collector distance (DCD) on the loading behaviors of melt-blown nonwoven filter media is discussed in this chapter.

Chapter 6: This chapter summaries the overall conclusions based on the above research chapters.

Chapter 7: This chapter includes recommendations for further research.

Appendix: Preliminary studies that cannot form complete stories are discussed in the Appendix instead of individual research chapters. It includes the characterization of the loading behaviors of gradient filter with multilayered pre-filters.

References

[1] Davies, C. N. (1973). Air filtration.

[2] Leung, W. W. F., Hung, C. H., & Yuen, P. T. (2009). Experimental investigation on continuous filtration of sub-micron aerosol by filter composed of dual-layers including a nanofiber layer. Aerosol Science and Technology, 43(12), 1174-1183.

[3] Fotovati, S., Tafreshi, H. V., & Pourdeyhimi, B. (2010). Influence of fiber orientation distribution on performance of aerosol filtration media. Chemical Engineering Science, 65(18), 5285-5293.

[4] Leung, W. W. F., Hung, C. H., & Yuen, P. T. (2010). Effect of face velocity, nanofiber packing density and thickness on filtration performance of filters with nanofibers coated on a substrate. Separation and purification technology, 71(1), 30-37.

[5] Liu, J., Zhang, X., Zhang, H., Zheng, L., Huang, C., Wu, H., ... & Jin, X. (2017). Low resistance bicomponent spunbond materials for fresh air filtration with ultra-high dust holding capacity. RSC Advances, 7(69), 43879-43887.

[6] Leung, W. W. F., & Hung, C. H. (2012). Skin effect in nanofiber filtration of submicron aerosols. Separation and Purification Technology, 92, 174-180.

CHAPTER 2. Literature Review

2.1. Nonwoven structures

2.1.1. Carding/through air bonding technique

Carding is a web formation process to individualize and parallelize the fibers [1]. Through-air bonding is a web bonding process to thermally bond the fibers by blowing hot air through the fiber web. The schematics of carding and through-air bonding can be found in Figure.2.1 a [2] and Figure.2.1 b [3] respectively. The carding process offers a broad range of selections for the final nonwoven structures, such as fiber diameter, fiber length, fiber blend ratio, nonwoven basis weight, etc. Since no significant pressure is applied during the through-air bonding process, the fabricated nonwoven retains a structure as loft as the fiber web.

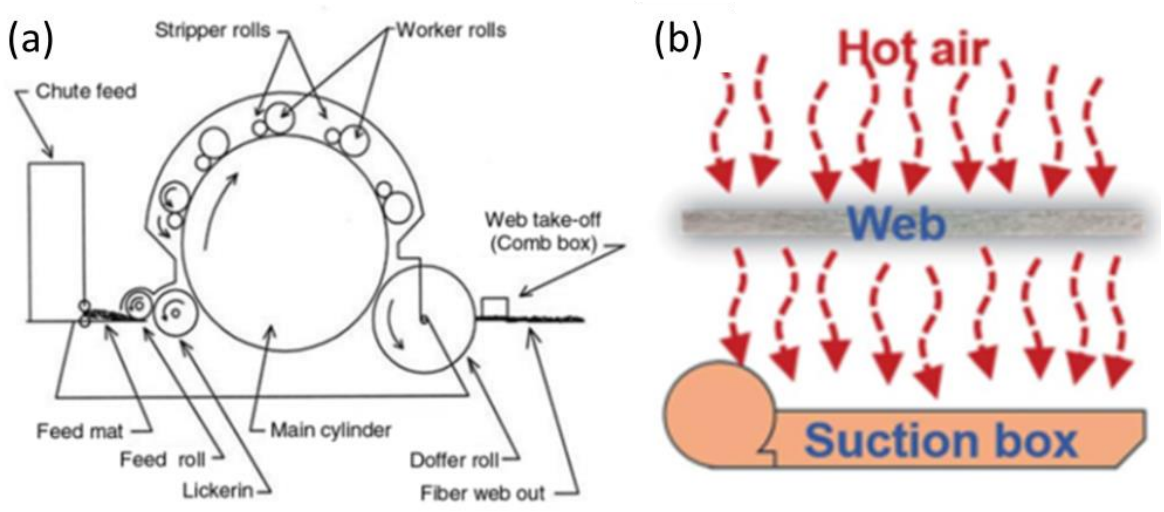

Figure.2.1. Schematics of (a) carding [2] and (b) through-air boding [3].

2.1.2. Melt-blown technique

Meltblown is a one-step process that can directly produce self-bonded nonwoven from polymer resin. The schematic of the melt-blown process is shown in Figure.2.2 [4]. This process produces fibers with diameters ranging between 0.1 to 1 micron [1], which makes the process widely used to produce high-efficiency filters. On the other hand, unlike the carding that requires a long time to produce nonwovens composed of different fiber diameters, the fiber diameter distribution, as well as other structure properties, can be easily changed in the melt-blown process by changing certain processing parameters. In this study, the melt-blown process has been applied to fabricate high efficiency fibrous nonwoven filter media and to investigate the effects of filter structures on particle loading behaviors.

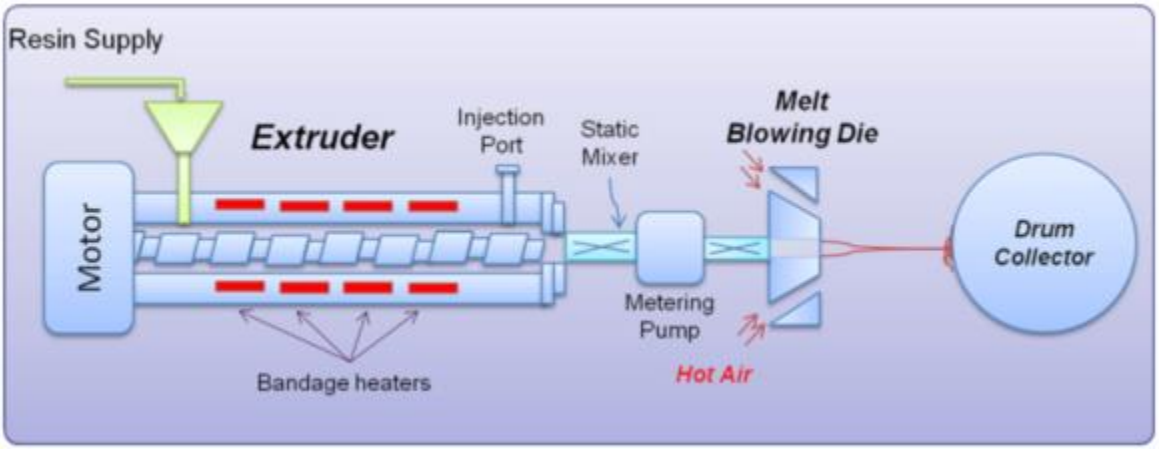

Figure.2.2. Schematic of the melt-blown process [4].

2.1.3. Nonwoven structural properties

Nonwovens are highly engineered fabrics that are made directly from polymer resins or staple fibers without any yarn structures involved (stitch bonding nonwoven is an exception). As a fiber

assembly, the nonwoven structural properties can be divided into fiber structural properties and nonwoven fabric structural properties.

Fiber structural properties include fiber length, fiber size/fiber diameter, fiber cross-section shape, etc. The fiber length of the commercial staple fibers used in the carding process is typically a fixed number with a small variation in distribution, while the fiber length of filaments in melt-blown nonwovens is almost infinite. The fiber diameter of commercial staple fibers is also a fixed number for each specific product type. The fiber diameter distribution of melt-blown filaments is determined by the melt-blown processing parameters, especially the airflow that draws the filaments. The fiber cross-section shape for both carding staple fibers and melt-blown filaments is considered as round or circle. Besides, it can also be trilobal, winged, hollow, etc. in other nonwoven forms and applications.

Nonwoven fabric structural properties include basis weight, thickness, fiber solidity, fiber orientation, pore size, pore tortuosity, etc. Basis weight is the mass per unit area. Fiber solidity, which is also considered as the fiber packing density or fiber solid volume fraction, refers to the ratio of fabric/nonwoven density over fiber density which can be used to evaluate the nonwoven compactness. Fiber orientation describes how fibers are aligned in direction. Pore tortuosity is used to define how tortuous the pores are.

2.2. Air filtration

2.2.1. Air filtration properties

As previously introduced in Chapter 1, there are three important filtration properties under the scope of this research: filtration efficiency, pressure drop and dust holding capacity. The

performance of these filtration properties during the particle loading process is referred to as the particle loading behaviors in this research.

The filtration efficiency evaluates the particle capturing ability of the filter media. It can be expressed as the ratio of the number of particles captured to the number of total particles. The equation of filtration efficiency, E, is shown in the following.

$$E = \frac{Nupstream - Ndownstream}{Nupstream}, \quad (2.1)$$

where $N_{upstream}$ is the total number of particles detected by the upstream sensor (before the test filter) and $N_{downstream}$ is the number of detected by the downstream sensor (after the test filter). In contrast, penetration is frequently used to represent the particle capturing performance of high-efficiency filter media [5]. The particle penetration, P, is shown in the following equation.

$$P = \frac{Ndownstream}{Nupstream} = 1 - E, \quad (2.2)$$

Pressure drop is used to quantify the resistance of airflow caused by the filter media. Higher pressure drop means high resistance and thus higher operational cost, e.g. energy consumption, which is not ideal for the application of filter media. Pressure drop, ΔP, is defined as the difference of upstream pressure (before the test filter) and downstream pressure (after the test filter), which is shown in the following equation.

$$\Delta P = Pupstream - Pdownstream, \quad (2.3)$$

Furthermore, the pressure drop can be obtained in the flowing equation as it obeys Darcy's law [6]:

$$\Delta P = 4\mu * V * h * f(\beta)/df2, \quad (2.4)$$

where μ is the fluid dynamic viscosity, V is the fluid velocity, h is the filter thickness, df is the fiber diameter, and f(β) is a function relates to the fiber solidity, β. One of the most popular expressions for f(β) was given by Davis [7]:

$f(\beta) = 16^* \beta^{1.5}*(1 + 56 \beta)$, for $0.006 < \beta < 0.6$, (2.5)

where the fiber solidity, β, falls into the range of most fibrous filter media.

The quality factor, QF, is an indicator that takes both the filtration efficiency and pressure drop into consideration to evaluate the performance of filter media. It is defined by the following equation [5]:

$$QF = \frac{-\ln(1-E)}{\Delta P}, \quad (2.6)$$

Dust holding capacity is used to evaluate the filter life or service time. It is defined as the cumulative collected mass of particles at a given pressure drop when the resistance of filter media is too high to use. Although the collected mass is good to represent the dust holding capacity of filter media at a specific point, it is difficult to measure in testing because of the low mass value of particles captured by a small area (100 cm^2) of the filter media sample. Besides, frequent mass measurement only brings additional error. Instead, the loaded mass can be very useful in terms of representing the particle loading behaviors, such as efficiency-loaded mass relationship and pressure drop-loaded mass relationship. Furthermore, the collected mass at the maximum pressure drop is ideal to represent the dust holding capacity of the filter media.

2.2.2. Air filtration mechanisms

The particle capturing mechanisms in air filtration can be classified into mechanical filtration and electrostatic attraction. The mechanical filtration further includes inertial impaction, browning diffusion (Brownian motion) and interception. A schematic for all these air filtration mechanisms is shown in Figure.2.3 [6].

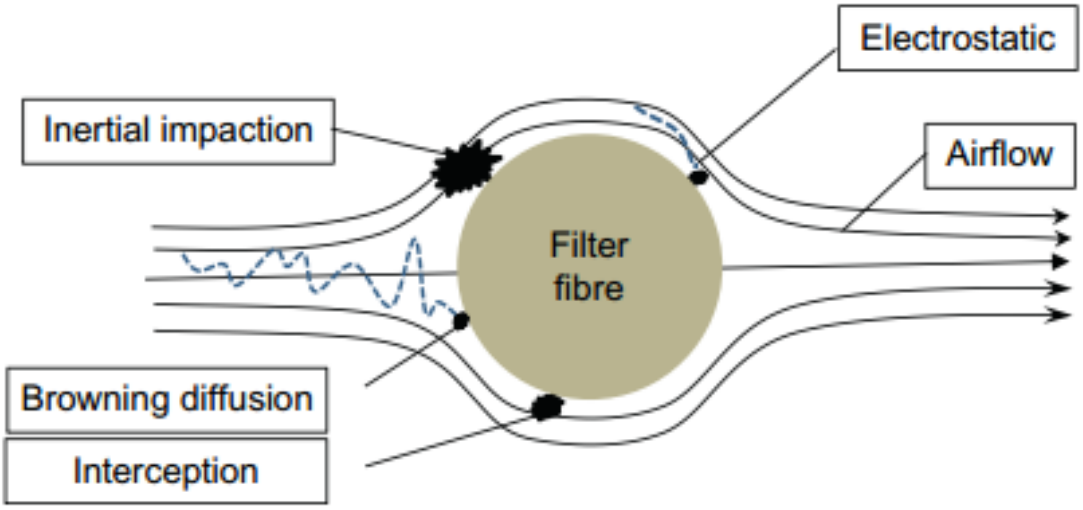

Figure.2.3. Schematic of air filtration mechanisms: inertial impaction, browning diffusion, interception and electrostatic [6].

Inertial impaction occurs when particles are no longer following the streamlines around the fiber before colliding the fiber and being captured due to their inertia. Increased momentum caused by large particle mass or diameter increases the inertial impaction. Higher air velocity also improves the inertia effect. This mechanism dominants particle capturing for particles larger than 1 μm.

Browning diffusion, or Brownian diffusion, occurs when the air velocity is relatively low, and the particle size is small. Particle under diffusion follows a random path in movement, which is known as Brownian motion. As its path passing the fiber is longer than the curved streamline, the particle can easily collide with the fiber, being captured eventually. Diffusion is effective mostly on particles smaller than 0.3 μm.

Interception occurs when the particles follow the streamline and the distance between the streamline and the fiber is smaller than the particle radius. Particles under this motion are inevitably to collide with the fiber and be captured. Interception is one of the major filtration mechanisms for particles between 0.1 and 1 μm.

2.2.3. Filter clogging

Davis [7] reported the fact that deposited particles do not distribute evenly on the filter surface. Instead, these particles build up chain aggregates that act similarly like fine fibers. These chain aggregates were later called as dendrites [6, 8]. The schematic of dendrite formation under particle loading is shown in Figure. 2.4.

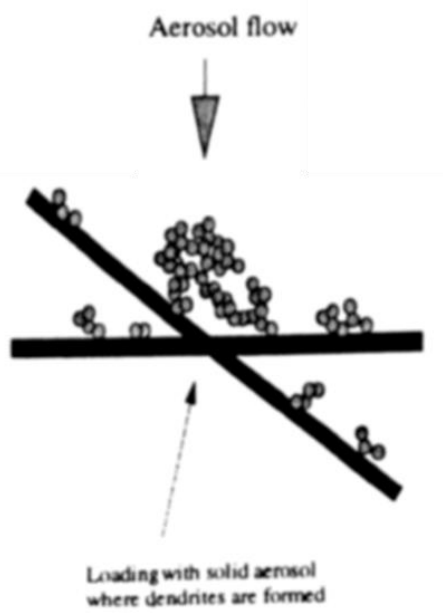

Figure.2.4. Schematic of dendrite formation under solid aerosol loading [8].

The filter clogging process typically includes three consequent stages: depth filtration, particles are captured mostly inside the filter structure and the pressure drop increases slowly during this stage; transition, particle deposition changes from depth to surface and pressure drop increase rapidly after a certain point named as the clogging point [7]; surface filtration, most particles are captured by the filter surface and a surface particle cake is gradually formed. In the surface filtration stage, pressure drop increases rapidly and its increasing rate eventually becomes constant. In this stage, particles would be directly captured by the filter surface or filter cake. This filtration process is also called as sieving. One example of the evolution of filter clogging is shown in Figure.2.5 [Song 2006].

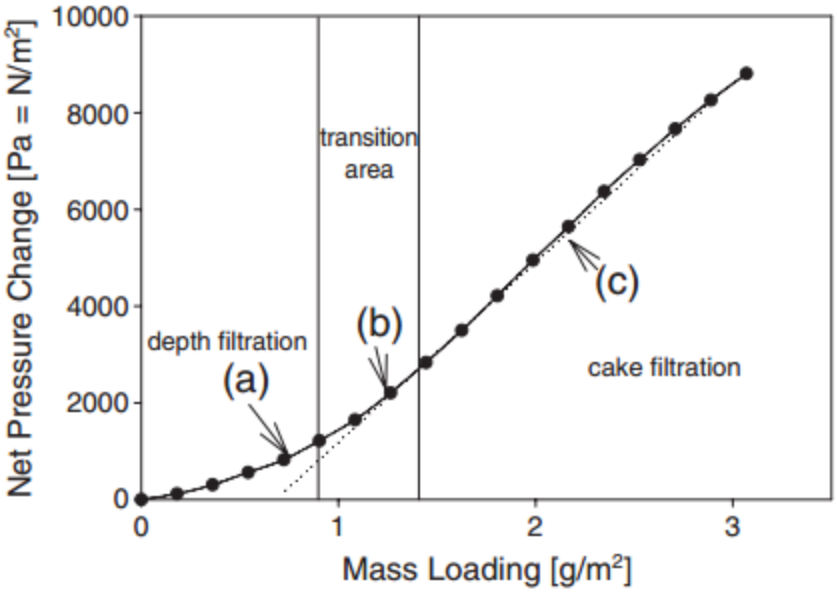

Figure.2.5. An example of the evolution of filter clogging [9].

2.3. Filter structure-filtration property relationship

2.3.1. Effects of filter structure properties on filtration and particle loading behaviors

Early studies regarding the particle loading behavior or the filtration properties, i.e. filtration efficiency, pressure drop, deposited mass, during the filtration process focused on the effect of filtration conditions on the particle loading behavior. The effect of particle shape [10], particle size [8], particle concentration [11], face velocity [9], particle composition [12] etc. were studied.

After those studies, limited research regarding the effects of filter structure properties has been carried out. Leung [13] discovered the fact that filter made with fine fibers led to higher pressure drop increase rate, faster clogging and lower dust holding capacity by comparing the particle loading behavior of electrospun nanofiber nonwoven membranes with different fiber diameter. A similar result was found that filters with higher fiber packing density led to faster clogging and shorter filter life [14]. Except for nanofiber filters, some studies regarding structure properties

relied on simulation and modeling. Tafreshi studied the effect of fiber orientation distribution [15] and fiber cross-section [16] on filtration properties during the filtration process.

Although Leung et.al. studied the two most important structural properties, i.e. fiber diameter and fiber packing density (fiber solidity), at the nanoscale with nanofiber membrane, the effects of nonwoven filter structure properties on the particle loading behavior at general micron scale are not yet studied. Other structural properties, such as basis weight, pore size, etc. remain to be studied by experiments or simulation tools.

2.3.2. Effect of structural gradient on filtration and particle loading behaviors

Before the studies of Leung et. al. on the area of skin effect caused by the cake formation of particle loading, limited attention in this filed was focused on the relationship between the particle deposition profile and the particle loading behavior. Leung [13, 14, 17, 18] also studied the effect of filter structural gradient on nanoparticle loading behavior by creating composite filters composed of microfiber layer (s) and nanofiber layer (s). As a result, filters with correct structure gradient design can not only extend the filter life but also improve the filtration efficiency, as the benefits of the coarse filter and fine filter have been put together. One example of the gradient structure design is shown in Figure.2.6.

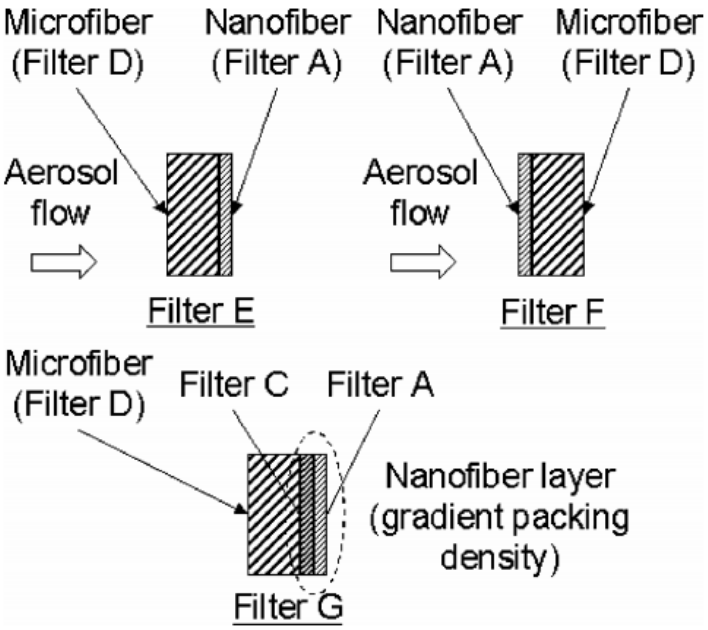

Figure.2.6. Example of filter structure gradient design [13].

Although Leung tried many gradient structure designs, the real problem regarding the comprehensive filtration performance of a gradient filter is particle deposition, i.e. how the particles are captured, deposited and distributed inside the filter structures. Leung also carried out some modeling works regarding the particle deposition in single-layer filter [18] and multi-layer filter [19], however, the particle deposition inside the filter and more importantly, the particle deposition between two stacked filters have not been fully understood.

2.4. Loaded filter structure characterization with imaging tools

In the early study of loaded filter structure characterization, Thomas [11] used adhesive tape to get the solid particles off from different points across the filter depth of high-efficiency filter media. It was found that most particles were captured by the close part of the filter facing airflow, as

shown in Figure.2.7. Because of the structure deformation caused by sample cutting and low accuracy of measurement, various studies were carried out to characterize the structures of filters loaded with solid particles using different imaging tools. This section reviewed four typical imaging tools, optical microscope, scanning electronic microscope (SEM), digital volumetric imaging (DVI) and X-ray micro-computed tomography (XMCT).

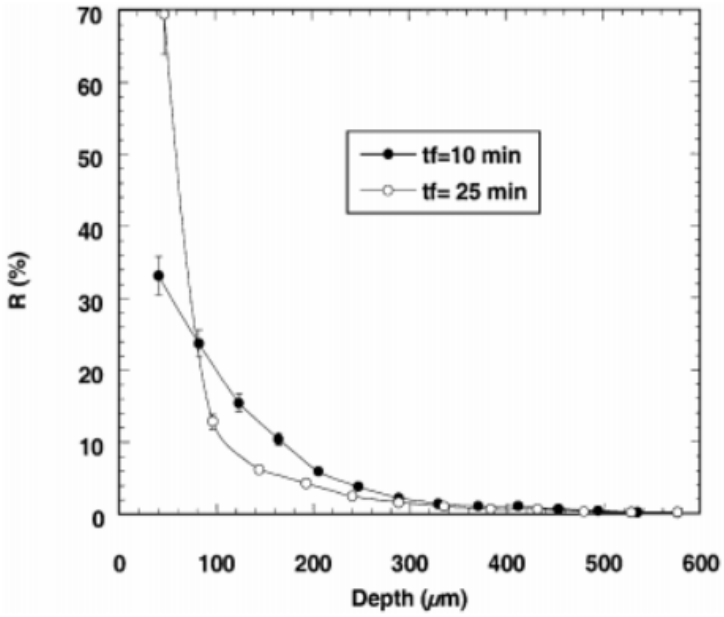

Figure.2.7. Particle penetration profile of soda fluorescein particles inside the filter for two values of filtration time [11].

2.4.1. 2D imaging: optical microscopy

The surface and cross-section of fibrous materials can be directly observed with the optical microscope. Venu et.al. [20] introduced a method of characterizing the structure change between a fiber web and hydroentangled nonwoven. A two-layer fiber web was prepared with the top layer

dyed as blue while the bottom layer remained original. In this way, the structures of fiber web before and after the hydroentangling process can be successfully visualized and compared under the optical microscope. Similarly, Ning et.al. [21] studied the structure change of a two-layer fiber web with the top layer dyed as blue before and after the needle punch process using the optical microscope.

The optical microscope was also used in the structure observation of filters loaded with solid particles. Jabric [22] compressed the coarse filter with different pressures. Composites consisted of a compressed depth filter and a high-efficiency filter was prepared and loaded with solid particles. The cross-sections of these composites were visualized and compared with the help of an optical microscope, as shown in Figure.2.8. In this case, the cross-sections of loaded filters were directly visualized. However, the structures were deformed inevitably by the sample cutting and quantitative analysis of the structures was not an option.

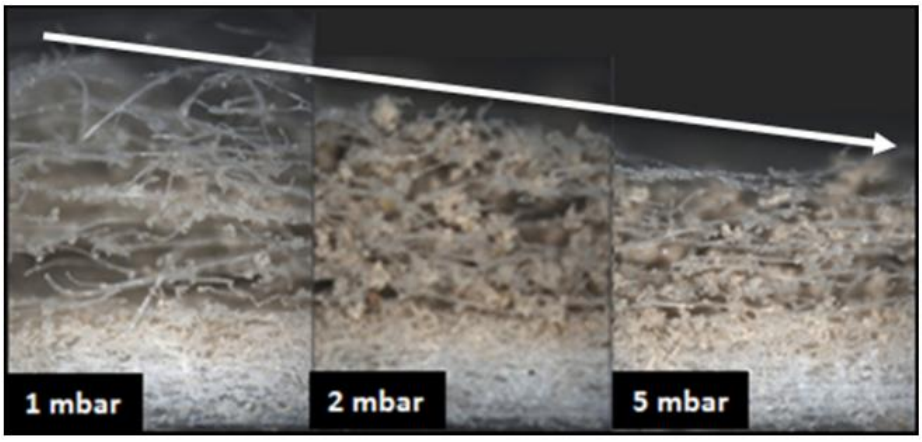

Figure.2.8. Example of imaging clogged filter structure using an optical microscope [22].

2.4.2. 2D imaging: scanning electronic microscopy (SEM)

As another 2D imaging tool, the SEM was widely used in the area of fibrous material characterization, especially the nanofiber characterization. Due to the advantage of high magnification and high contrast, the SEM was also widely used in characterizing the loaded filter structures [3, 11]. One example is shown in Figure.2.9.

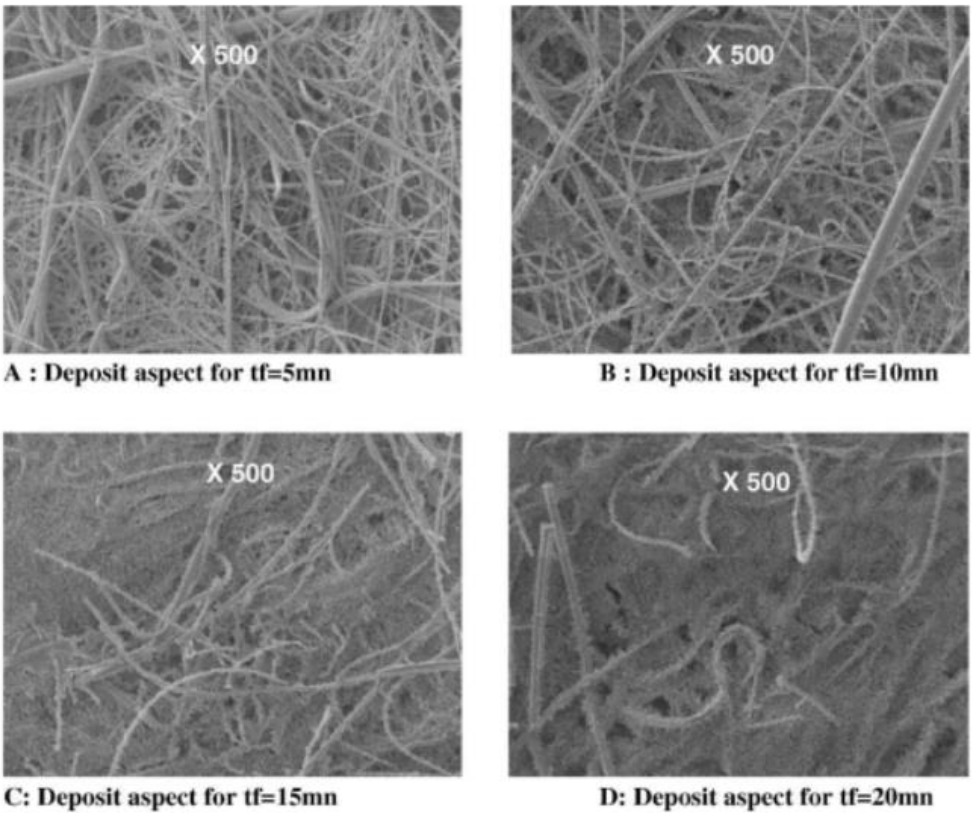

Figure.2.9. Example of imaging filter structures using SEM [11].

Even though the filter structures were still changed by the sample cutting, Thomas et.al. [23] studied the nanoparticle distribution in flat and pleated high-efficiency filters during clogging using the SEM equipped with energy-dispersive X-ray spectroscopy (EDX). With the variation of

packing density signals, the nanoparticle distribution was quantitatively plotted, as shown in Figure.2.10.

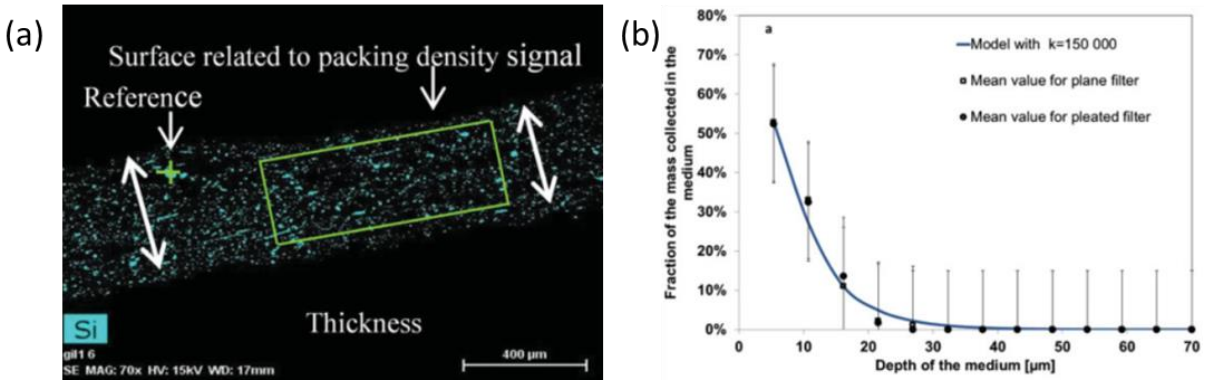

Figure.2.10. Example of imaging clogged filter structure using SEM (SEM/EDX): (a) Illustration of the packing density measurement using SEM/EDX. (b) mean particle penetration profile in the thickness of the flat filter and the pleated filter [23].

2.4.3. 3D imaging: digital volumetric imaging (DVI)

Digital Volumetric Imaging (DVI) microimager® (Microscience Group Inc., USA) is a 3D imaging tool originally designed for the 3D imaging and characterization of biological studies. The sample block is prepared by embedding the fluorescently stained samples into the polymer matrix. Then the sample block is placed in the motorized image stage and it is cut by a diamond knife based on the preset section thickness. Images of the sample block surface are captured through the fluorescence filter cube and motorized RGB filter wheel. A 3D image set of sample sections are finally obtained. The schematic of the DVI microimager® image capturing system is shown in Figure.2.11.

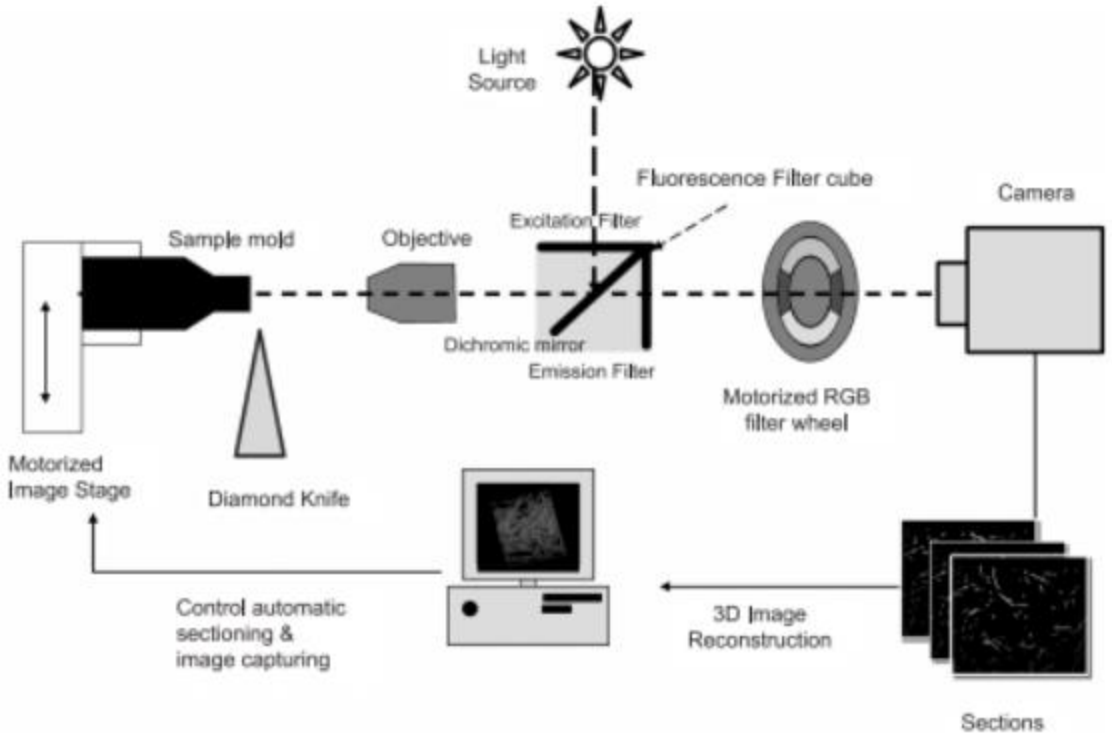

Figure.2.11. Schematic of the image capturing system of the DVI microimager® [24].

The 3D image set can be further reconstructed and analyzed using the RESView^{TM} software to acquire and visualize the 3D structure. Tafreshi et.al. [25] acquired the 3D structures of nonwovens compressed under different pressures and modeled the pore size distribution of those samples based on the DVI 3D images. Medhi [26] obtained the 3D structures of needle-punched nonwovens and further simulated and modeled the air permeability. Furthermore, the solid volume fraction distribution profile of the sample along with all three directions, MD, CD, and TD, can be derived by exporting the 2D sections, as shown in Figure.2.12 [24]. Different components of the sample can also be stained with different fluorescent chemicals to study the 3D structure. Shim et.al. [Shim 2010] studied the 3D structure of segment-pie bicomponent nonwovens. Venu characterized the 3D structure of hydroentangled nonwovens originally with a nylon/polyester two-layer web

structure [27]. Venu also studied the impacts of high-speed water jets on web structures [28] and the effect of the number of manifolds on hydroentangled nonwoven structures [29].

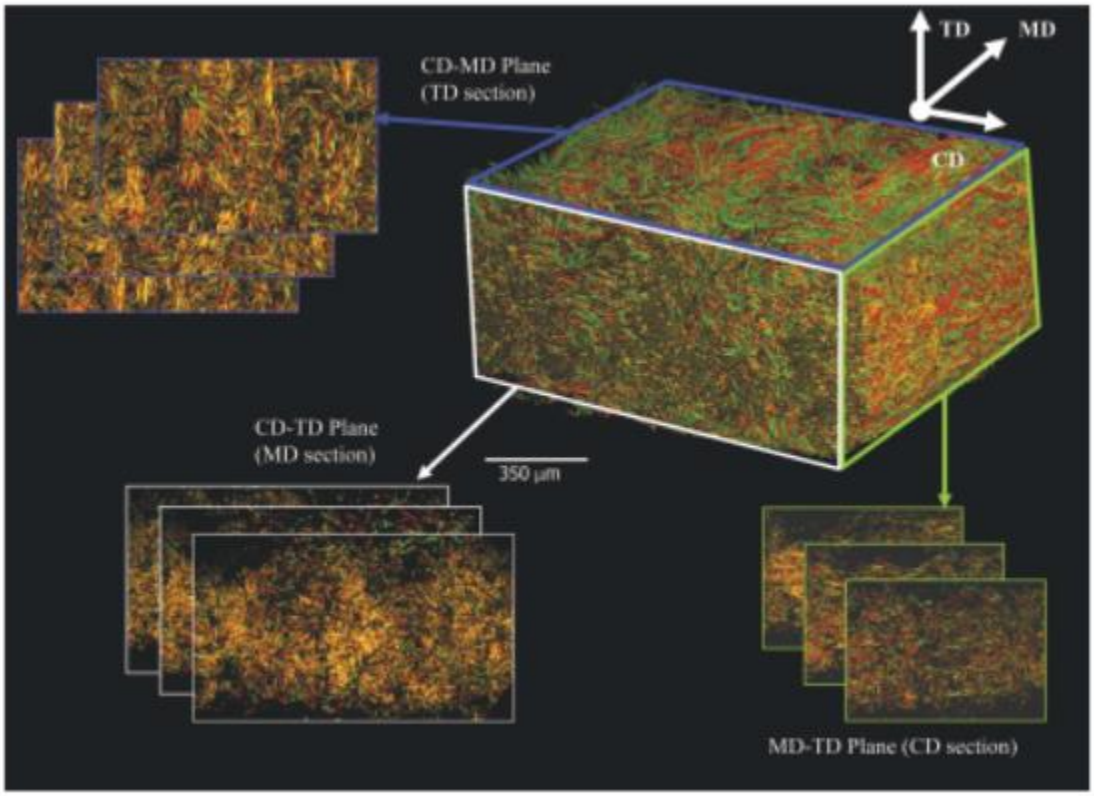

Figure.2.12. Exporting 2D sections [24].

Previous studies proved that DVI could work as a good candidate for imaging the 3D structure of clean nonwoven filter media. However, it is not suitable for the structural characterization of the loaded filter due to its sample preparation process, because embedding the loaded filter sample into the polymer matrix would change the particle positions.

2.4.4. 3D imaging: X-ray micro-computed tomography (XMCT)

2.4.4.1. Basics of XMCT

The X-ray micro-computed tomography (XMCT) is the X-ray computed tomography (XCT) with a resolution of the micron level. Similarly, the X-ray nano-computed tomography with a resolution of the nanometer level also exists. Tomography is referred to as the quantitative description of a slice of matter within a bulky object, and the X-ray is the most used method to deliver specific images [30]. As a 3D imaging technique that can offer non-invasive visualization and characterization of the internal structures, the XCT is widely used in both medical and industrial fields. It has also been applied to study various materials, such as metal, bone, fibrous material, etc.

A schematic of the synchrotron XMCT system is shown in Figure.2.13. Comparing with standard laboratory equipment, the synchrotron XMCT offer reduced exposure times, i.e. less imaging time, and increased signal-to-noise ratio [30]. The X-ray tube in standard XMCT is replaced by the synchrotron source to generate the X-ray beam. The transmitted beam penetrates the sample and then it is then converted into visible light by a scintillator and the signal is recorded with a camera of the 2D detector, forming projections. The transmitted beam is typically recorded for many different angular positions equally spaced between 0º and 180º, as the sample rotates step by step. A series of projections are captured, and these projections are then sent to the reconstruction process with a filter back-projection algorithm. As a result, the X-ray attenuation coefficient distribution could be quantitatively mapped as image slices described with grey values of different pixels. The generated image slice set is ready for further image analysis.

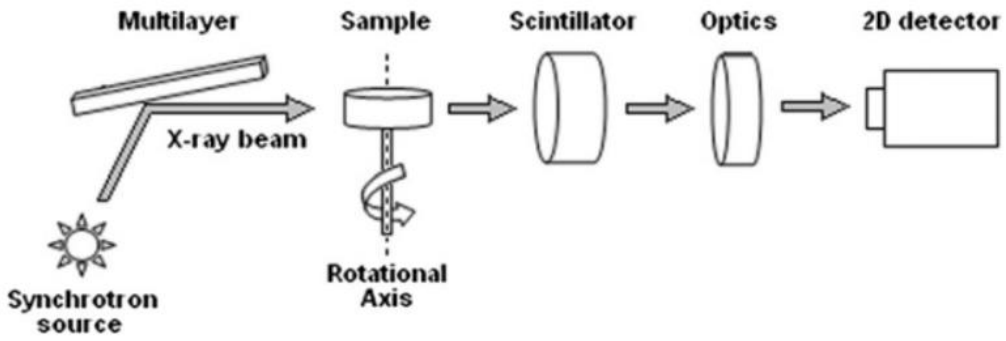

Figure.2.13. Schematic of synchrotron X-ray micro-computed tomography (XMCT) system [31].

Among the three typical types of XCT, transmission, scattered photons, and emission, the transmission XCT is the most widely used in material science study. Transmission XCT delivers a map of μ (x, y), the linear attenuation coefficient, as shown in Figure.2.14 a. For XCT below 200 keV photon energy, the following equation (1) is often used to describe the mass attenuation coefficient to compare the attenuation performance of different materials under X-ray transmission:

$$\mu/\rho = K*Z^4/E^3, \quad (1)$$

where ρ is the material density, K is a constant, Z is the atomic number of material and E is the photon energy. This equation indicates that a high atomic number or low photon energy leads to a high mass attenuation coefficient. The comparison of the mass attenuation coefficient of two different materials, carbon and iron, is shown in Figure.2.14 b. This attenuation behavior is very important for the XMCT imaging with different materials being investigated, for example, the imaging of polymeric fibrous filter media loaded with standard test dust containing a wide range of chemical elements.

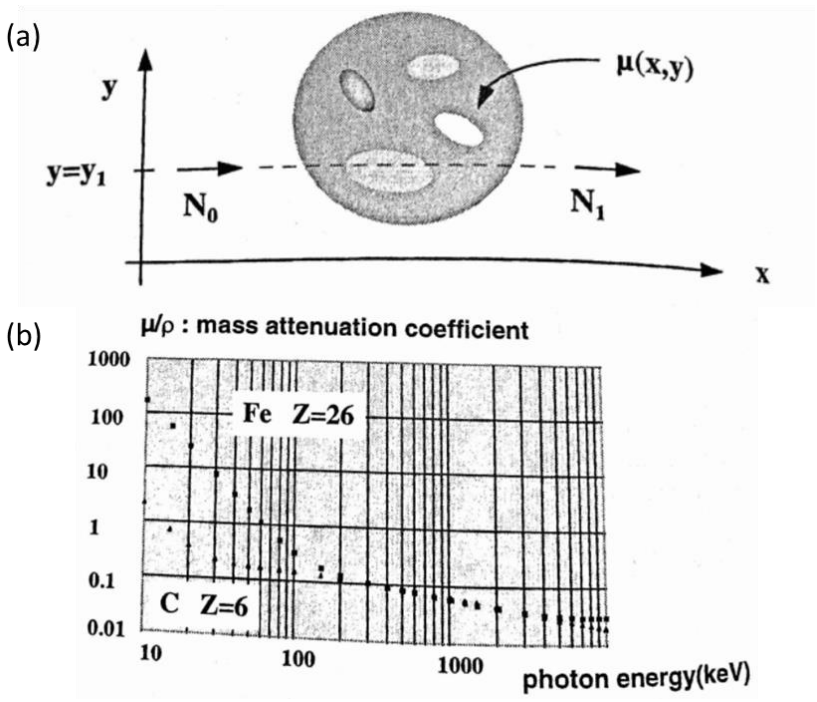

Figure.2.14. (a) The physical basis of transmission tomography inside a slice, (b) value of the mass attenuation coefficient for carbon and iron [30].

The two most important parameters of XMCT imaging are photon energy and resolution. From equation (1), it is known that low photon energy leads to a high mass attenuation coefficient, resulting in more significant differences between the mass attenuation coefficient of materials with different densities and higher contrast of gray values in the final image slice. This phenomenon is important for the XMCT imaging of polymeric fibrous structures because the densities of polymer fibers are typically very low and close to the air. Resolution is the term to describe how well the details are presented in images. The resolution in digital image relates to the 2D pixels and 3D voxels, the respective smallest unit of 2D area and 3D volume. Generally, the pixels and voxels are respectively considered as square and cube. The 1.0 μm resolution means a pixel size of 1.0 μm*1.0 μm and a voxel size of 1.0 μm*1.0 μm*1.0 μm. These two units are also respectively used

in describing the dimensions of 2D images and 3D volumes. For example, a 2D image may have a dimension of 800 pixels*600 pixels, and a 3D volume may have a dimension of 600 voxels*600 voxels*800 voxels.

2.4.4.2. Filter structure characterization with XMCT

The XMCT has been widely used in characterizing the fibrous structures. Gervais [32] studied the fiber diameter distribution of fiberglass filter media. Yu [33] studied the fiber length distribution of cashmere fabrics. Soltani [34] investigated the 3D fiber orientation of nonwoven fabrics. Fiber solid volume fraction distribution of fibrous materials was also studied [35, 36].

As a non-invasive 3D imaging technique, X-ray micro-computed tomography (XMCT) also becomes very ideal in terms of structural characterization of clogged fibrous filters as well. In recent years, studies carried out utilizing the XMCT or modified CT has emerged. Charvet et al. [31] utilized the synchrotron X-ray holotomography to study fibrous filter media clogged with a liquid aerosol of di-ethyl-hexyl-sebacate (DEHS) and discovered the heterogeneous liquid distribution through the thickness of the clogged filter. Thomas et al. [23] utilized both single-photon emission and X-ray computed tomography to study the aerosol deposition in the pleated filter by analyzing the mean voxel intensity of particles in pleat depth, filter width, and filter height respectively. Jackiewicz [37] studied the particle deposit behavior with the simulation of the non-steady state filtration process by blowing clean air stream through the loaded filter media at different velocities. Riefler [38] studied particle penetration of filters clogged with standard dust particles (Al2O3) and discovered an exponential decay of the penetration depth of particles, as shown in Figure.2.15. However, all these studies focused on the clogging of fine filters and the structural characterization of clogged coarse filters remains undiscovered.

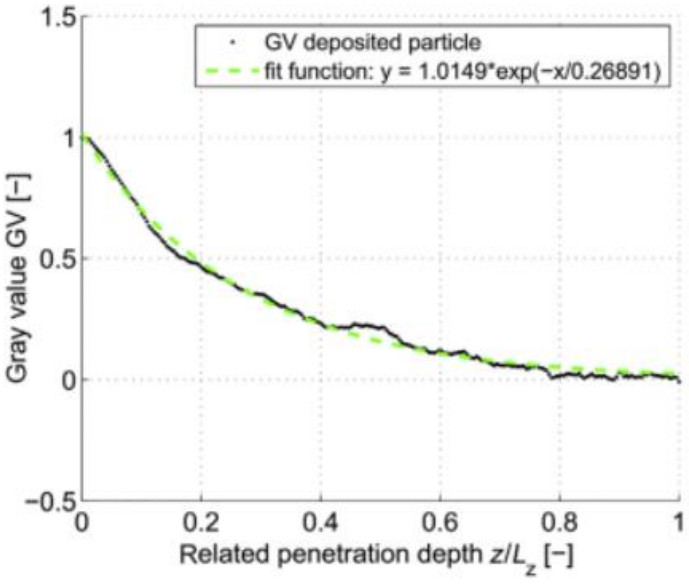

Figure.2.15. Gray values of particle penetration profile (black curve) and fitted exponential decay (dashed line) [38].

2.4.4.3. Meta artifact

It is known that the metal substance such as belt buckles, rings, keys, etc. should be removed from the patient before taking the medical CT because the metal artifact caused by those metal substances would affect the image quality of CT images and thus bringing difficulties to the diagnosis. A typical medical CT image affected by the metal artifact can be found in Figure.2.16 [39].

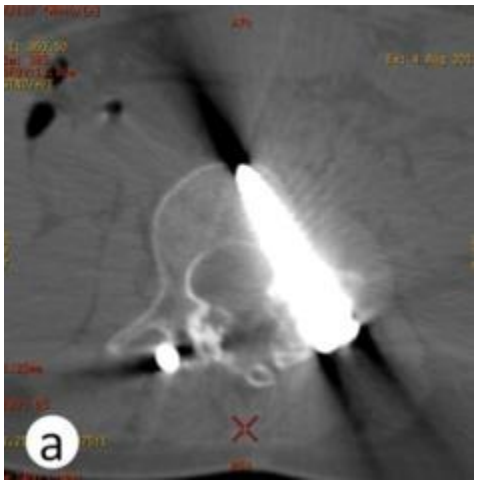

Figure.2.16. Medical CT image affected by the metal artifact [40].

Metal artifacts occur because the density of the metal is way higher than those of other substances scanned at the same time, and the metal artifacts consist of beam hardening and scatter that produce dark streaks. As an X-ray beam is composed of individual photons with a range of energies, the lower-energy photons are absorbed more rapidly than then higher-energy photons due to the high density of the meal, which makes the beam 'harder' with higher mean energy. As the beam gets harder, it would be more intense when it reaches the detector than those beams are not harden, resulting in the formation of a dark streak [40]. The scatter caused by the metal makes the X-ray photons to change direction and energy and thus leading to dark streak as well. Bright streaks are seen adjacent to the dark streaks due to the low beam energy after scattering [41]. These bright and dark streaks caused by beam hardening and scatter of metal artifact would affect the image quality. In the medical CT imaging field, methods such as filtering [42] and machine learning [43, 44] were discovered to reduce or remove the metal artifact. However, there is not a good method that can be easily applied to effectively reduce the metal artifact in the field of material science study.

In this study, one thing required to be considered for XMCT imaging and image processing is the metal artifact caused by the existence of metal elements. The metal artifact could be reduced by using high photon energy [Wang 2013]. However, for the XMCT imaging of polymeric fibrous nonwoven filter loaded with standard fine dust, relative low photon energy is required since X-ray with high photon energy could penetrate the polymer fibers with minimum attenuation occurred. As a result, it would be extremely difficult to differentiate the polymer fibers and pores due to the low contrast under high photon energy imaging. The relatively low photon energy of 90 kV was selected given the contradictory requirement of photon energy for polymer fiber imaging and metal artifact reduction. Since filters loaded with the heavy amount of standard fine dust contained a high concentration of metal elements which would cause significant metal artifact, only the filters with relatively light and medium particle loading were scanned by the XMCT.

2.5. Image processing and image analysis

With the images acquired from the previously described 2D and 3D images, the image processing and image analysis allow further analysis. Image processing refers to the application of a variety of techniques in modifying the original images. The image processing of fibrous materials images typically consists of the image pre-processing and segmentation. Image analysis is applied to make a quantitative description of the images [45]. One useful image analysis process used in this study is skeletonization.

2.5.1. Image pre-processing

Filters that are widely used in the image pre-processing includes the noise removal filters, e.g. mean filter and median filter, and edge detection filters, e.g. Laplacian filter and Sobel operator (gradient filter). The noise removal filters are applied to remove the noise pixels of the original images. The edge detection filters can make the edges of different components clear in the image, thus allowing better segmentation performance to separate those components. Under the scope of this study, only the noise removal filters are critical to image processing.

For the mean filter, the gray value of each pixel within a given window (e.g. 3 pixels*3 pixels) is measured. If the gray value of the center pixel is significantly different than the average gray value of the surrounding pixels (according to a preset threshold value, typically set as default by the image processing software), it is then replaced by the average gray value [45].

Rather than the average gray value of the neighborhood (surrounding pixels), the median gray value is used in the median filter. Comparing with the mean filter, the median filter has two advantages. One is the new gray value always comes from one of the original values of its neighborhood when the number of neighboring pixels is odd. Second is the median filter is less sensitive to extreme values [46]. The median filter is an effective technique in noise removal. Its performance is shown in Figure.2.17 c. As an important parameter of the median filter, the larger neighborhood size leads to stronger denoising performance. However, it also makes the image blurred, as shown in Figure.2.17 d. As a result, a balance between the filtering performance and image quality should be considered during the neighborhood size selection in the median filter.

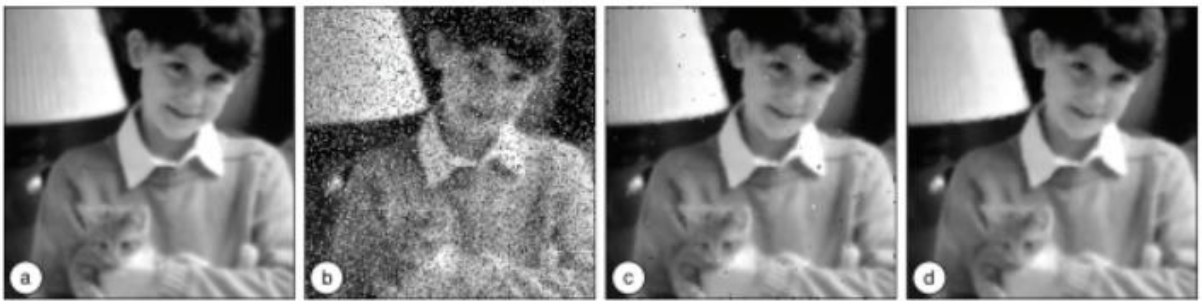

Figure.2.17. Noise removal with a median filter: (a) original image, (b) image (a) with 10% of pixels randomly selected and set to black, and another 10% randomly selected and set to white, (c) result of median filtering using a 3*3 square region, (d) result of median filtering using a 5*5 octagonal region [47].

Morphological processing, also known as morphological transform or mathematical morphology, is another useful image pre-processing technique. It is used to modify the morphology of information in the image based on mathematical algorithms [48]. Two basic morphological processing operations are erosion and dilation. Dilation fills holes in objects and closes gaps between objects. Erosion removes background noise and opens space between contacting objects [49]. The opening is the combination of an erosion followed by a dilation that can open gaps between just-touching objects, while the closing is the combination of a dilation followed by an erosion which can close small holes in objects or gaps between neighboring objects [47]. The illustrations of erosion, dilation, opening, and closing can be found in Figure.2.18. The morphological processing becomes critical when some pixels are not supposed to be there, for example, some noises may not be removed by the previous mean or median filter. For XMCT imaging of fibrous materials, hole imaging defects frequently occurred inside the fibers because of the photon reflection due to the curved fiber surface [32, 36]. The closing processing was found

helpful to reduce this hole defect, although that was impossible to be completely removed only by image processing [Jackiewicz 2015].

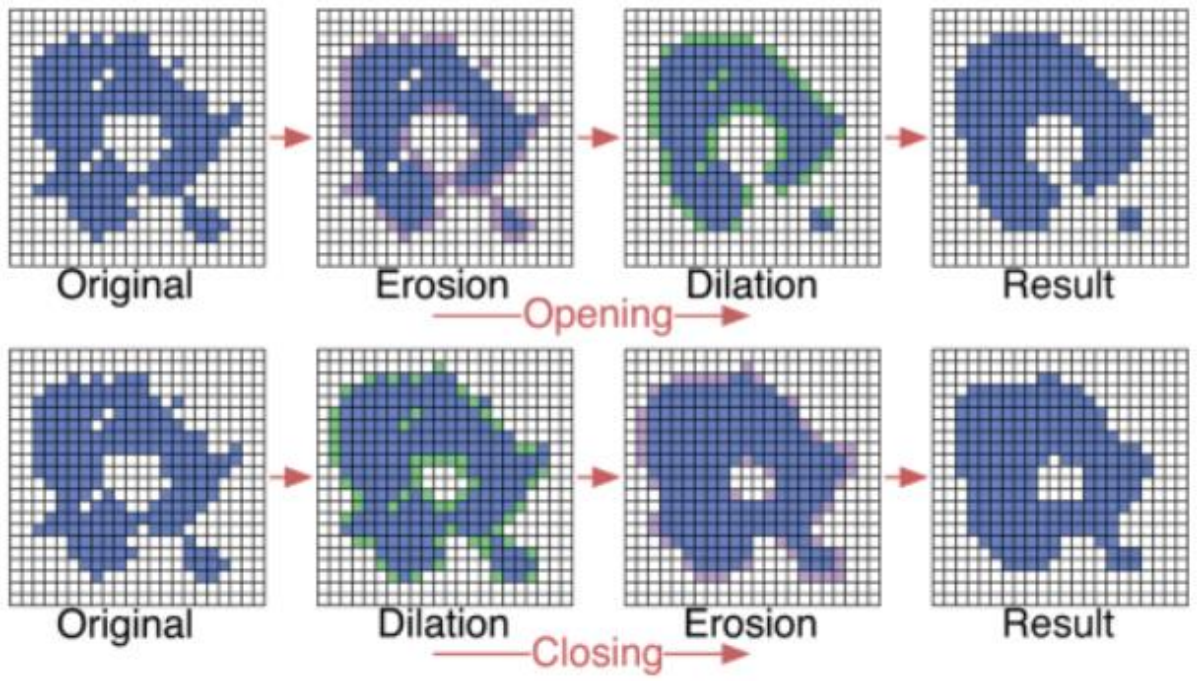

Figure.2.18. Combing erosion and dilation to produce an opening or a closing. Colors indicate pixels that are removed (magenta) or added (green) in each step [47].

2.5.2. Segmentation

Segmentation is a process designed for two tasks: to separate different phases or components in the gray value image and to identify connected objects [49]. The previous one is the major task in characterizing the 3D structure of fibrous materials, especially the fibrous filter media loaded with silicon-based standard test dust. The method for this type of segmentation is thresholding. In a gray value image, a gray value distribution profile can be drawn based on the gray values of individual pixels. An example is shown in Figure.2.19. Objects of the same materials have very

close gray values due to the same attenuation coefficient. Therefore, it is easy to select all the objects of one specific material in the image by selecting a thresholding range, a gray value range. However, finding a proper thresholding range could sometimes be very difficult due to the overlapping of gray values of different components.

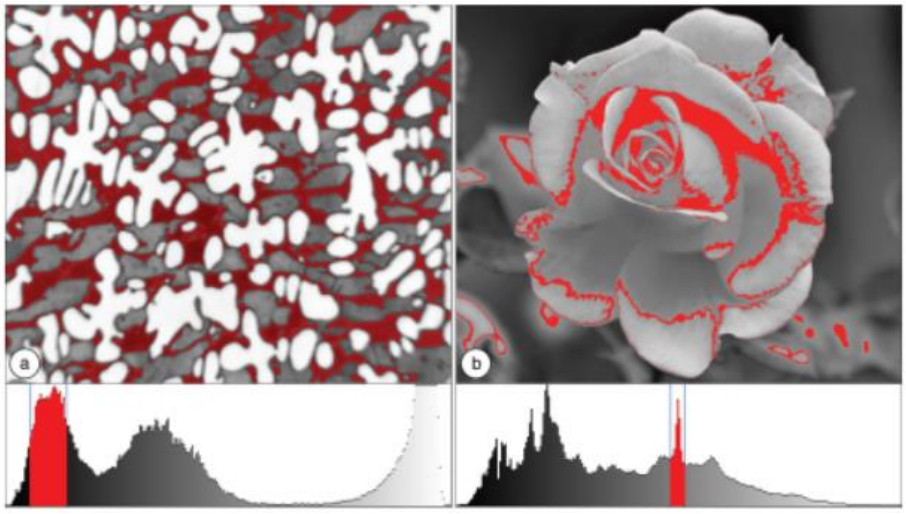

Figure.2.19. Example of thresholding an image based on a peak in the histogram: (a) metal surface imaged in a microscope, (b) real-world photography of a 3D flower using ambient light [47].

Binarization is one method of thresholding performed to turn a gray value image into completely black and white by setting up a threshold value. All pixels below that value are considered as background (white) and pixels above that value are considered as foreground (black). Binarization is frequently used in characterizing structures of fibrous materials, such as clean filter media [32, 35]. Similarly, a trinarization method is possible for the segmentation of loaded fibrous filter media with two thresholding values to separate the fiber, particle, and pore.

2.5.3. Skeletonization

Skeletonization is the process to derive the medial axis of a feature in the binary image. One typical method for constructing the skeleton is the Euclidean distance map (EDM). The EMD is a tool to obtain a gray value image based on a binary image. It's defined that 'each point in the foreground is assigned a brightness value equal to its straight-line distance from the nearest point in the background' [47]. With the skeletonization by the EMD process, for example, the medial axis along the fiber length of a given fiber can be located. Another example of skeletonization is shown in Figure.2.20. In this figure, four nodes (blue branch points), eight segments (four yellow terminal segments and four internal segments) and fiver endpoints (red) form the skeleton of this feature. Nodes here connect different segments of the skeleton, and segments are the basic units that constructed the skeleton.

Figure.2.20. Diagram of the skeleton of a feature with five endpoints (red), four nodes (blue), four terminal segments (yellow), four internal segments (green) [47].

As a useful method of image analysis, the skeletonization process can be used to generate the 3D pore skeleton network of fibrous materials [50, 51]. The nodes in the pore skeleton network can be used to evaluate the pore connectivity [26]. The thickness of segments can be considered as the pore diameter. Therefore, a pore diameter distribution profile can be plotted based on the segment thickness data derived from the pore skeleton network. More importantly, an average pore diameter is calculated based on the average segment thickness of each point along the segment. In this way, the entire path of a 3D pore is considered, unlike the pore structure characterization methods that are limited to 2D [52, 35] or without considering the whole pore structure [25].

References

[1] Batra, S. K., & Pourdeyhimi, B. (2012). Introduction to nonwovens technology. DEStech Publications, Inc.

[2] Bhat, G. S., Gulgunje, P., & Desai, K. (2008). Development of structure and properties during thermal calendering of polylactic acid (PLA) fiber webs. Express Polymer Letters, 2(1), 49-56.

[3] Liu, J., Zhang, X., Zhang, H., Zheng, L., Huang, C., Wu, H., ... & Jin, X. (2017). Low resistance bicomponent spunbond materials for fresh air filtration with ultra-high dust holding capacity. RSC Advances, 7(69), 43879-43887.

[4] Hassan, M. A., Yeom, B. Y., Wilkie, A., Pourdeyhimi, B., & Khan, S. A. (2013). Fabrication of nanofiber meltblown membranes and their filtration properties. Journal of membrane science, 427, 336-344.

[5] Brown, R. C. (1993). Air filtration: an integrated approach to the theory and applications of fibrous filters. Pergamon.

[6] Brown, P., & Cox, C. L. (Eds.). (2017). Fibrous Filter Media. Woodhead Publishing.

[7] Davies, C. N. (1973). Air filtration.

[8] Walsh, D. C., Stenhouse, J. I. T., Scurrah, K. L., & Graef, A. (1996). The effect of solid and liquid aerosol particle loading on fibrous filter material performance. Journal of Aerosol Science, (27), S617-S618.

[9] Song, C. B., Park, H. S., & Lee, K. W. (2006). Experimental study of filter clogging with monodisperse PSL particles. Powder technology, 163(3), 152-159.9

[10] Wake, D., Brown, R. C., Trottier, R. A., & Liu, Y. (1992). Measurements of the efficiency of respirator filters and filtering facepieces against radon daughter aerosols. The Annals of occupational hygiene, 36(6), 629-636.

[11] Thomas, D., Penicot, P., Contal, P., Leclerc, D., & Vendel, J. (2001). Clogging of fibrous filters by solid aerosol particles experimental and modeling study. Chemical Engineering Science, 56(11), 3549-3561.

[12] Walsh, D. C., & Stenhouse, J. I. T. (1997). Clogging of an electrically active fibrous filter material: experimental results and two-dimensional simulations. Powder Technology, 93(1), 63-75.

[13] Leung, W. W. F., Hung, C. H., & Yuen, P. T. (2009). Experimental investigation on continuous filtration of sub-micron aerosol by filter composed of dual-layers including a nanofiber layer. Aerosol Science and Technology, 43(12), 1174-1183.

[14] Leung, W. W. F., Hung, C. H., & Yuen, P. T. (2010). Effect of face velocity, nanofiber packing density, and thickness on filtration performance of filters with nanofibers coated on a substrate. Separation and purification technology, 71(1), 30-37.

[15] Fotovati, S., Tafreshi, H. V., & Pourdeyhimi, B. (2010). Influence of fiber orientation distribution on performance of aerosol filtration media. Chemical Engineering Science, 65(18), 5285-5293.

[16] Hosseini, S. A., & Tafreshi, H. V. (2011). On the importance of fibers' cross-sectional shape for air filters operating in the slip flow regime. Powder technology, 212(3), 425-431.

[17] Hung, C. H., & Leung, W. W. F. (2011). Filtration of nano-aerosol using nanofiber filter under low Peclet number and transitional flow regime. Separation and purification technology, 79(1), 34-42.

[18] Leung, W. W. F., & Hung, C. H. (2012). Skin effect in nanofiber filtration of submicron aerosols. Separation and Purification Technology, 92, 174-180.

[19] Leung, W. W. F., Hau, C. W. Y., & Choy, H. F. (2018). Microfiber-nanofiber composite filter for high-efficiency and low pressure drop under nano-aerosol loading. Separation and Purification Technology, 206, 26-38.

[20] Suragani Venu, L. B., Shim, E., Anantharamaiah, N., & Pourdeyhimi, B. (2014). Impacts of high-speed waterjets on web structures. The Journal of The Textile Institute, 105(4), 430-443.

[21] Sun, N. (2014). Structures of Needlepunched Fabrics and Needling Mechanism. North Carolina State University.

[22] Jabri, W., Vroman, P., & Perwuelz, A. (2015). Study of the influence of synthetic filter media compressive behavior on its dust holding capacity. Separation and Purification Technology, 156, 92-102.

[23] Bourrous, S., Bouilloux, L., Ouf, F. X., Appert-Collin, J. C., Thomas, D., Tampère, L., & Morele, Y. (2014). Measurement of the nanoparticles distribution in flat and pleated filters during clogging. Aerosol Science and Technology, 48(4), 392-400.

[24] Shim, E., Pourdeyhimi, B., & Latifi, M. (2010). Three-dimensional analysis of segmented pie bicomponent nonwovens. The Journal of The Textile Institute, 101(9), 773-787.

[25] Jaganathan, S., Tafreshi, H. V., Shim, E., & Pourdeyhimi, B. (2009). A study on compression-induced morphological changes of nonwoven fibrous materials. Colloids and Surfaces A: Physicochemical and Engineering Aspects, 337(1-3), 173-179.

[26] Gholipour Baradari, M. (2016). Studying Pore Structure of Nonwovens with 3D Imaging and Modeling Permeability.

[27] Venu, L. B. S., Shim, E., Anantharamaiah, N., & Pourdeyhimi, B. (2012). Three-dimensional structural characterization of nonwoven fabrics. Microscopy and Microanalysis, 18(6), 1368-1379.

[28] Suragani Venu, L. B., Shim, E., Anantharamaiah, N., & Pourdeyhimi, B. (2014). Impacts of high-speed waterjets on web structures. The Journal of The Textile Institute, 105(4), 430-443.

[29] Venu, L. B. S., Shim, E., Anantharamaiah, N., & Pourdeyhimi, B. (2017). Structures and properties of hydroentangled nonwovens: effect of number of manifolds. The Journal of The Textile Institute, 108(3), 301-313.

[30] Baruchel, J., Buffiere, J. Y., & Maire, E. (2000). X-ray tomography in material science.

[31] Charvet, A., Du Roscoat, S. R., Peralba, M., Bloch, J. F., & Gonthier, Y. (2011). Contribution of synchrotron X-ray holotomography to the understanding of liquid distribution in a medium during liquid aerosol filtration. Chemical Engineering Science, 66(4), 624-631.

[32] Gervais, P. C., Bourrous, S., Dany, F., Bouilloux, L., & Ricciardi, L. (2015). Simulations of filter media performances from microtomography-based computational domain. Experimental and analytical comparison. Computers & Fluids, 116, 118-128.

[33] Jing, H., & Yu, W. (2019). Estimation of fiber orientation and length distribution in cashmere fibrous assemblies. Textile Research Journal, 89(6), 1084-1093.

[34] Soltani, P., Johari, M. S., & Zarrebini, M. (2015). 3D fiber orientation characterization of nonwoven fabrics using X-ray micro-computed tomography. World J Text Eng Technol, 1, 41-47.

[35] Théron, F., Lys, E., Joubert, A., Bertrand, F., & Le Coq, L. (2017). Characterization of the porous structure of a non-woven fibrous medium for air filtration at local and global scales using porosimetry and X-ray micro-tomography. Powder technology, 320, 295-303.

[36] Zhu, L., Wang, X., Hinestroza, J. P., & Naebe, M. (2018). Determination of the porosity in a bifacial fabric using micro-computed tomography and three-dimensional reconstruction. Textile Research Journal, 88(11), 1263-1277.

[37] Jackiewicz, A., Jakubiak, S., & Gradoń, L. (2015). Analysis of the behavior of deposits in fibrous filters during non-steady state filtration using X-ray computed tomography. Separation and Purification Technology, 156, 12-21.

[38] Riefler, N., Ulrich, M., Morshäuser, M., & Fritsching, U. (2018). Particle penetration in fiber filters. Particuology, 40, 70-79.

[39] Wang, Y., Qian, B., Li, B., Qin, G., Zhou, Z., Qiu, Y., ... & Zhu, B. (2013). Metal artifacts reduction using monochromatic images from spectral CT: evaluation of pedicle screws in patients with scoliosis. European journal of radiology, 82(8), e360-e366.

[40] Barrett, J. F., & Keat, N. (2004). Artifacts in CT: recognition and avoidance. Radiographics, 24(6), 1679-1691.

[41] Boas, F. E., & Fleischmann, D. (2012). CT artifacts: causes and reduction techniques. Imaging in Medicine, 4(2), 229-240.

[42] Chen, L. M., Liang, Y., Sandison, G. A., & Rydberg, J. (2002, May). Novel method for reducing high-attenuation object artifacts in CT reconstructions. In Medical Imaging 2002: Image Processing (Vol. 4684, pp. 841-851). International Society for Optics and Photonics.

[43] Fredericksen, M. A., Zhang, Y., Hazen, M. L., Loreto, R. G., Mangold, C. A., Chen, D. Z., & Hughes, D. P. (2017). Three-dimensional visualization and a deep-learning model reveal complex fungal parasite networks in behaviorally manipulated ants. Proceedings of the National Academy of Sciences, 114(47), 12590-12595.

[44] Zhang, Y., Yang, L., Chen, J., Fredericksen, M., Hughes, D. P., & Chen, D. Z. (2017, September). Deep adversarial networks for biomedical image segmentation utilizing unannotated images. In International Conference on Medical Image Computing and Computer-Assisted Intervention (pp. 408-416). Springer, Cham.

[45] Ghosh, S.K. (2013). Digital image processing.

[46] Mather, P. M. (1987). Computer processing of remotely-sensed images—An introduction.

[47] Russ, J. C. (2016). The image processing handbook. CRC press.

[48] Snyder, W. E., & Qi, H. (2010). Machine vision. Cambridge University Press.

[49] Banhart, J. (Ed.). (2008). Advanced tomographic methods in materials research and engineering (Vol. 66). Oxford University Press.

[50] Huang, X., Wang, Q., Zhou, W., Deng, D., Zhao, Y., Wen, D., & Li, J. (2015). Morphology and transport properties of fibrous porous media. Powder technology, 283, 618-626.

[51] Huang, X., Wen, D., Zhao, Y., Wang, Q., Zhou, W., & Deng, D. (2016). Skeleton-based tracing of curved fibers from 3D X-ray microtomographic imaging. Results in physics, 6, 170-177.

[52] Xu, B. (1996). Measurement of pore characteristics in nonwoven fabrics using image analysis. Clothing and Textiles Research Journal, 14(1), 81-88.

CHAPTER 3. Structure Characterization of the Clogging Process of Coarse Fibrous Nonwoven Filter Media during Solid Particle Loading with X-ray Micro-Computed Tomography

Abstract

Fibrous nonwoven filters are widely used in various air filtration applications. Coarse filters are typically used to protect and extend the lifetime of high-efficiency filters. The filtration properties of the studied fibrous nonwoven coarse filter including differential pressure and filtration efficiency were found increasing along with the particle loading. Unlike high-efficiency filters, limited work had been carried out to study particle loading characteristics of coarse filters and no work had been done regarding the clogging process of coarse fibrous filters due to the lack of non-invasive and non-destructive structural characterization technique.

In this study, the X-ray micro-computed tomography (XMCT) was used to non-invasively characterize the 3D structures of clean and particle-loaded fibrous nonwoven coarse filters at different clogging stages. Heterogeneous distribution of both fiber solidity and particle solidity across the filter thickness was found based on the solidity derived from the 3D images. To be specific, particle distribution diagrams indicated that at the beginning of particle loading stages, particles were captured and trapped by the top part of filter thickness, which was corresponded to the reported clogging process of high-efficiency filters. Then particles could be found across the full filter thickness. However, during the transitioning from the depth filtration stage to the surface filtration stage, clogging of particle clusters with high particle solidity was found in the bottom part of filter thickness. As more particles were loaded, clogging was found in both the middle part and the bottom part. After that, the top part would be clogged, and surface cake would start forming thereafter. This is the first report of the clogging process of the fibrous nonwoven coarse filter.

Pore diameter distribution derived from the pore skeleton network of the 3D particle-loaded filter structures also described the same structure due to clogging.

Keywords: Clogging, Particle loading, Coarse filter, Nonwoven, X-ray micro-computed tomography

3.1. Introduction

The air filter is the key component of the air filtration system to control air quality. Fibrous nonwoven filters are widely used for various air filtration applications. One typical challenge for filter design is to manage the contradictory targets among different filtration properties, i.e. high filtration efficiency, low resistance, and long filter life. It is known that filtration efficiency could be easily improved by using fibers with a smaller diameter. However, this would lead to increased resistance and reduced filter lifetime. One general solution is to utilize the structural gradient in the filter design by putting a coarse filter on top of a high-efficiency filter. The coarse filter could capture and hold large particles with huge mass which provides high dust holding capacity and low initial pressure drop, while the high-efficiency filter enables to capture of small particles and therefore contributes to the high filtration efficiency. In this way, an ideal compromise could be reached among these contradictory filtration properties. Therefore, it is important to study both the coarse filters and high-efficiency filters.

During the filtration process, solid particles would form dendritic branches around the fibers soon after being loaded [1]. Then these branches would entangle with one another and occupy the pore space of filters which leads to clogging. The structural parameters of the initial clean filter could affect particle loading behavior, and the particle deposits that caused clogging could also determine

the increase in filtration efficiency and resistance, as they have become part of the clogged filter structure. To understand the relationship between initial filter structures and the dynamic filtration properties during particle loading, it is important to investigate the clogging process of filters to realize how particles are deposited inside the filter structure.

However, limited experimental work had been carried out early in this area under the scope of fibrous nonwoven filters. To the best of our knowledge, only Thomas et al. [2] collected particle deposits with adhesive tape and found out most particles were captured by the surface of the filter and deposits volume was lower and lower through the filter depth. Besides, studies relied on simulation and modeling. Leung et al. [3] modified the imperial model of Brown and determined the uniform deposits distribution across the filter thickness and there were more particles deposited on the top part. Tafreshi et al. [4] utilized numerical simulation to study the dust loading process of the fibrous filter and obtained a similar finding of particle deposits distribution.

One reason for the limited existence of studies regarding filter clogging could be the lack of proper structure characterization technique. Researchers utilized Scanning Electronic Microscopy (SEM) [5] or optical microscopy [6] images to observe the solid particle deposition both on the filter surface and across the filter depth. However, it was inevitable to avoid changing the particle positions and filter structure deformation during the sample cutting. Digital volume imaging (DVI) [7] could be used to visualize and analyze the 3D structure of the fibrous filter, but sample cutting was still required and thus DVI was not suitable for characterizing filters clogged with solid particles.

The X-ray micro-computed tomography (XMCT) is a 3D imaging technique that enables visualization and analysis of the internal structure of fibrous materials without deforming the filter structure. With the help of XMCT, fiber diameter distribution [8], fiber length distribution [9],

fiber orientation [10] and fiber solid volume fraction [11] of fibrous materials were studied. As a non-invasive and non-destructive 3D imaging technique, X-ray micro-computed tomography (XMCT) has become an ideal candidate for the structural characterization of clogged fibrous nonwoven filters. Charvet et al. [12] utilized synchrotron X-ray holotomography to study the fibrous filter media clogged with liquid aerosols of di-ethyl-hexyl-sebacate (DEHS) and discovered the heterogeneous liquid distribution through the thickness of the clogged filter. Thomas et al. [13] used both single-photon emission and X-ray computed tomography to study the aerosol deposition in the pleated filter by analyzing the mean voxel intensity of particles in pleat depth, filter width, and filter height respectively. Jackiewicz [14] studied the particle deposition behavior with the simulation of the non-steady state filtration process by blowing clean air stream through loaded filter media at different velocities. Riefler [15] investigated particle penetration of filters clogged with standard dust particles and discovered an exponential decay of the penetration depth of particles. However, all these studies focused on the clogging of high-efficiency filters and the structural characterization of clogged coarse filters remained undiscovered.

Besides, it is important to characterize the pore structure of clogged filters to understand the effect of clogging on filter structure. Pore area could be obtained from the 2D images like SEM [16] or XMCT tomograms [17] and the diameter of an equivalent circle with the same area could be considered as the pore diameter. However, this pore diameter is limited to 2D. Another method could obtain 3D pore diameter by filling the largest sphere into the pore space within the 3D fibrous structure obtained from DVI [18], but it has not considered the thickness through the entire path of the pore and DVI is not suitable for characterization of the filter containing particles due to the structure deformation caused by sample cutting. Huang et al. [19] studied the 3D pore diameter by

skeletonizing the pore structure of the fibrous structure obtained from XMCT, which provided an ideal method to study the complex pore structure of clogged fibrous filters.

In this study, XMCT was utilized to visualize and analyze the 3D structure of fibrous nonwoven coarse filters at different clogging stages to study the clogging process during solid particle loading. Fiber and particle solidity of each smallest volume across filter thickness were derived from 3D XMCT images and quantitatively analyzed. In this way, particle solidity distribution at different clogging stages was compared to study the evolution of coarse filter structures and the clogging process. Additionally, 3D pore diameter distribution was generated and compared for coarse filter structures with and without particles deposited using image segmentation tools. Further summarized clogging process based on the above information regarding fiber solidity distribution, particle solidity distribution, and 3D pore diameter distribution can be used to create models describing the clogging of coarse filters to guide the design of coarse filters as well as gradient filters, which would contribute to future filters with high filtration efficiency, low pressure drop and high dust holding capacity.

3.2.Materials and methods

3.2.1. Characterization of clean filter media

The studied fibrous nonwoven coarse filter was composed of polypropylene (PP) and binder fiber with a blend ratio of 70/30 (PP/binder). The PP fiber had 11.6 μm (1.5 Denier) fiber diameter, 38 mm (1.5 inches) fiber length and 0.946 g/cm^3 density. The binder fiber had 14.3 μm (2 Denier) fiber diameter, 38 mm (1.5 inches) fiber length and 1.380 g/cm^3 density. The filter was manufactured using carding for web formation and through air (TA) thermal bonding for fibrous web consolidation. The areal density was designed to be 50 g/m^2 and the thickness was controlled

by a 1 mm gap, which limited the thickness of coarse filter TA a maximum value of 1 mm. All the structure parameters are listed in Table 3.1.

Table 3.1. Structure parameters of studied fibrous nonwoven coarse filter TA.

	Coarse filter TA
Fiber diameter, PP (μm)	11.6
Fiber density, PP, ρ_1 (g/cm^3)	0.946
Fiber diameter, binder (μm)	14.3
Fiber density, binder, ρ_2 (g/cm^3)	1.380
Blend ratio R_1/R_2 (PP/binder)	70/30
Filter basis weight (g/m^2)	51.4 ± 1.1
Filter thickness (μm)	890.6 ± 13.9
Filter fiber solidity, Sf (%)	5.36
Mean pore diameter (μm)	94.3

The basis weight of the coarse filter TA was then measured according to ASTM 3776 Standard Test Methods for Mass Per Unit Area (Weight) of Fabric. The mass of 5 sample replicates, each with a 100 cm^2 area, was measured and an average was calculated to be 51.4 g/m^2 with a standard deviation of 1.1 g/m^2.

The thickness of the filter TA was measured according to ASTM D 1777 Standard Test Method for Thickness of Textile Material by a thickness gauge with a low pressure of 15 Pa applied. 10 test replicates were carried out and an average was calculated to be 890.6 μm with a standard deviation of 13.9 μm.

The fiber solidity (fiber packing density) is a parameter to evaluate the compactness of the porous structure. It was calculated according to the following equation:

$$Sf = \frac{m}{H*(R1*\rho1+R2*\rho2)}$$, (3.1)

where the Sf is the fiber solidity of the sample, H is the thickness of the sample, R_1 is the PP blend ratio, ρ_1 is the PP density, R_2 is the Binder blend ratio and ρ_2 is the Binder density. The calculated Sf was 5.36 % as presented in Table 3.1.

The pore diameter distribution was measured using PMI liquid capillary porosimetry (Porous Materials Inc., U.S.).

3.2.2. Loading filter media with standard solid particles

The Palas MFP 3000 Filter Tester Rig (Palas GmbH, Germany) was used to load solid particles and to analyze the particle loading behaviors of the studied fibrous nonwoven coarse filter TA. This equipment can measure the dynamic change of differential pressure and filtration efficiency during continuous solid particle loading. It was consisted of a rotating brush particle generator (RBG 1000), a particle counting system (Welas 3000) with both upstream and downstream optical particle counter (2070 sensor), a differential pressure detector, a test filter holder, a gravimetric filter holder, and a suction pump, as shown in Figure.3.1.

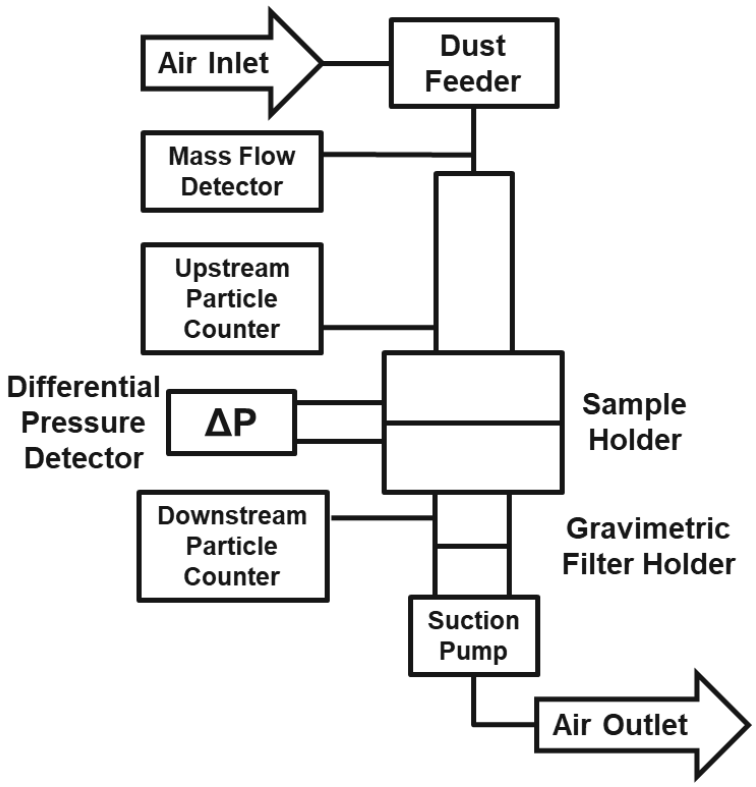

Figure.3.1. Equipment set-up for particle loading.

Clean air was first fed to the system. The piston containing solid particles was pushed upward at a constant speed so the particle feeding rate could be kept constant. The particles were then continuously generated by the rotating brush and fed through the air stream. As the particles were loading to the test filter and penetrating the test filter, the particle number before the penetration, p_1, was measured by the upstream particle counter. The particle number after the penetration, p_2, was measured by the downstream particle counter. The overall numerical efficiency, E, could then be calculated according to the following equation:

$$E = \frac{p1-p2}{p1} \text{ . (3.2)}$$

Meanwhile, the pressure drop across the test filter was measured by the differential pressure detector continuously. The test sample holder had a circle shape with an area of 100 cm^2, so the loaded area of the test filter was the same. All the penetrated particles would eventually be captured by the gravimetric filter to protect the testing system.

The testing standard ISO 5011 Inlet Air Cleaning Equipment for Internal Combustion Engines and Compressors was followed. Three individual measurements were carried out under the same testing conditions of 20 cm/s air face velocity, 120 L/min airflow, and 200 mg/m^3 particle concentration. The ISO 12103-1 Arizona Fine Test Dust (Power Technology Inc., USA), standard test dust containing 70% of silica in terms of mass, was used in the testing. It has a nominal size of 0 to 80 µm. Volume-based particle size distribution also indicates its bimodal distribution with two peaks at around 4 µm and 20 µm.

3.2.3. Imaging of clean and loaded filter media

3.2.3.1. Optical microscopy

The surface and cross-section observations of particle-loaded coarse filter TA were carried out using the Keyence Optical Microscopy (Keyence, Japan) with 300X magnification for surface imaging and 100X for cross-section imaging.

3.2.3.2. X-ray micro-computed tomography

XMCT was used for 3D imaging and 3D structure characterization of both clean and clogged coarse filters. Samples were scanned at the University of Texas High-Resolution X-ray Computed Tomography Facility using the Xradia 400 system (Zeiss, Germany). X-ray source with 10 W and

90 kV photon energy was used for the scans. To visualize and analyze particles larger than 1 μm that occupied the major mass and volume, the resolution was set up as 1 μm/pixel. The scanned spatial volume was thereafter limited to 1000 μm*1000 μm*1000 μm. Therefore, samples with a dimension of 3 mm*3 mm were cut from the clean and loaded filter samples so that the outer edges deformed by the sample cutting won't be scanned. As a substance with higher density and thickness causes higher X-ray attenuation, a high concentration of dust particles contained in heavily loaded coarse filters at the surface filtration stage would absorb much X-ray energy, thus making the fibrous structure difficulty to be characterized under attenuated low X-ray energy. As a result, only the filters with relatively light and medium particle loading at the initial depth filtration stage and transition stage from the depth filtration to the surface filtration were scanned by the XMCT. One clean filter (7 Pa initial differential pressure) and four filters at different particle loading stages (10 Pa, 30 Pa, 50 Pa, and 100 Pa differential pressure respectively) were scanned by the XMCT. The number of tomograms was 959, 969, 971, 973 and 969 respectively.

3.2.3.3. Image processing and image analysis

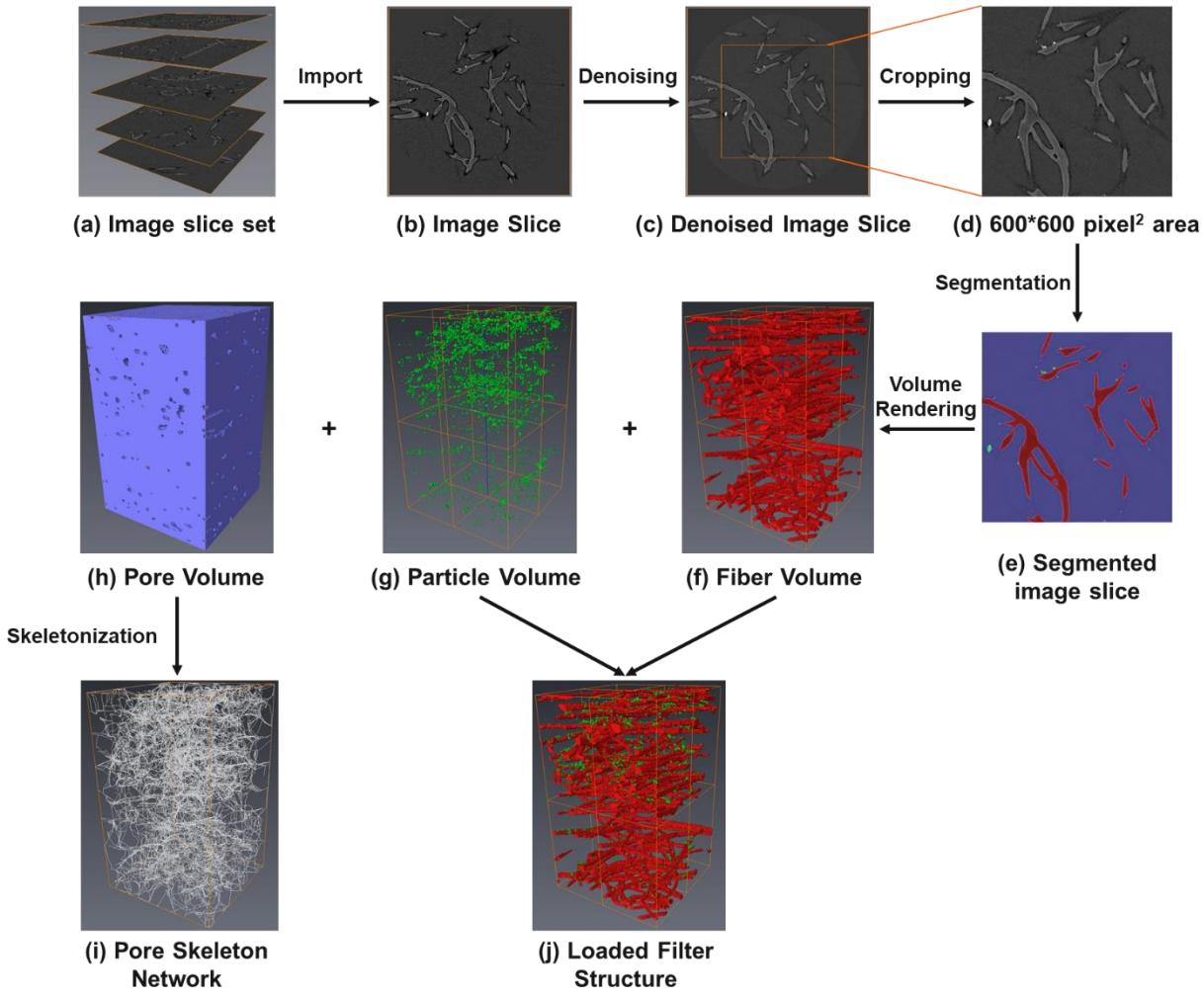

Figure.3.2. Image processing and image analysis procedures of XMCT images.

The image processing procedures of XMCT tomograms are shown in Figure.3.2, where the image processing software Avizo® was used. After the image slices or tomograms as shown in Figure.3.2 a were imported to Avizo, the whole image slice set could be processed simultaneously. Denoising process with a combination of median filter and closing process (dilation then erosion) was applied to remove the background noises of original image slices in Figure.3.2 b. This closing process was

used to reduce the fact that some inner parts of fibers exhibited low gray values which were very close to those of pores. This fact was caused by the reflection of X-ray photons of the curved fiber surfaces [13]. The research of interest area was then resized by cropping the denoised image slices in Figure.3.2 c, then image slices with 600*600 pixel^2 area Figure.3.2 d were obtained.

The segmentation process was then applied to separate the three components of the 3D structure of clogged coarse filters, i.e. fibers, particles, and pores. Due to the different attenuation rates of these three substances caused by different material densities, pores had low gray value, while fibers had medium gray value and particles had ultra-high gray value, which corresponded to the dark area, gray area and bright area respectively in the image slices. The brightness and contrast of Figure.3.2 a to d were increased for better visualization. In this study, the thresholding tool was used to choose the threshold range of gray value to determine and select the target substance within that threshold range. Manual processing was also applied to select the low gray value inner parts of fibers in case these parts were not removed by the closing process and were determined as pores. After the segmentation, the original image slices with a wide range of gray values were segmented into the fiber (red), particle (green) and pore (purple) as shown in Figure.3.2 e.

Then individual fiber volume Figure.3.2 f, particle volume Figure.3.2 g and pore volume Figure.3.2 h were generated from the segmented image slices Figure.3.2 e by the volume rendering process. With the skeletonization process, the axis of each pore from the pore volume was considered as the pore skeleton and a pore skeleton network in Figure.3.2 i composed of all the pore skeletons was generated. A 3D loaded filter structure Figure.3.2 j could also be visualized by combing the segmented fiber volume and the particle volume together using the software Avizo.

3.3. Results and discussion

3.3.1. Evolution of filtration properties during the particle loading process

The evolution of the dynamic filtration properties, i.e. differential pressure Figure.3.3 a, number efficiency Figure.3.3 b, mass efficiency Figure.3.3 c and fractional efficiency Figure.3.3 d, of the studied filter TA, is described in Figure.3.3. Overall, the differential pressure, number efficiency and mass efficiency increase along with the particle loading over time. The loaded mass was calculated by the Palas testing system according to the total mass of particles captured by the test filter and gravimetric filter at the end of the test. It had a linear increase in relationship with time. The number efficiency was much lower than the mass efficiency at the same loaded mass, which accounted for the low efficiencies for small particles and the high efficiencies for large particles, as indicated in Figure. 3.3 d. This diagram further illustrates although the studied filter TA was a coarse filter, the large particles were still effectively captured and trapped by the test filter. It also shows the rapid growth of fractional efficiency at various particle sizes as the filter got clogged during the particle loading process.

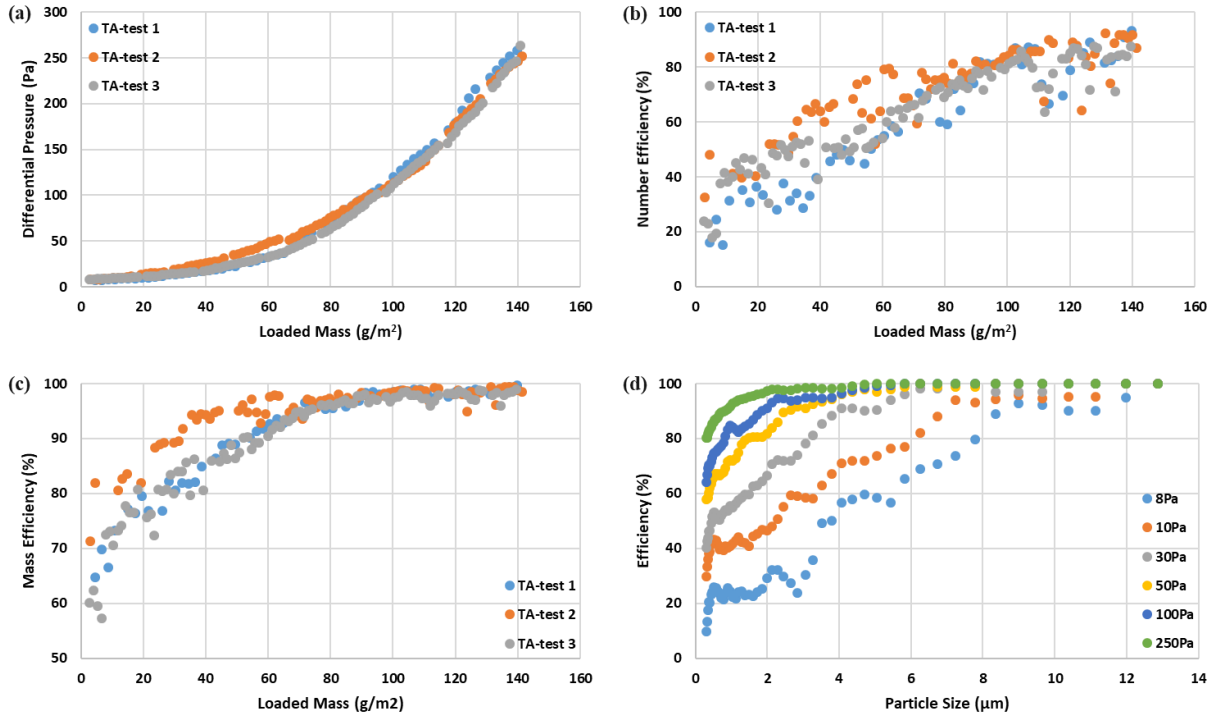

Figure.3.3. Evolution of filtration properties of filter media TA: (a) differential pressure vs. loaded mass, (b) number efficiency vs. loaded mass, (c) mass efficiency vs. loaded mass, (d) fractional efficiency vs. particle size.

3.3.2. Surface and cross-section observations of the filters at different clogged stages

In Figure.3.4, surface observation: (a) 10 Pa, (b) 30 Pa, (c) 50 Pa, (d) 100 Pa and cross-section observation (e) 10 Pa, (f) 30 Pa, (g) 50 Pa and (h) 100 Pa of the filter TA at four different clogged stages were presented. In surface (a), light loaded particles could be found on the filter and dendritic branches just started growing; in surface (b), the dendritic branches had grown, and branches started to entangle with one another fiber or particle branch; in surface (c), many fibers were covered by the particles and inter-fiber pores had been partially filled by particles; in surface (d), inter-fiber pores had been filled in a higher degree. In cross-section (e), particles could be

hardly found in the image; in cross-section (f), particles could be found in the top part and middle part, however, no significantly high concentration of particles could be found in bottom part; in cross-section (g), significant particle concentration could be found in the bottom part; cross-section (h), high particle concentration could be found across the filter thickness. Eventually, at 100 Pa, almost the full thickness of filter TA was utilized for capturing and holding dust particles, which accounted for the high dust holding capacity of this nonwoven filter media due to its low fiber solidity and loose structure. These surface and cross-section observations offered a comprehensive view and understanding of the structural evolution of particle-loaded coarse filters at different clogging stages.

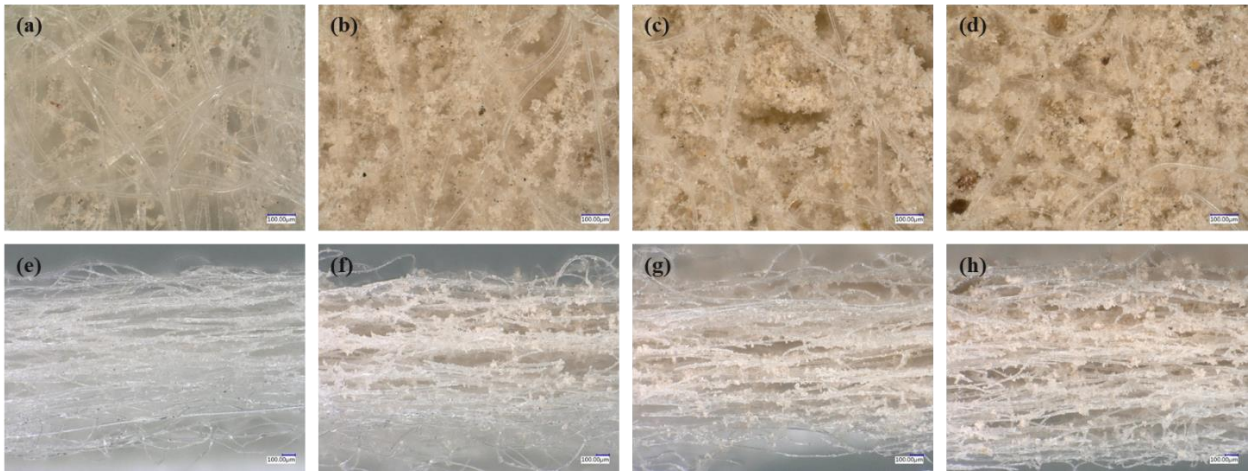

Figure.3.4. Optical microscopic images of studied filter media at different clogging stages for surface observation: (a) 10 Pa, (b) 30 Pa, (c) 50 Pa, (d) 100 Pa and cross-section observation: (e) 10 Pa, (f) 30 Pa, (g) 50 Pa and (h) 100 Pa.

3.3.3. 3D structure visualization of clean and loaded filter media

The XMCT tomograms were processed following the procedures described in section 3.2.3.3 and the corresponding 3D clean and loaded filter structures were presented in Figure.3.5. Structure evolution of filter TA during the particle loading process can be observed from these XMCT images. At 10Pa, the beginning of particle loading, the minimum number of particles was deposited on the filter media and most of them were deposited on the top part of the filter structure. At 30Pa, particles were found through almost the full thickness of filter TA, in contrast, no significantly high concentration of particles was observed from 2D optical microscopic images. Because the XMCT can be used to visualize the whole 3D volume, while optical microscopy can only be utilized to observe the 2D cross-section. At 50Pa, a high concentration of particles was found in both the middle and bottom parts. At 100Pa, particle concentration higher than that of 50Pa was found in all top, middle and bottom parts through the filter thickness, which was in good agreement with optical microscopic observation. After the direct visualization from the XMCT images of the coarse filter TA at different particle loading stages, the next objective is to derive structural information and to quantitatively characterize the structure evolution based on these 3D filter structures.

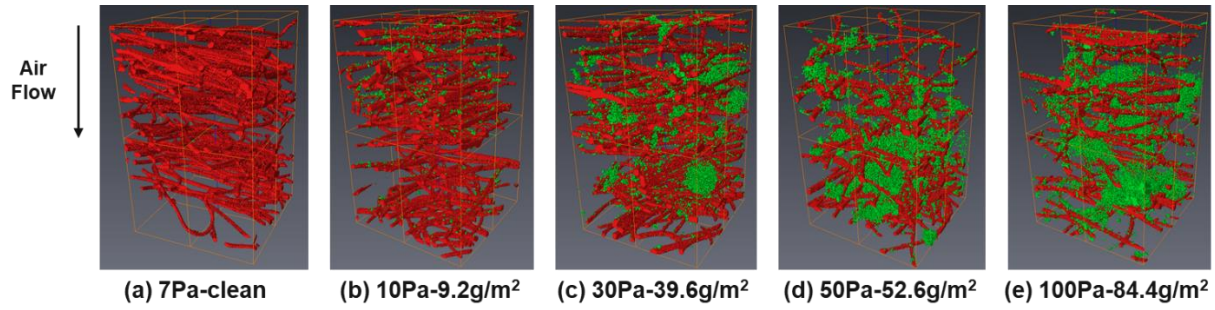

Figure.3.5. 3D structure visualization of clean and loaded filter media from XMCT images: (a) 7Pa-clean, (b) 10Pa-9.2g/m^2, (c) 30Pa-39.6g/m^2, (d) 50Pa-52.6g/m^2, and (e) 100 Pa-84.4g/m^2.

3.3.4. Fiber and particle solidity distribution analysis

After segmentation, the fiber solidity, particle solidity and pore volume fraction of each slice with 1 µm thickness could be derived from the XMCT image slice set. The solidity distribution or volume fraction distribution of fiber, particle, and pore could be drawn respectively. The fiber solidity distribution of clean filter TA was shown in Figure.3.6. In this diagram, fiber solidity varied from a minimum value of 0.95 % to a maximum value of 12.26 %, with an average of 5.21 ± 2.41 % as presented in Table 3.2, which was rather heterogeneous.

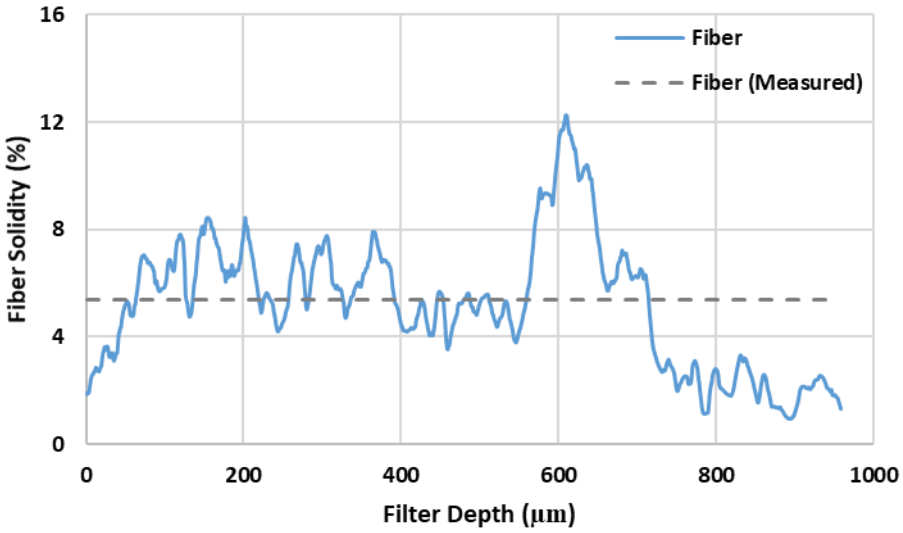

Figure.3.6. Fiber solidity distribution through the filter depth of clean filter TA.

Table 3.2. Average fiber and particle solidity of clean and loaded filter media from XMCT images.

	Clean	10Pa	30Pa	50Pa	100Pa
Average fiber solidity (%)	5.21 ± 2.41	5.50 ± 2.78	5.51 ± 2.92	3.27 ± 2.09	3.08 ± 2.08
Minimum fiber solidity (%)	0.95	0.53	0.74	0.11	0.00
Maximum fiber solidity (%)	12.26	11.23	15.38	10.51	9.58
Average Particle Solidity (%)	/	0.14 ± 0.13	0.50 ± 0.27	0.74 ± 0.47	1.40 ± 0.99
Minimum particle solidity (%)	/	0.00	0.03	0.00	0.00
Maximum particle solidity (%)	/	0.72	1.28	2.63	3.41

Fiber solidity distribution of coarse filter TA at different clogging stages could also be obtained after the fiber components and particle components were separated with the segmentation process as shown in Figure.3.7. Wide data range and high standard deviation could be found in all the samples of TA-10 Pa, TA30 Pa, TA-50 Pa, and TA-100 Pa, which could confirm that fiber solidity distribution of all the studied samples was rather heterogeneous. One reason for this phenomenon was the limited XMCT scan dimension, as the fiber solidity distribution or porosity distribution would be less heterogeneous and more uniform under a larger scan dimension which was confirmed in a previous study [Wang 2018]. The other reason is the existence of an incomplete layer. As the surface of filter TA was rough, and incomplete layer composed of some fibers could exist on the top or bottom surface of the filter sample since the studied samples had not been processed by surface calendaring. When the XMCT was scanning the whole 3D structure of clean and loaded filter TA, those incomplete layers would be scanned and considered as part of the structure, which led to ultra-low fiber solidity of continuous thickness across the filter depth. Direct observations of incomplete layer and rough surface of filter TA could also be found in the cross-section images in Figure.3.4.

As the measured fiber solidity of clean filter TA was 5.36%, the average fiber solidity of TA-clean, TA-10 Pa and TA-30 Pa were in good agreement with the measurement, which proves that the XMCT is an effective technique of solidity characterization. However, it is required to be cautious about the sample variation when applying the XMCT scan. The average fiber solidity of TA-50 Pa and TA-100 Pa were much lower than other data points obtained from 3D images. One reason for this fact is the variation of basis weight uniformity of nonwovens when it happened that a low basis weight area or weak point was captured by the XMCT scan. On the other hand, the XMCT scan area in this study was limited at the high resolution. Although high-resolution scanning was able to capture the information of small particles, it also reduced the scan area. However, the high resolution is still required for the imaging of particles captured by filter media. Otherwise, those particles would not be able to be visualized under low resolution. Overall, in this study, it is recommended to focus on the particle solidity distribution evolution and comparison of clogging conditions instead of the effect of the initial filter structure on the clogging.

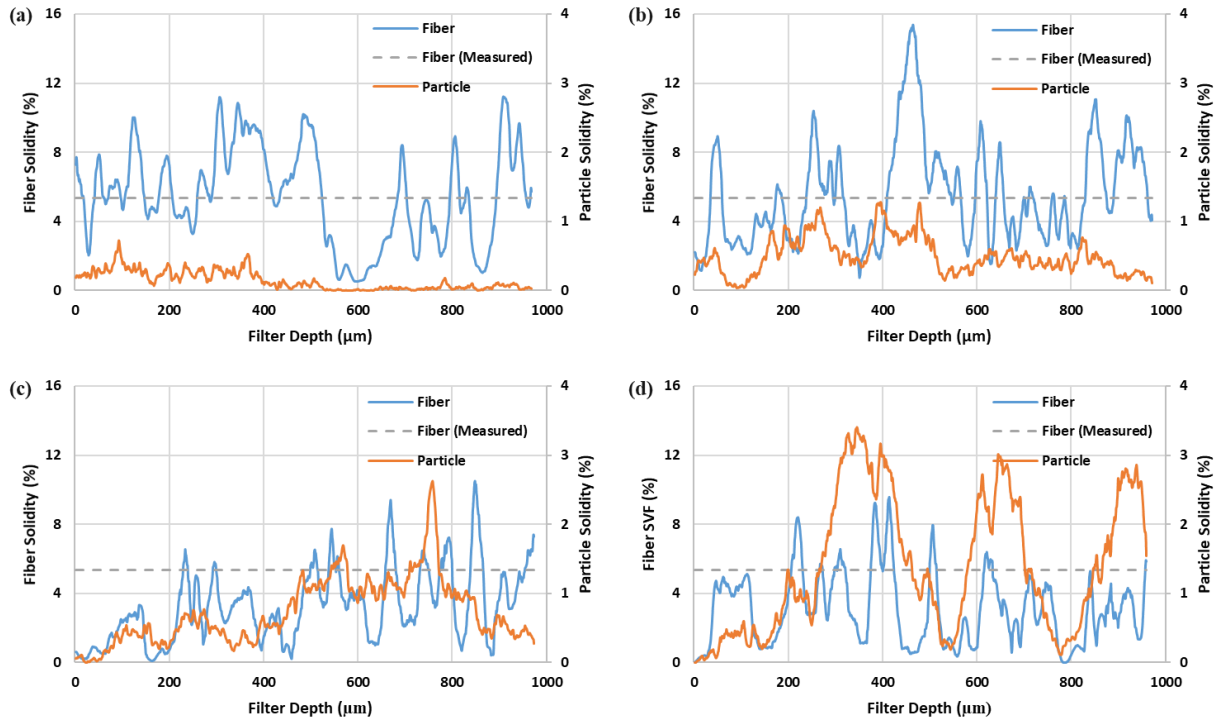

Figure.3.7. Fiber and particle solidity distribution through filter depth of filter TA at different particle loading stages: (a) 10 Pa, (b) 30 Pa, (c) 50 Pa and (d) 100 Pa.

A 'Dimensionless Time' was used to verify if the particle solidity data obtained from the XMCT images fit the deposited mass data obtained from the experimental particle loading tests. The calculation of this Dimensionless Time at 10Pa followed equation 3.3 as an example.

Dimensionless Time of Deposited Mass at 10Pa = Deposited mass (Particle solidity) at 10Pa / Loaded mass (Particle solidity) at 100 Pa (3.3),

where the dimensionless time of deposited mass and particle solidity at 100Pa are both 1.

The data on the dimensionless time of deposited mass and particle solidity is shown in Table 3.3 and plotted in Figure.3.8. It is obvious that the exponential curve of the differential pressure-dimensionless time of deposited mass perfectly fits the exponential curve of the differential

pressure-dimensionless time of particle solidity. As a result, it can be claimed that the particle solidity data obtained from the XMCT images reflected the evolution of particle deposition in the studied filter TA.

Table 3.3. Dimensionless time of loaded mass and particle solidity.

	Deposited mass (g/m^2)	Dimensionless time of deposited mass	Particle solidity (%)	Dimensionless time of particle solidity
TA-10Pa	10.9	0.136	0.72	0.211
TA-30Pa	40.7	0.507	1.28	0.375
TA-50Pa	57.0	0.711	2.63	0.771
TA-100Pa	80.2	1	3.41	1

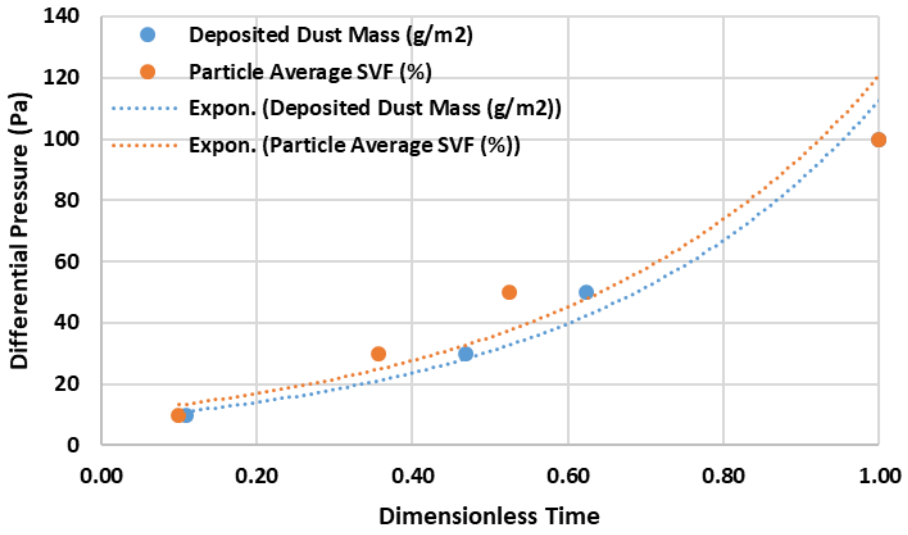

Figure.3.8. Progress ratio of loaded mass and particle solidity.

Like the heterogeneous fiber solidity distribution, wide data range and high standard deviation can also be found for particle solidity distribution in Table 3.2. The particle solidity distribution diagrams of TA-10 Pa, TA-30 Pa, TA-50 Pa, TA-100 Pa had been combined in the same diagram as shown in Figure.3.9. For the clogging of a studied coarse filter, most particles were trapped in the top part at the beginning of particle loading as shown from the TA-10 Pa diagram. In the early particle loading stage, as shown from the TA-30 Pa diagram, solid particles had reached the deep bottom part of filter depth, while a higher number of particles were still trapped in the top part. Unlike the findings from previous literature [Thomas 2001, Leung 2012, Riefler 2018] regarding the clogging of high-efficiency fine fibrous filters that most particles were captured by top part, most solid particles were found being trapped in the bottom part and caused clogging, as shown from the peak in TA-50 Pa diagram, during the transition stage from depth filtration to surface filtration. With further particles loaded, clogging occurred from the bottom part to the middle part of the coarse filter as shown from the TA-100 Pa diagram. For coarse filters with even more particles loaded, the particles would almost completely cover the surface of fibers which would make the image quality too poor to be processed. Because a high concentration of silicon particles leads to high attenuation of X-ray, which allows minimum X-ray to penetrate the fibers. As a result, no further XMCT scan had been carried out on the coarse filter TA with even more particle loaded. However, it can still be estimated that with further particle loading, the top part would be clogged, and a surface cake would start forming thereafter, which follows the filtration theory of fine filter media [Brown, 1993].

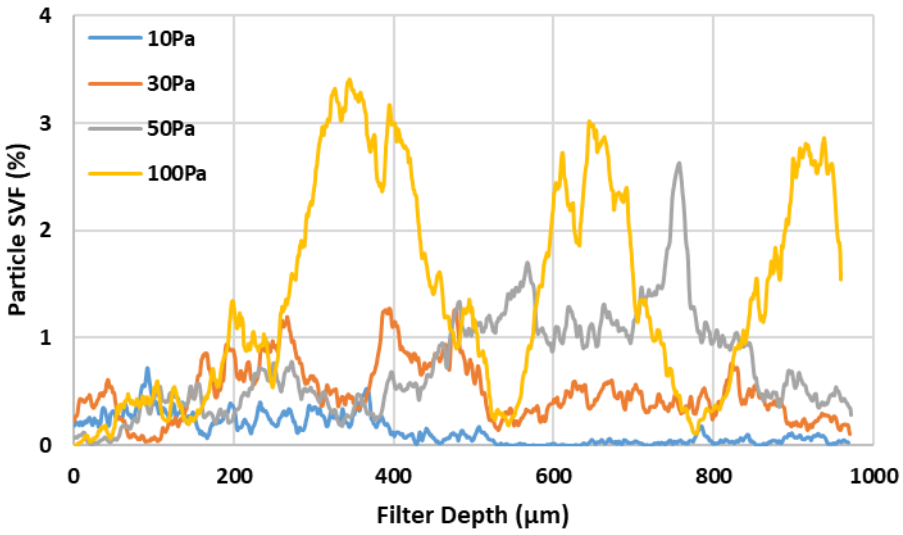

Figure.3.9. Evolution of particle solidity distribution through filter depth.

3.3.5. Pore diameter distribution analysis

The pore diameter distribution from PMI liquid porosimetry Figure.3.10 a. and image analysis Figure.3.10 b. of clean coarse filter TA with no particles loaded are both presented in Figure.3.10. The mean pore diameter measured from the liquid porosimetry was 94.3 µm. The average pore diameter directly obtained from the pore skeleton network was 65.7 µm. During the particle loading process, particles trapped in the coarse fibrous filter structure would change the original filter structure and cause many small pores. These small pores would not affect the filtration properties and filtration process due to their small volume. However, these small pores would significantly affect the original average pore diameter. The volume-based average pore diameter was then calculated to represent the average pore diameter of coarse fibrous filters using the following equation:

$$D = \frac{D1*V1+D2*V2+\cdots+Dn*Vn}{V1+V2+\cdots+Vn}, \quad (3.4)$$

where D is the volume-based average pore diameter, D_1 the diameter of pore 1, V_1 the volume pore 1, D_2 the diameter of pore 2, V_2 the volume pore 2, Dn the diameter of pore n, Vn the volume pore n. The pore diameter and pore volume of individual pores could be obtained from the pore skeleton network. The volume-based average pore diameter of the clean coarse filter TA was 107.6 µm. The liquid porosimetry was underestimating the pore diameter due to the mechanism of the bubble point method, while the volume-based average pore diameter was overestimating the pore diameter because the scanned thickness was larger than the measured thickness. This could be supported by the difference between the measured thickness of filter TA, 890.6 ± 13.9 µm, as shown in Table 3.1 and the thickness of scanned 3D volume varying from 959 µm to 973 µm. Despite the difference in the result of the average pore diameter, the data from liquid porosimetry and image analysis were still very close and in good agreement. Therefore, volume-based average pore diameter from the pore skeleton network can work as an effective characterization method of the pore structures of clean and loaded coarse filters.

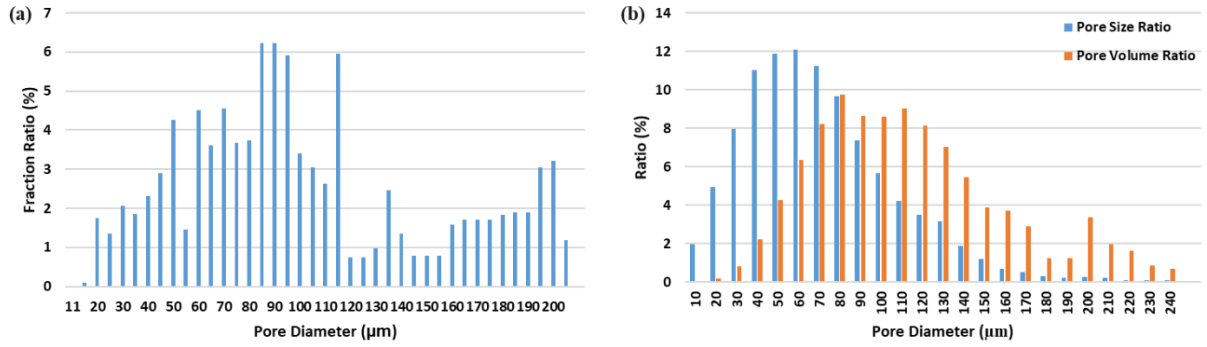

Figure.3.10. Pore diameter distribution of clean filter media from (a) PMI liquid porosimetry (b) XMCT image analysis.

With the segmentation process, the fiber volume (e.g. Figure.3.2 f.) can be considered as the clean filter without particle loading. If the fiber volume added up with the particle volume (e.g. Figure.3.2 g.), the resulted whole volume (e.g. Figure.3.2 j.) can be considered as the filter loaded with particles. Both the clean and loaded version of each scanned 3D volume was then divided into top part (top 1/3 volume), middle part (middle 1/3 volume) and the bottom part (bottom 1/3 volume) with Avizo. The average pore diameter for each cropped part was calculated with the method described earlier in this section. The results are shown in Figure.3.11 a. The ratio of pore diameter reduction was then calculated according to the following equation 3.5, which is more meaningful than the original average pore diameter data in terms of analyzing the filter structure evolution during the particle loading process. The ratio of pore diameter reduction data is shown in Figure.3.11 b.

$$\text{Ratio of pore diameter reduction} = (\text{Diameter}_{clean} - \text{Diameter}_{loaded}) / \text{Diameter}_{clean} \quad (3.5)$$

As another aspect of characterizing filter structure evolution, the findings from the ratio of pore diameter reduction is in good agreement with those from particle solidity distribution. At 10Pa, the ratio of the top part was higher than that of middle and bottom, which corresponded to the fact that most particles were captured by the top part at this stage. At 30Pa, although the particle solidity was higher in the top and middle part, the ratio of the bottom part was about the same ratio of the middle part and it was higher than the ratio of the top part. This fact was ascribed for the beginning of clogging formation, where a particle cluster could be seen in the bottom part in Figure.3.5 c. Such particle clusters clogged filter structures and thereafter caused an increase in pressure drop. At 50Pa, the ratio of the bottom part was higher than the ratio of the middle part and top part, which corresponded to the existence of high particle concentration in the bottom part, where the bottom part was getting clogged. At 100Pa, the ratio of the bottom part and the middle part was

much higher than that of the top part, because the bottom part was estimated to be fully clogged and the middle part was still getting clogged, while the top part just started clogging. Overall, the ratio of pore diameter reduction and particle solidity distribution is in good agreement. Furthermore, the clogging occurred in the filter structures blocked the airflow and therefore increased the pressure drop during filtration, although the total solidity (fiber solidity + particle solidity) remained less than 10%.

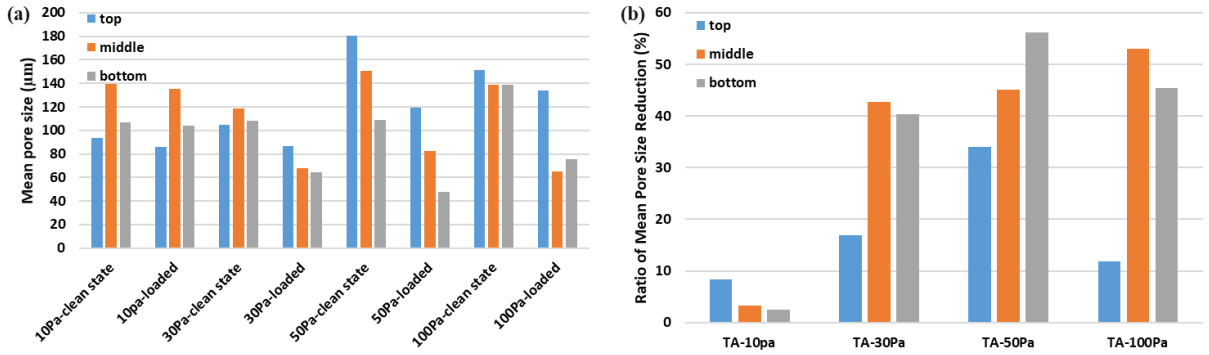

Figure.3.11. (a) Average pore diameter and (b) ratio of average pore size change.

3.4. Conclusions

Three particle loading measurements of the studied coarse filter were carried out. The differential pressure, number efficiency, and mass efficiency increase along with the particle loading. Fractional efficiencies of large particles are higher than fractional efficiencies at small particles. The fractional efficiency at small particle size improves rapidly during particle loading.

Fiver samples consisted of clean and particle-loaded coarse fibrous filters at different clogging stages, 10 Pa, 30 Pa, 50 Pa, and 100 Pa, which were scanned by the XMCT. The fiber solidity from

measurement and image analysis were in good agreement, which proves that XMCT is an effective technique on solidity characterization. Wide data range and high standard deviation of fiber solidity indicated its rather heterogeneous distribution, where this heterogeneous fiber solidity distribution should be taken into consideration for the modeling of solid particle filtration and loading process. A similar wide data range and high standard deviation of particle solidity also indicate its rather heterogeneous distribution during the clogging process. Particle distribution diagrams from coarse fibrous filters at different clogging stages shows that at the beginning and early particle loading stages, particles were mostly trapped in the top part of filter depth, which followed previous literature regarding the clogging of fine filters. However, in the particle loading stage of transitioning from depth filtration to surface filtration, most particles were trapped in the bottom part. As more particles were loaded, high particle concentration occurred in the middle part. The close surface part facing airflow would then be clogged by particles and surface cake would start forming thereafter. This is the first report of the clogging process of the coarse fibrous coarse filter.

The skeletonization process was used to generate the pore skeleton network of 3D pore structure from the XMCT scan. Pore diameter and pore volume of each pore in the 3D pore structures were obtained. The mean pore diameter measured from PMI liquid porosimetry and volume-based average pore diameter obtained from image analysis of XMCT images were in good agreement. The average pore diameter and volume-based average pore diameter obtained by the image analysis of XMCT scans could contribute to the modeling of particle-loaded filter structures and guide the design of both coarse coarse filters and gradient filters with better filtration performance.

References

[1] Walsh, D. C., Stenhouse, J. I. T., Scurrah, K. L., & Graef, A. (1996). The effect of solid and liquid aerosol particle loading on fibrous filter material performance. Journal of Aerosol Science, (27), S617-S618.

[2] Thomas, D., Penicot, P., Contal, P., Leclerc, D., & Vendel, J. (2001). Clogging of fibrous filters by solid aerosol particles experimental and modeling study. Chemical Engineering Science, 56(11), 3549-3561.

[3] Leung, W. W. F., & Hung, C. H. (2012). Skin effect in nanofiber filtration of submicron aerosols. Separation and Purification Technology, 92, 174-180.

[4] Saleh, A. M., Hosseini, S. A., Tafreshi, H. V., & Pourdeyhimi, B. (2013). 3-D microscale simulation of dust-loading in thin flat-sheet filters: a comparison with 1-D macroscale simulations. Chemical Engineering Science, 99, 284-291.

[5] Bourrous, S., Bouilloux, L., Ouf, F. X., Appert-Collin, J. C., Thomas, D., Tampère, L., & Morele, Y. (2014). Measurement of the nanoparticles distribution in flat and pleated filters during clogging. Aerosol Science and Technology, 48(4), 392-400.

[6] Jabri, W., Vroman, P., & Perwuelz, A. (2015). Study of the influence of synthetic filter media compressive behavior on its dust holding capacity. Separation and Purification Technology, 156, 92-102.

[7] Shim, E., Pourdeyhimi, B., & Latifi, M. (2010). Three-dimensional analysis of segmented pie bicomponent nonwovens. The Journal of The Textile Institute, 101(9), 773-787.

[8] Gervais, P. C., Bourrous, S., Dany, F., Bouilloux, L., & Ricciardi, L. (2015). Simulations of filter media performances from microtomography-based computational domain. Experimental and analytical comparison. Computers & Fluids, 116, 118-128.

[9] Jing, H., & Yu, W. (2018). Estimation of fiber orientation and length distribution in cashmere fibrous assemblies. Textile Research Journal, 0040517518763987.

[10] Soltani, P., Johari, M. S., & Zarrebini, M. (2015). 3D fiber orientation characterization of nonwoven fabrics using X-ray micro-computed tomography. World J. Text. Eng. Technol., 1, 41-47.

[11] Zhu, L., Wang, X., Hinestroza, J. P., & Naebe, M. (2018). Determination of the porosity in a bifacial fabric using micro-computed tomography and three-dimensional reconstruction. Textile Research Journal, 88(11), 1263-1277.

[12] Charvet, A., Du Roscoat, S. R., Peralba, M., Bloch, J. F., & Gonthier, Y. (2011). Contribution of synchrotron X-ray holotomography to the understanding of liquid distribution in a medium during liquid aerosol filtration. Chemical Engineering Science, 66(4), 624-631.

[13] Gervais, P. C., Poussier, S., Bardin-Monnier, N., Karcher, G., & Thomas, D. (2014). Combination of Single-Photon Emission and X-Ray Computed Tomography to visualize aerosol deposition in pleated filter. Separation and Purification Technology, 126, 52-61.

[14] Jackiewicz, A., Jakubiak, S., & Gradoń, L. (2015). Analysis of the behavior of deposits in fibrous filters during non-steady state filtration using X-ray computed tomography. Separation and Purification Technology, 156, 12-21.

[15] Riefler, N., Ulrich, M., Morshäuser, M., & Fritsching, U. (2018). Particle penetration in fiber filters. Particuology, 40, 70-79.

[16] Xu, B. (1996). Measurement of pore characteristics in nonwoven fabrics using image analysis. Clothing and Textiles Research Journal, 14(1), 81-88.

[17] Théron, F., Lys, E., Joubert, A., Bertrand, F., & Le Coq, L. (2017). Characterization of the porous structure of a non-woven fibrous medium for air filtration at local and global scales using porosimetry and X-ray micro-tomography. Powder Technology, 320, 295-303.

[18] Jaganathan, S., Tafreshi, H. V., Shim, E., & Pourdeyhimi, B. (2009). A study on compression-induced morphological changes of nonwoven fibrous materials. Colloids and Surfaces A: Physicochemical and Engineering Aspects, 337(1-3), 173-179.

[19] Huang, X., Wang, Q., Zhou, W., Deng, D., Zhao, Y., Wen, D., & Li, J. (2015). Morphology and transport properties of fibrous porous media. Powder Technology, 283, 618-626.

CHAPTER 4. Effect of Basis Weight of Meltblown Nonwoven Filter Media on Filtration Properties and Particle Deposition Distribution

Abstract

Meltblown nonwoven filter media with different basis weight were produced and loaded with standard dust particles for this study. It was found that higher basis weight leads to faster pressure drop increase, higher filtration efficiency during filtration and lower dust holding capacity at the end. However, the increase in filtration efficiency cannot compensate for the increase in resistance.

Filter samples with different basis weight captured the same mass of standard dust particles and then those samples were sent to the X-ray micro-computed tomography (XMCT) for 3D structure visualization and analysis. Direct thickness measurement of textured filter structure was overestimated, while a reorganized 3D filter structure from XMCT imaging offered more accurate filter thickness. The increase of filter basis weight only causes a slight increase in structure compactness.

Particle deposition was also analyzed based on XMCT images. Most of the particles are captured by a given thickness of a top part of the filter structure, despite the filter basis weight and thickness. Besides, more particles were captured at the same dimensionless ratio of filter depth by filter with higher basis weight.

In one sentence, both the particle loading behaviors and particle deposition profiles are recommended to control and limit the basis weight of melt-blown nonwoven filter media for filter design if the desired filtration efficiency can be obtained.

Keywords: Meltblown nonwoven filter media, particle loading behavior, filter solidity, particle deposition

4.1.Introduction

Fibrous filters are commonly used for various air filtration applications and nonwoven filter media is a major component of the fibrous filters. Meltblown technology enables bulk production of fine fiber nonwoven filter media [1]. Basis weight is one of the most important structural properties of nonwoven filter media to evaluate its areal density, i.e. mass per unit area. Basis weight can also affect the filtration properties of nonwoven filter media. Brown concluded in his book that an increase of basis weight led to increasing in initial filtration efficiency, however, it also led to a decrease in initial quality factor, indicating a worse comprehensive filtration performance considering both filtration efficiency and pressure drop [2]. Besides, many reported the role of basis weight on the initial performance of various nonwoven filter media. However, limited research was carried out regarding the effect of basis weight on the dynamic filtration performance. Leung [3] utilized to study the effect of filter basis weight on the loading behaviors. However, electrospinning technology was mostly applied which cannot represent microfiber filter media dominating the current filter market. The same group also used melt-blown nonwoven filter media in their studies [4], but only nanoparticles were used which cannot represent general air filtration application, which was not commonly existed. Overall, it is necessary to study the effect of the basis weight of melt-blown nonwoven filter media on both initial and dynamic filtration properties using micron-sized particles.

Investigating particle deposition is another aspect to study the effect of the basis weight of melt-blown nonwoven filter media on filtration performance. Thomas [5] and Leung [6] reported exponential decay of particle deposition from filter surface to filter bottom of filter media with compact structures with modeling. Thomas [5] also used adhesive tapes to collect particle mass at different spots across the filter depth. However, a more accurate and quantitative method is

recommended to be applied to study the particle deposition. As traditional structure characterization methods, e.g. optical microscopy [7], scanning electronic microscopy (SEM) [8], digital volumetric imaging (DVI) [9], have to deform the filter structure during sample preparation, the XMCT becomes a competitive candidate for non-invasive 3D structural characterization of particle-loaded melt-blown nonwoven filter media. Jackwicz studied the particle movement under steady-state filtration [10], Riefer reported the particle penetration across filter depth [11]. However, both of them haven't separated the particles from the whole filter structure, and the effect of basis weight on particle deposition remains undiscovered.

In this study, we load standard dust particles to melt-blown nonwoven filter media with different basis weight to evaluate the effect of basis weight on dynamic filtration properties. We also send melt-blown nonwoven filters with different basis weight but captured the same mass of particles to XMCT for further filter structure and particle deposition analysis to evaluate the effect of basis weight on particle deposition.

4.2.Materials and Methods

4.2.1. Meltblown filter media sample production

The melt-blown nonwoven filter media used in this study was produced using Reicofil® (Reifenhauser, Germany) melt-blown equipment at The Nonwovens Institute. Metocene 650W Polypropylene (LyondellBasell, Netherlands) with a 500 g/10min melt flow rate and 0.946 g/cm^3 density was used as the raw material. throughput for all samples was 0.9 g/hole/min. The die-to-collector distance was kept at 300 mm. The same 500 m^3/hr airflow was used for these samples during production, and the basis weight was the only variable in this research.

4.2.2. Filter media characterization

The fiber diameter of studied melt-blown nonwoven filter media was measured based on scanning electronic microscope (SEM) images and an average value was calculated to represent the fiber diameter of all the samples because of the same airflow. The SEM images were taken on a Phenom SEM (Thermo Fisher Scientific, U.S.). Two straight lines perpendicular to each other were drawn on each SEM image, and all fibers crossed these two straight lines (> 200 fibers) were measured for the fiber diameter in a total of 10 SEM images for each sample. Details of melt-blown fiber diameter measurement are discussed in section 4.3.1. Fiber diameter and other structural properties of the studied filter MB are listed in Table 4.1.

The basis weight of samples used in this study was measured according to ASTM 3776 Standard Test Methods for Mass Per Unit Area (Weight) of Fabric. The mass of 5 sample replicates, each with a 100 cm^2 area, were measured for each sample.

The thickness was measured according to ASTM D 1777 Standard Test Method for Thickness of Textile Material by a thickness gauge with a low pressure of 15 Pa applied. 10 test replicates were measured for each sample.

The filter solidity (fiber packing density) is a parameter to evaluate the compactness of the porous structure. It was calculated according to the following formula:

$$Sf = \frac{m}{H*\rho}, \quad (4.1)$$

where m is the sample mass, H is the sample thickness, and ρ is the PP density.

The pore diameter distribution was measured using PMI liquid capillary porosimetry (Porous Materials Inc., U.S.).

4.2.3. Particle loading process

The Palas MFP 3000 Filter Tester Rig (Palas GmbH, Germany) was used to load solid particles and to analyze the particle loading behaviors of melt-blown nonwoven filter media. This equipment could measure the dynamic change of differential pressure and filtration efficiency during continuous solid particle loading to the test sample. It consisted of a rotating brush particle generator (RBG 1000), a particle counting system (Welas 3000) with both upstream and downstream optical particle counter (2070 sensor, 0.3 µm to 17 µm), a differential pressure detector, a test filter holder, a gravimetric filter holder, and a suction pump, as shown in Figure.4.1.

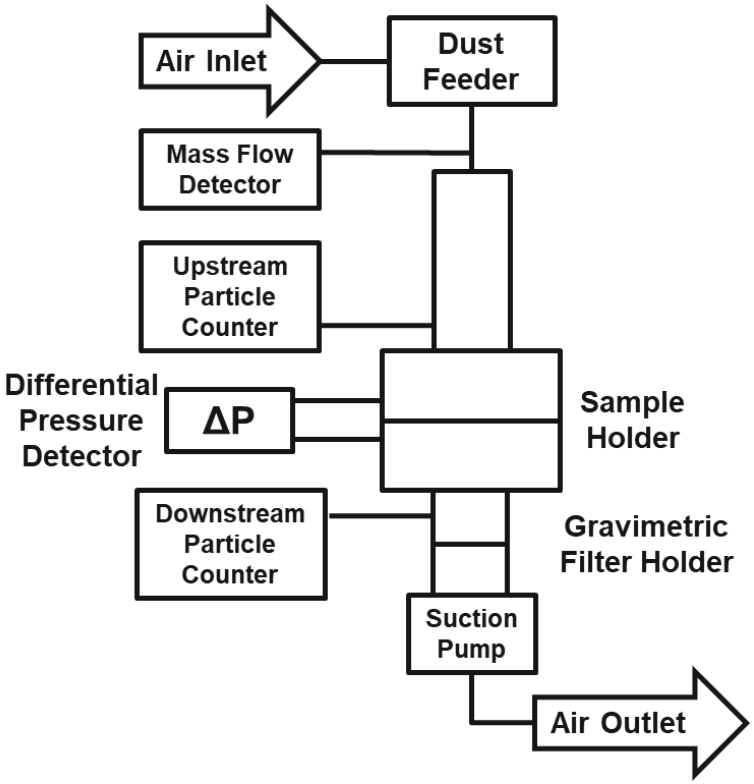

Figure.4.1. Equipment set-up for particle loading test.

Clean air was fed to the system. The piston containing solid particles was pushed upward at a constant speed so the particle feeding rate could be kept constant. The particles were then continuously generated by the rotating brush and fed through the air stream. As the particles were loading to the test filter and penetrating the test filter, the particle number before the penetration, p_1, was measured by the upstream particle counter. The particle number after the penetration, p_2, was measured by the downstream particle counter. The overall numerical efficiency, E, could then be calculated according to the following equation:

$$E = \frac{p1-p2}{p1} . \quad (4.2)$$

Meanwhile, the pressure drop across the test filter was measured by the differential pressure detector continuously. The test sample holder had a circle shape with an area of 100 cm^2, so the loaded area of the test filter was kept the same. All the penetrated particles would then be captured by the gravimetric filter to protect the testing system.

Three individual measurements were carried out under the same testing condition of 20 cm/s air face velocity, 120 L/min air flow rate and 200 mg/m^3 particle concentration. The ISO 12103-1 Arizona Fine Test Dust (manufactured by Power Technology Inc., USA), standard test dust containing 70% of silica in terms of mass, was used in the testing. It has a nominal size of 0 to 80 μm. Volume-based particle size distribution also indicates its bimodal distribution with two peaks at around 4 μm and 20 μm.

4.2.4. 3D structure acquisition of particle-loaded melt-blown filter media

XMCT was used for 3D imaging and 3D structure characterization of particle-loaded melt-blown nonwoven filter media to study the nonwoven structures and particle deposition distribution across

the filter depth. Samples respectively with 100 g/m^2, 150 g/m^2, and 200 g/m^2 basis weight were loaded with different the same mass, 5g/m^2 of dust particles. Then these samples were scanned at the University of Texas High-Resolution X-ray Computed Tomography Facility using the Xradia 400 system (Zeiss, Germany). The number of tomograms or image slices was 611, 680, and 723 respectively for sample BW-100gsm-5g, BW-150gsm-5g, and BW-200gsm-5g.

X-ray source with 10 W and 90 kV photon energy was used for the scans. To visualize and analyze particles larger than 1 µm that occupied the major mass and volume, the resolution was set up as 1 µm/pixel. The scanned spatial volume was thereafter limited to 1000 µm*1000 µm*1000 µm. Samples with a dimension of 3 mm*3 mm were cut from the particle-loaded filter samples so that the scan zone in the center of the samples was not affected by the deformation due to sample cutting on the outer edges.

4.2.5. Image processing and 3D structure characterization

The image processing procedures of XMCT tomograms are shown in Figure.4.2, where the image processing software Avizo® was used. After the image slices or tomograms as shown in Figure.4.2 a were imported to Avizo, the whole image slice set could be processed simultaneously. Denoising process with a combination of median filter and closing process (dilation then erosion) was applied to remove the background noises of original image slices in Figure.4.2 b. This closing process was used to reduce the fact that some inner parts of fibers exhibited low gray values which were very close to those of pores. This fact was caused by the reflection of X-ray photons of the curved fiber surfaces [10]. The research of interest area was then resized by cropping the denoised image slices in Figure.4.2 c, then image slices with 660*660 pixel^2 area in Figure.4.2 d were obtained.

The segmentation process was then applied to separate the fibers and particles of the 3D structure of particle-loaded samples. Due to the different attenuation rates of these two substances caused by different material density and material thickness, fibers had medium gray value, while particles had ultra-high gray value, which corresponded to the gray area and bright area respectively in the image slices from Figure.4.2 b to Figure.4.2 d. The brightness and contrast of these image slices were increased for better visualization. In this study, the thresholding tool was used to choose the threshold range of gray value to determine and select the target substance within that threshold range. Manual processing was also applied to select the low gray value inner parts of fibers in case these parts were not removed by the closing process and were determined as pores. After the segmentation, the original image slices with a wide range of gray values were segmented into the fiber (red) and particle (green) as shown in Figure.4.2 e. Then individual fiber volume Figure.4.2 f and particle volume Figure.4.2 g were generated from the segmented image slices by the volume rendering process. A 3D loaded filter structure Figure.4.2 h could also be visualized by combing the segmented fiber volume and the particle volume together using the software Avizo.

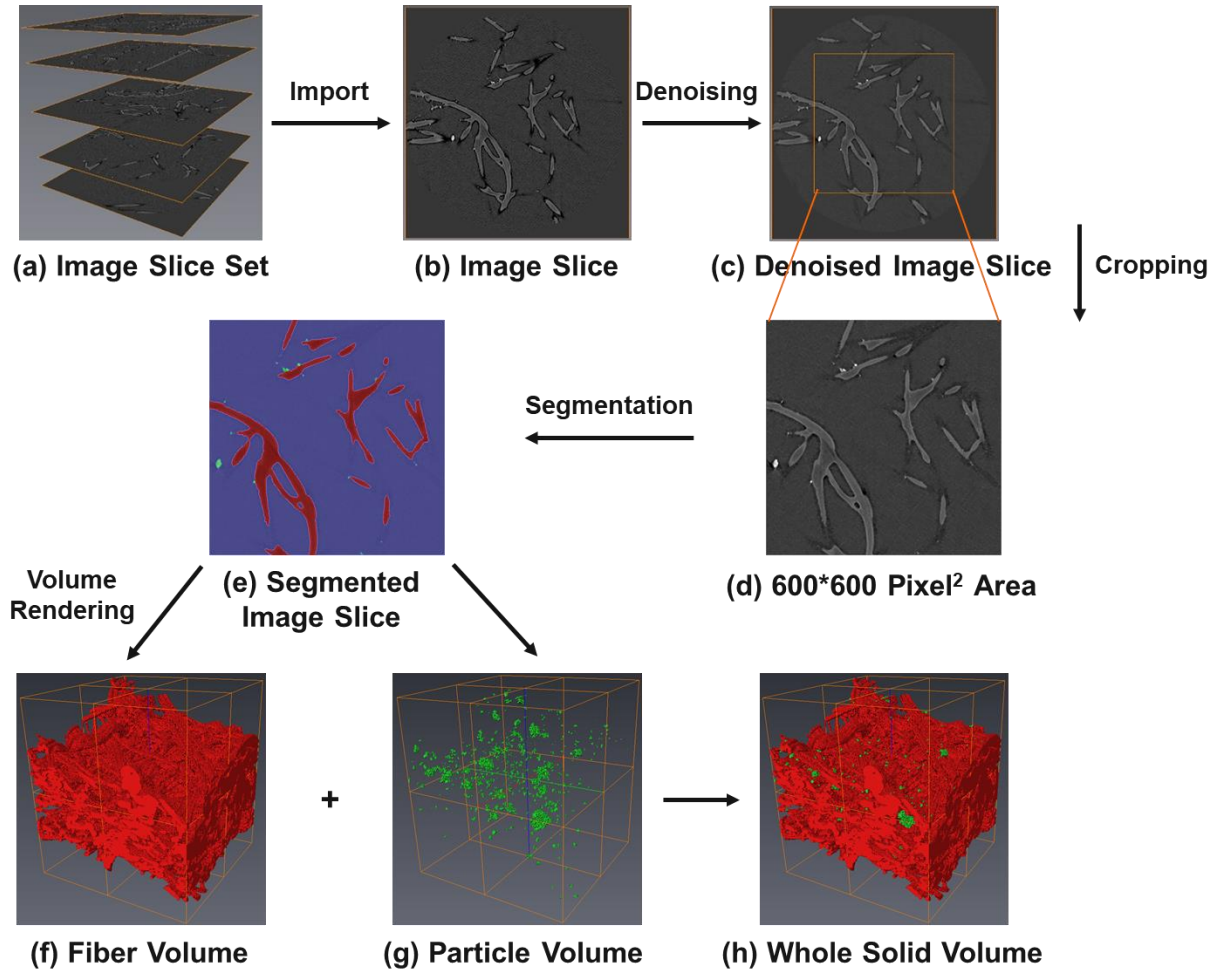

Figure.4.2. Image processing and image analysis procedures.

4.3. Results and discussion

4.3.1. Characterization of structure properties

Structure properties of the studied melt-blown nonwoven filter media were characterized, and the structure information was listed in Table 4.1. Figure.4.3 expresses the surface observation of sample BW-100gsm. The fiber diameters were measured with the method mentioned in section 4.2.2. For these samples produced with 500 m^3/hr airflow, 204 fibers were measured, and the average fiber diameter was 10.86 μm as displayed in Figure.4.3 b. The filter solidities of samples

were calculated according to equation 4.1 based on the basis weight and filter thickness from the measurement. These measured fiber solidity values were 10.37%, 14.67%, and 18.18% respectively. An evident increase in filter solidity existed with the increase of filter basis weight. The pore diameter distributions of filter samples with different basis weight are illustrated in Figure.4.3 c. The average pore diameter was 32.30, 24.84, and 18.11 respectively, which increased with the increase of filter basis weight.

Table 4.1. Structure properties of melt-blown filter media with different basis weight.

	BW-100gsm	BW-150gsm	BW-200gsm
Average Fiber Diameter (μm)	10.86 ± 4.04	10.86 ± 4.04	10.86 ± 4.04
Median Fiber Diameter (μm)	11.06	11.06	11.06
Basis Weight (g/m^2)	96.8 ± 3.3	146.2 ± 6.3	194.6 ± 1.5
Filter Thickness (μm)	986.8 ± 13.9	1053.7 ± 19.0	1131.3 ± 20.8
Filter Solidity (%)	10.37	14.67	18.18
Average Pore Diameter (μm)	32.30 ± 1.78	24.84 ± 1.97	18.11 ± 0.23

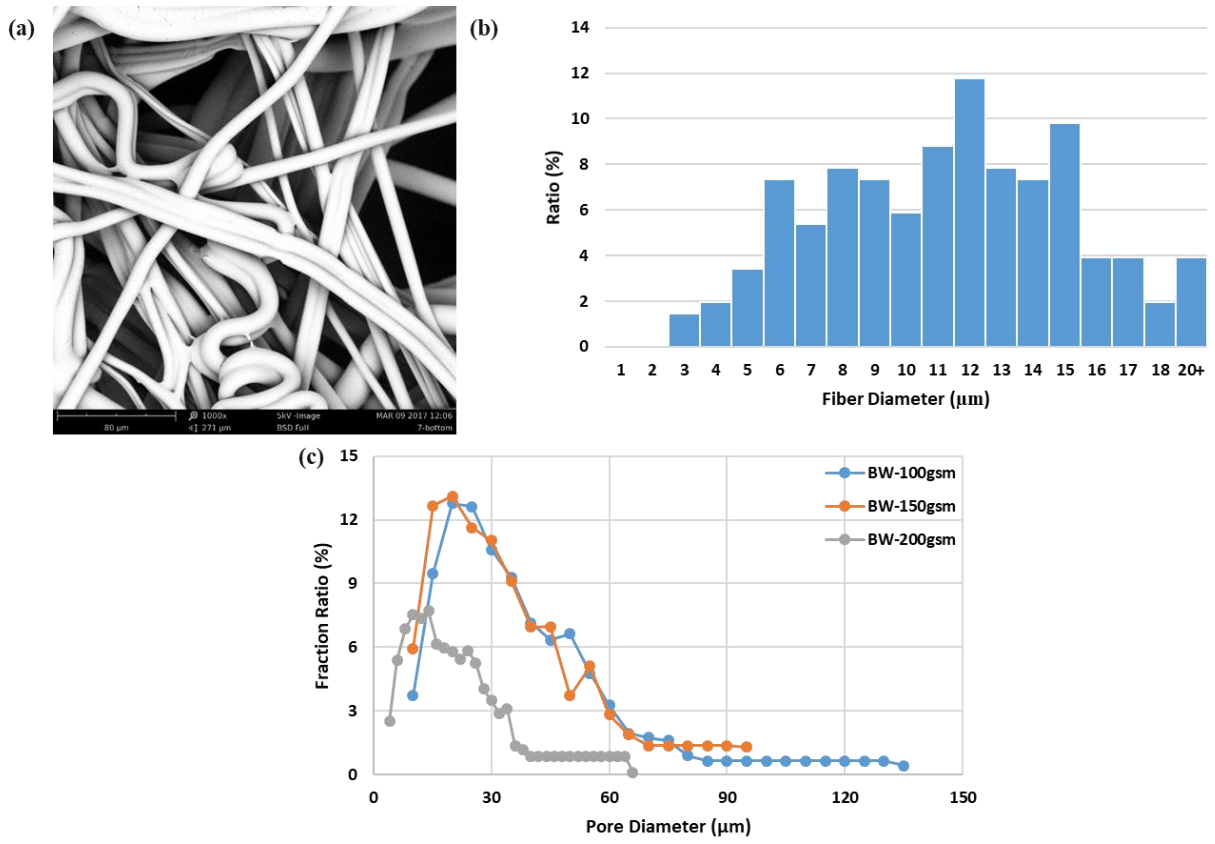

Figure.4.3. Structure properties of melt-blown filter media with different structure compactness: (a) SEM image, (b) fiber diameter distribution, and (c) pore diameter distribution.

4.3.2. Particle loading behaviors

Meltblown filter media samples, BW-100gsm, BW-150gsm, and BW-200gsm, were loaded with standard dust particles using the equipment and test condition described in section 4.2.3 to study the effect of the basis weight of melt-blown filter media on particle loading behaviors. Figure.4.4 indicates that filter with a lower basis weight had a lower pressure drop increase during continuous particle loading, which is ideal for extending the filter lifetime. Figure.4.4 b presents that filter with a higher basis weight had a higher filtration efficiency over time, which means higher basis

weight enables to increase not only the initial filtration efficiency but also the dynamic filtration efficiency during filtration. However, the quality factor in Figure.4.4 c expressed that filter with higher basis weight had lower comprehensive performance, considering both the filtration efficiency and pressure drop. In this case, the dynamic quality factor here in this research and initial quality factor in literature is in agreement that the benefit of the increase in filtration efficiency from high basis weight could not overcome the disadvantage of the decrease in pressure drop. The quality factor QF was calculated from the following equation 4.3 [Brown 1993/Leung 2012].

$$\mathrm{QF} = \frac{-\ln(1-E)}{\Delta \mathrm{P}}, \quad (4.3)$$

where E is the filtration efficiency, and ΔP is the pressure drop.

Besides, Figure.4.4 d indicates that filter with lower basis weight had higher dust holding capacity at the end of the test with 500 Pa pressure drop. This might be attributed to the loose structure, because both the filter solidity and average pore diameter of low basis weight filter were lower, as listed in Table 4.1.

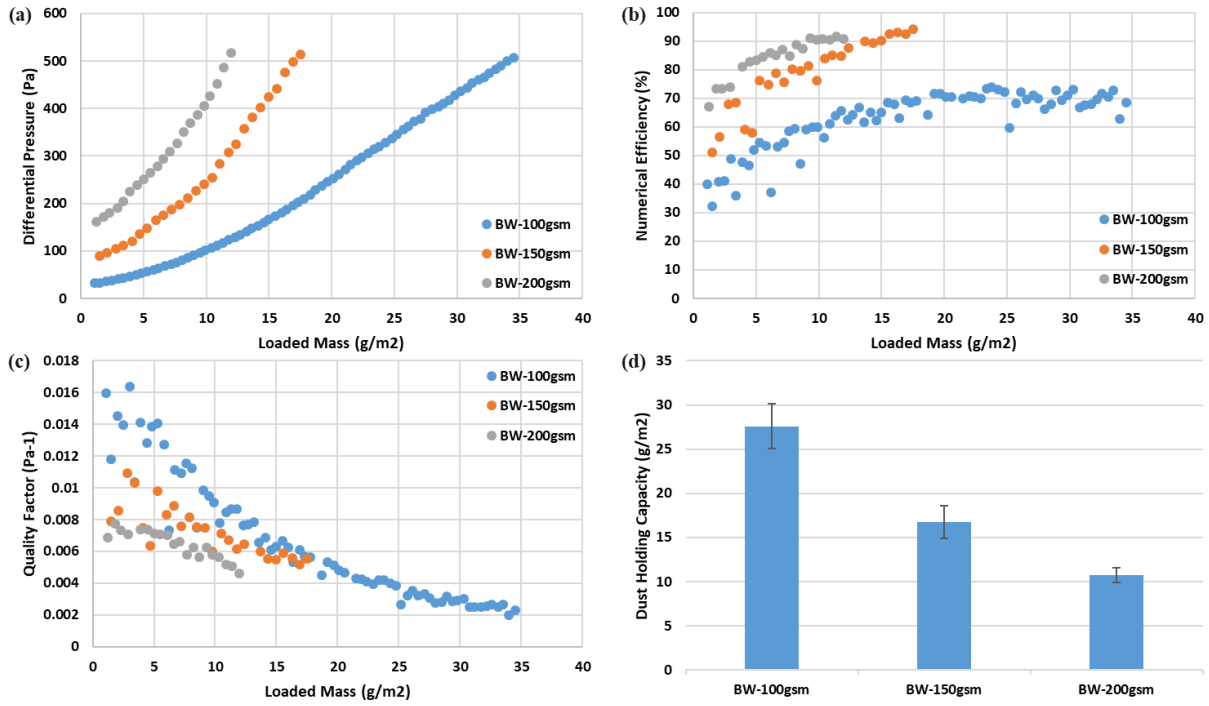

Figure.4.4. Effect of structure compactness on particle loading behaviors. (a) differential pressure vs. loaded mass, (b) number efficiency vs. loaded mass (c) quality factor vs. loaded mass, and (d) dust holding capacity at the end 500 Pa differential pressure.

4.3.3. 3D structure visualization of particle-loaded filters

Despite particle loading experiments, XMCT was used to investigate the effect of the basis weight of melt-blown nonwoven filter media on filtration properties. Filter samples were sent to the XMCT scan with the scan condition mentioned in section 4.2.4. The acquired 3D image slice sets were processed following image processing procedures described in section 4.2.5. 3D structures of these filters, BW-100gsm-5g, BW-150gsm-5g, and BW-200gsm-5g, are displayed respectively in Figure.4.5 a, Figure.4.5 b, and Figure.4.5 c.

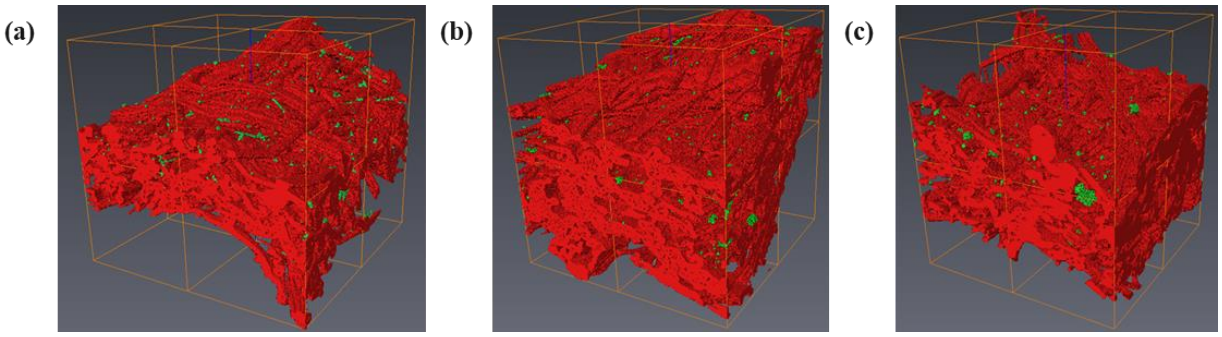

Figure.4.5. 3D meltblown nonwoven filter media structures respectively captured 5g/m^2 dust: (a) BW-100gsm, (b) BW-150gsm, and (c) BW-200gsm.

From these 3D images, it is obvious that these melt-blown filter samples had a textured structure, which is estimated to be caused by the texture of forming belt during production. The special image processing approach illustrated in Figure.4.6 was applied to get rid of such textured structures that may affect the analysis of filter structure and particle deposition profile. A 3D structure was first divided into 16 equal individual units in Figure.4.6 b. If there was only air or pore on the top section or bottom section of that unit, the top section or bottom section would be cropped as shown in Figure.4.6 c. As a result of cropping, the thickness of the unit in Figure.4.6 c was lower than the original thickness in Figure.4.6 b. Then the unit was shifted up to form a reorganized 3D structure with reduced thickness and reduced influence from the original textured structure. The following two sections were discussed based on the results from reorganized structures.

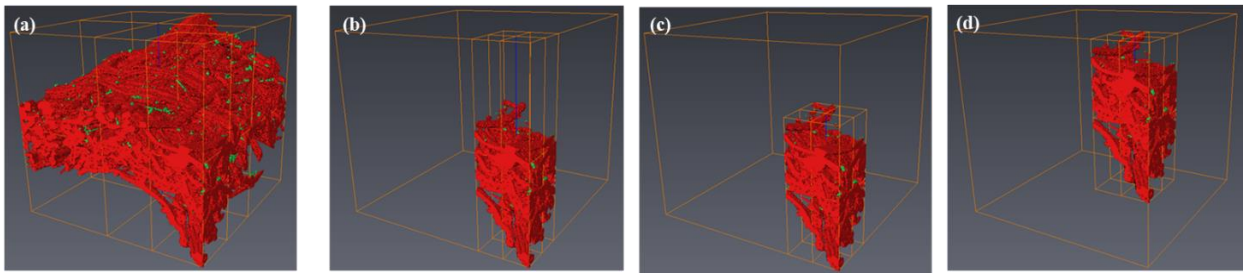

Figure.4.6. Image processing approach to acquire an adjusted structure despite the original textured structure: (a) original 3D structure, (b) 1 of the 16 divided equal individual part, (c) individual part with the top section cropped, (d) individual part being shifted up.

4.3.4. Analysis of filter structures

Following the image processing procedures described in section 4.2.5, the particle-loaded filter structure can be divided into the filter structure in Figure.4.2 f and particle deposition in Figure.4.2 g. As a result, the filter structure and particle deposition were analyzed individually in this section and the following section 4.3.5.

The filter solidity distribution across filter depth was presented in Figure.4.7. In the x-axis of Figure.4.7 a, 0 µm indicates the filter surface, and 611 µm indicates the filter bottom of sample BW-100gsm-5g. The disordered beginning segments of filter solidity distribution curves in Figure.4.7 illustrates that these three samples with different basis weight were influenced by the textured filter structures. In contrast, aligned beginning segments of filter solidity distribution curves in Figure.4.7 b explains the influence of textured structures were no longer existed by reorganizing the filter structure using the image processing approach in Figure.4.6. The heterogeneous filter solidity distribution of melt-blown nonwovens reported in the literature [12] can still be observed.

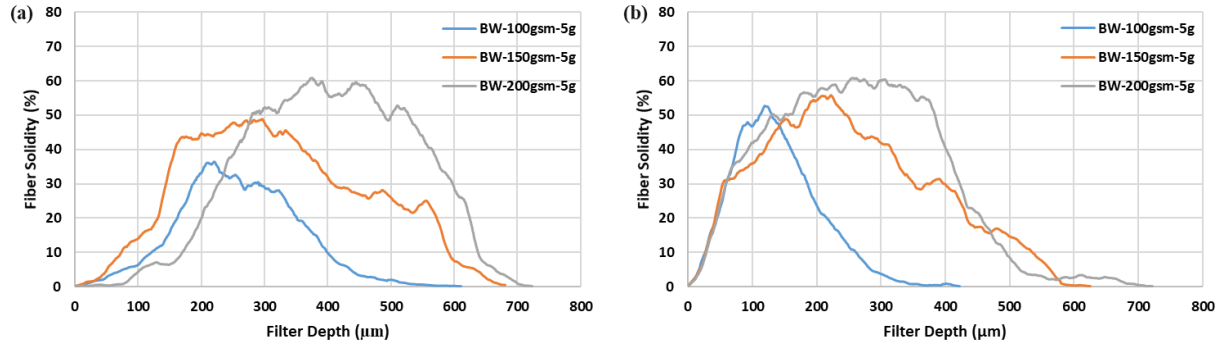

Figure.4.7. Fiber solidity distribution across filter depth of (a) original structures from imaging, (b) reorganized structures from imaging.

Thickness obtained from different methods were first compared in Figure.4.8 a. For filter samples, BW-100gsm-5g, BW-150gsm-5g, and BW-200gsm-5g, the thickness based on experimental measurement was 986 µm, 1053 µm, and 1131 µm respectively. It is a common thing that filter thickness increases with the increase of filter basis weight. However, this thickness from experimental measurement was overestimated due to the existence of textured filter structures. As each image slice from XMCT has 1 µm thickness, BW-100gsm-5g with 611 image slices indicates the 611 µm thickness from the original imaging structure. Furthermore, the reduced 422 image slices of the reorganized structure of BW-100gsm-5g mean the 422 µm thickness from the reorganized imaging structure. As described in section 4.3.3, the thickness of the reorganized imaging structure is less than that of the original imaging structure. However, sample BW-100gsm-5g had the most significant difference in thickness from the original and reorganized imaging structures, indicating filter with lower basis weight was easier to be affected by the belt and thus forming a more textured structure. Overall, the thickness from experimental measurements was much overestimated than that from imaging structures.

Furthermore, the filter solidities obtained from different methods were analyzed and compared in Figure.4.8 b. For example, the filter solidity of BW-100gsm-5g calculated following equation 4.1 using experimental data was 10.37%, which was underestimated due to the overestimated thickness. Besides, the average filter solidity from the filter solidity distribution curve in Figure.4.7 b was 12.86%, which was not accurate by considering the heterogeneous distribution. Following the same equation 4.1, the filter solidity of the same sample was 24.25% by replacing the experimental thickness with the thickness from the reorganized imaging structure. Interestingly, similar filter solidity values of 24.69% and 28.49% for BW-150gsm-5g and BW-200gsm-5g were obtained using the same method with thickness data from the reorganized imaging structures. These three close values of filter solidity further indicate a fact that an increase of filter basis weight only causes a slight increase in the structure compactness of melt-blown nonwoven filter media.

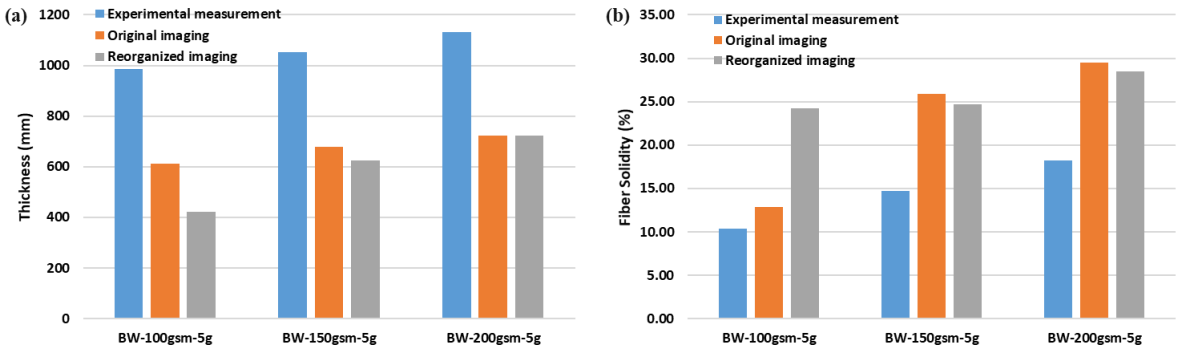

Figure.4.8. Comparison of (a) filter thickness and (b) filter solidity based on experimental measurements, original imaging structures, and reorganized imaging structures.

4.3.5. Analysis of particle deposition distribution

The particle deposition profiles are presented in Figure.4.9 in the form of particle solidity distribution curves across the filter depth. Particle solidity curves of filter samples, BW-100gsm-5g, BW-150gsm-5g, and BW-200gsm-5g, are presented in Figure.4.9 a. It can be found that a significant volume of particles was captured by around 250 μm depth beginning from the surface for all three samples. In other words, the rest part of these samples was not capturing many particles. This was further verified by the cumulative particle solidity curves in Figure.4.9 b. At 250 μm filter depth, 98.6%, 80.7% and 78.9% volume of particles were captured respectively by three studied samples.

Besides, dimensionless filter depth was calculated by dividing the number of each slice by the total number of slices. In this way, the particle solidity distribution across a relative dimensionless filter depth of each sample can be compared, as shown in Figure.4.9 c. It can be observed that particles were penetrating more deeply for filter BW-100gsm-5g, comparing with the other two filters. Because one peak of particle solidity can be found around 50% filter depth, while no significant peak can be observed after 40% filter depth of the other two filters. Figure.4.9 d further indicates that at the same dimensionless filter depth, more particles were captured by the filter with higher basis weight. This is ascribed to the higher thickness of the filter with a higher basis weight. For example, at 250 μm filter depth (39.9% filter depth and 34.6% filter depth respectively), 80.7% and 78.9% volume of particles were captured respectively by filter BW-150gsm-5g and filter BW-200gsm-5g, which was very close in volume. As a result, there is no doubt that filters with higher basis weight can capture more particles at the same dimensionless filter depth. Besides, the slightly higher filter solidity also contributes to a higher filtration efficiency of the same thickness, resulting in more particles capturing at the same dimensionless filter depth.

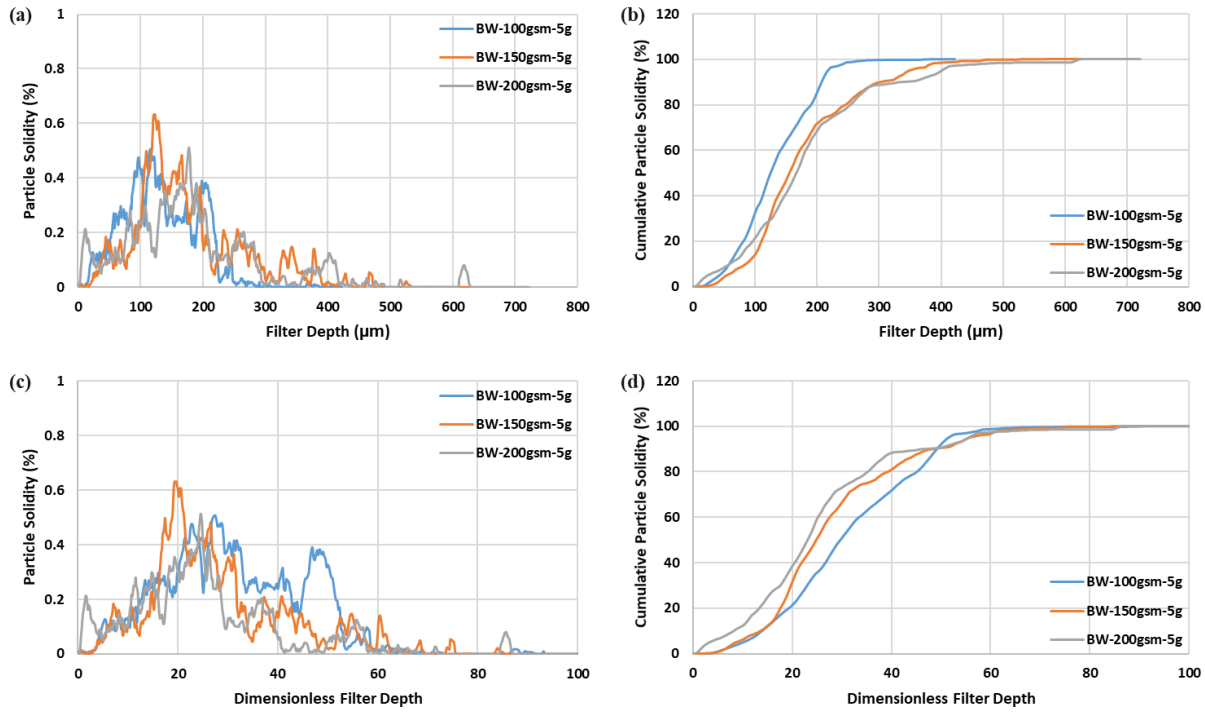

Figure.4.9. Particle solidity distribution of melt-blown nonwoven filter media with different basis weight loaded with the same 5 g/m^2 dust particles. (a) Particle solidity distribution across filter depth, (b) cumulative particle solidity across filter depth, (c) particle solidity distribution across dimensionless filter depth, and (d) cumulative particle solidity across dimensionless filter depth.

4.4. Conclusions

Meltblown nonwoven filter media with different basis weight were produced and loaded with standard dust particles for this study. It has been found that higher basis weight leads to faster pressure drop increase during filtration and lower dust holding capacity at the end of the test. Higher basis weight also leads to higher filtration efficiency over time, however, the increase in efficiency cannot compensate for the sacrifice in pressure drop.

The filter thickness obtained from experimental measurement is overestimated due to the textured structure of studied samples. A more accurate filter thickness can be acquired by reorganizing the 3D filter structure from XMCT imaging. The filter solidity data based on the measured basis weight and thickness from reorganized 3D imaging structure indicates an increase of filter basis weight only causes a slight increase in structure compactness.

Most of the particles are captured by a given thickness of a top part of the filter structure, despite the filter basis weight and thickness. The rest thickness of the filter is not contributing much to particle capturing. Besides, more particles are captured at the same dimensionless ratio of filter depth by filter with higher basis weight.

In one sentence, both the particle loading behaviors and particle deposition profiles are recommended to control and limit the basis weight of melt-blown nonwoven filter media for filter design if the desired filtration efficiency can be obtained.

References

[1] Hassan, M. A., Yeom, B. Y., Wilkie, A., Pourdeyhimi, B., & Khan, S. A. (2013). Fabrication of nanofiber meltblown membranes and their filtration properties. Journal of membrane science, 427, 336-344.

[2] Brown, R. C. (1993). Air filtration: an integrated approach to the theory and applications of fibrous filters. Pergamon.

[3] Leung, W. W. F., Hung, C. H., & Yuen, P. T. (2010). Effect of face velocity, nanofiber packing density and thickness on filtration performance of filters with nanofibers coated on a substrate. Separation and purification technology, 71(1), 30-37.

[4] Leung, W. W. F., & Hung, C. H. (2008). Investigation on pressure drop evolution of fibrous filter operating in aerodynamic slip regime under continuous loading of sub-micron aerosols. Separation and Purification Technology, 63(3), 691-700.

[5] Thomas, D., Penicot, P., Contal, P., Leclerc, D., & Vendel, J. (2001). Clogging of fibrous filters by solid aerosol particles experimental and modeling study. Chemical Engineering Science, 56(11), 3549-3561.

[6] Leung, W. W. F., & Hung, C. H. (2012). Skin effect in nanofiber filtration of submicron aerosols. Separation and Purification Technology, 92, 174-180.

[7] Jabri, W., Vroman, P., & Perwuelz, A. (2015). Study of the influence of synthetic filter media compressive behavior on its dust holding capacity. Separation and Purification Technology, 156, 92-102.

[8] Bourrous, S., Bouilloux, L., Ouf, F. X., Appert-Collin, J. C., Thomas, D., Tampère, L., & Morele, Y. (2014). Measurement of the nanoparticles distribution in flat and pleated filters during clogging. Aerosol Science and Technology, 48(4), 392-400.

[9] Shim, E., Pourdeyhimi, B., & Latifi, M. (2010). Three-dimensional analysis of segmented pie bicomponent nonwovens. The Journal of The Textile Institute, 101(9), 773-787.

[10] Jackiewicz, A., Jakubiak, S., & Gradoń, L. (2015). Analysis of the behavior of deposits in fibrous filters during non-steady state filtration using X-ray computed tomography. Separation and Purification Technology, 156, 12-21.

[11] Riefler, N., Ulrich, M., Morshäuser, M., & Fritsching, U. (2018). Particle penetration in fiber filters. Particuology, 40, 70-79.

[12] Ishikawa, T., Ishii, Y., Ohkoshi, Y., & Kim, K. H. (2019). Microstructural analysis of melt-blown nonwoven fabric by X-ray micro computed tomography. Textile Research Journal, 89(9), 1734-1747.

CHAPTER 5. Effect of Fiber Diameter and Die-to-Collector Distance (DCD) on the Loading Behaviors of Meltblown Nonwoven Filter Media

Abstract

Meltblown filter media with different fiber diameter and DCD were produced and loaded with standard micron-sized dust particles to investigate the effect of fiber diameter and DCD on particle loading behaviors during the filtration process. It was found that fine fiber and small DCD result in faster pressure drop increase, higher filtration efficiency, but the lower quality factor over time. Besides, it also caused lower dust holding capacity at the endpoint due to the more compact structure and smaller pore diameter.

Keywords: Meltblown nonwoven filter media, particle loading behavior, fiber diameter, die-to-collector distance (DCD)

5.1. Introduction

Meltblown is a common technology to produce fibrous filter media with fine fiber [1]. Many studies focused on the investigation of initial filtration properties of fibrous filter media, and limited studies regarding the dynamic filtration properties during the filtration process were reported. Leung [2] studied the loading behaviors mostly with electrospun nanofiber mats. Although melt-blown nonwoven filter media was also applied in his studies, the used particles were at a nanometer size that was not commonly existed. Jin et al. studied the effect of DCD on initial filtration properties [3] and the loading characteristics of gradient filters containing melt-blown layers [4], but the effect of melt-blown structure properties on dynamic filtration efficiency

remained undiscovered. Overall, it is needed to study the effect of structural properties of melt-blown filter media on the particle loading behaviors with micron-sized particles.

In this study, we have produced melt-blown nonwoven filter media with fiber diameter and DCD. Standard micron-sized dust particles are also loaded to the filter samples to investigate the effect of fiber diameter and DCD on particle loading behaviors.

5.2. Materials and Methods

5.2.1. Meltblown filter media sample production

The melt-blown nonwoven filter media used in this study was produced using Reicofil® (Reifenhauser, Germany) melt-blown equipment at The Nonwovens Institute. Metocene 650W Polypropylene (LyondellBasell, Netherlands) with a 500 g/10min melt flow rate and 0.946 g/cm^3 density was used as the raw material. throughput for all samples was 0.9 g/hole/min. The die-to-collector distance was kept at 300 mm. The airflow was controlled to study the effect of fiber diameter on particle loading behaviors, and different die-to-collector distance (DCD) values were selected to investigate the effect of DCD on the loading characteristics.

5.2.2. Filter media characterization

The filter media characterization methods regarding fiber diameter distribution, basis weight, thickness, filter solidity, and pore diameter distribution were the same as those mentioned in Chapter 4 section 4.2.2.

5.2.3. Particle loading process

The particle loading equipment and testing condition used in this study were the same as those described in Chapter 5 section 4.2.3.

5.3. Results and discussion

5.3.1. Effect of fiber diameter on particle loading behaviors

Meltblown samples produced with different airflow but the same DCD and basis weight were selected to study the effect of fiber diameter on particle loading behaviors. The fiber diameter distribution was measured with the method mentioned in Chapter 4 section 4.2.2. The magnification was kept constant as 500X for both SEM images. The SEM image and fiber diameter distribution of melt-blown filter media produced with 1,200 m^3/hr and 1,900 m^3/hr are shown in Figure.5.1. For samples produced with 1,200 m^3/hr airflow, 230 fibers were measured, and the average fiber diameter was 4.40 μm. For samples produced with 1,900 m^3/hr airflow, 312 fibers were measured, and the average fiber diameter was 2.82 μm.

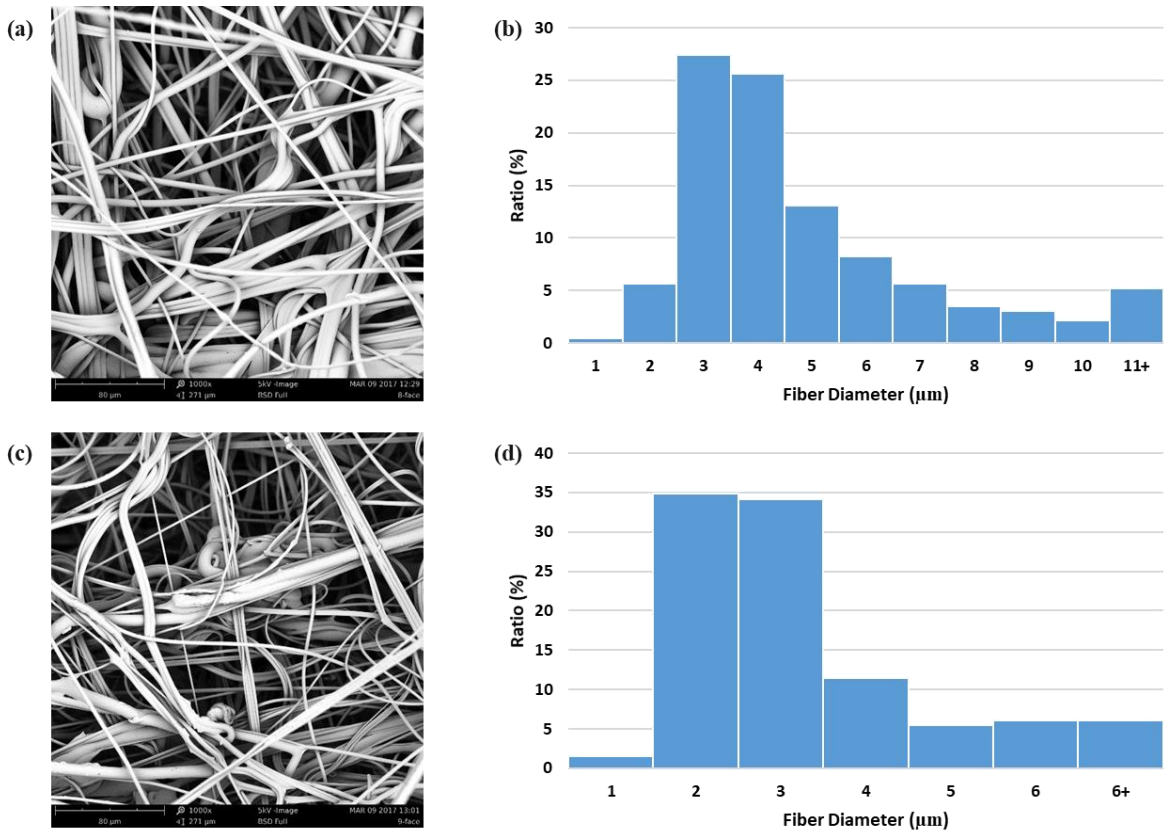

Figure.5.1. SEM image and fiber diameter distribution of meltblown filter media produced with (a), (b) 1,200 m^3/hr, and (c), (d) 1,900 m^3/hr airflow.

The structure parameters of filter AF-1200m^3/hr and filter AF-1900m^3/hr are listed in Table 5.1. These two filters had very close fiber solidity (similar structure compactness), 10.68%, and 11.42% respectively, the same basis weight, but different fiber diameter. The more compact structure of AF-1900m^3/hr also corresponds to a smaller average pore diameter.

Table 5.1. Structure parameters of melt-blown filter media with different fiber diameters.

	AF-1200m^3/hr	AF-1900m^3/hr
Average Fiber Diameter (μm)	4.40 ± 2.47	2.82 ± 1.58
Median Fiber Diameter (μm)	3.64	2.33
Basis Weight (g/m^2)	53.8 ± 2.0	55.6 ± 1.1
Filter Thickness (μm)	532.6 ± 20.9	514.7 ± 16.9
Filter Solidity (%)	10.68	11.42
Average Pore Diameter (μm)	18.67 ± 0.05	15.79 ± 0.65

The comparison of their particle loading behaviors is shown in Figure.5.2. It can be found that the differential pressure of both melt-blown filter media increased along with the increase of loaded mass (Figure.5.2 a) during the particle loading process. AF-1900m^3/hr reached the maximum differential pressure earlier than the AF-1200m^3/hr, with fewer particles loaded. The number efficiency (Figure.5.2 b) increased as the particles were being loaded and then captured by the test filter. AF-1900m^3/hr had higher efficiency than AF-1200m^3/hr over time. The quality factor (Figure.5.2 c) indicates that AF-1900m^3/hr had better comprehensive performance over time, considering both efficiency and pressure drop. At the endpoint of the particle loading experiment, 500 a, the dust holding capacity (Figure.5.2 d) of AF-1200m^3/hr was higher than that of AF-1900m^3/hr.

From this comparison, it can be concluded that nonwoven filter media with smaller fiber diameter leads to faster pressure drop increase rate, higher efficiency during filtration over time, and lower dust holding capacity at the maximum pressure drop.

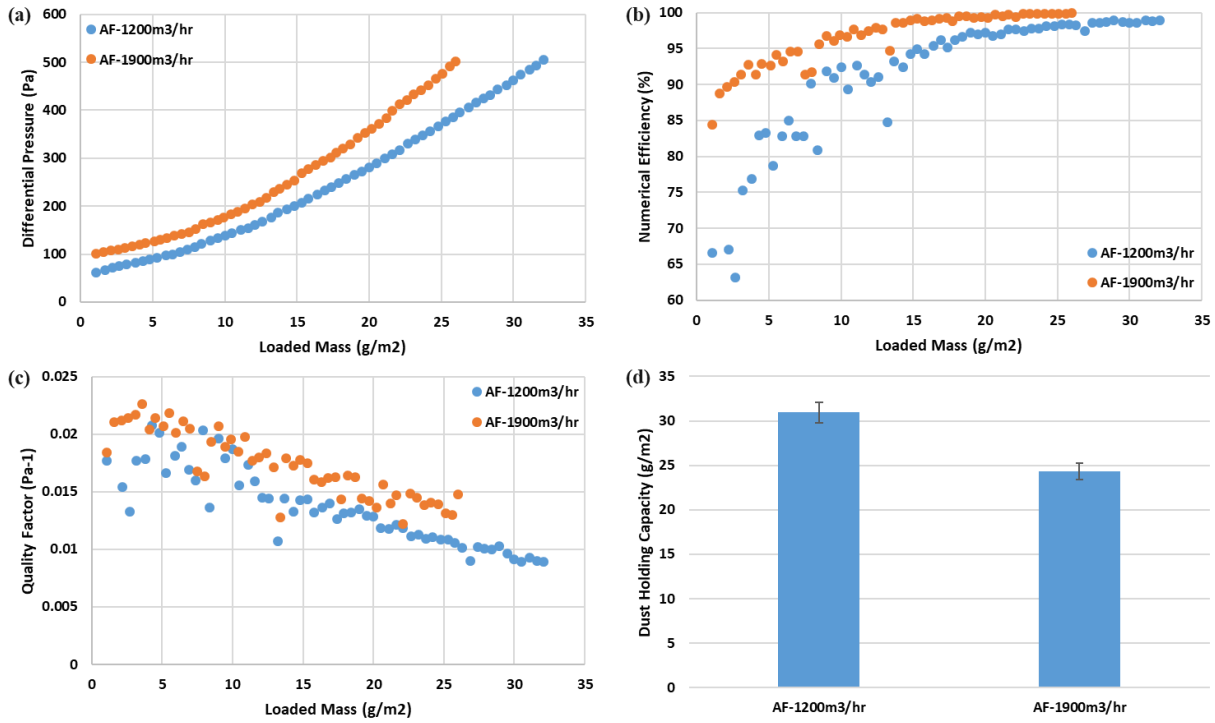

Figure.5.2. Effect of fiber diameter on particle loading behaviors. (a) differential pressure vs. loaded mass, (b) number efficiency vs. loaded mass, (c) quality factor vs. loaded mass, and (d) dust holding capacity at the end of 500 Pa.

5.3.2. Effect of DCD on particle loading behaviors

Meltblown nonwoven filter media used in this study had the same fiber diameter as the samples used in Chapter 4 due to the same airflow during production. The basis weight of these three samples was 100 g/m^2, and the only variable was the DCD. The structure parameters of these samples are listed in Table 5.2. It cannot be concluded that DCD did not affect filter solidity, although the filter solidity of these samples with different DCD was about the same. First, this is the opposite of the previous report [4]. Secondly, it is discovered from Chapter 4 that filters with 100 gsm basis weight and 10.86 μm average fiber diameter had textured structures caused by the

forming belt during production. As a result, the filter solidity data here were not accurate. However, there is no doubt that higher DCD led to a larger average pore diameter due to the longer fiber deposition time.

Table 5.2. Structure parameters of melt-blown filter media with different DCD.

	DCD-150mm	DCD-300mm	DCD-400mm
Average Fiber Diameter (μm)	10.86 ± 4.04	10.86 ± 4.04	10.86 ± 4.04
Median Fiber Diameter (μm)	11.06	11.06	11.06
Basis Weight (g/m^2)	97.4 ± 4.8	96.8 ± 3.3	96.8 ± 3.3
Filter Thickness (μm)	993.5 ± 20.4	986.8 ± 13.9	1024.9 ± 24.7
Filter Solidity (%)	10.36	10.37	10.13
Average Pore Diameter (μm)	22.31 ± 1.19	32.3 ± 1.78	41.83 ± 3.27

Figure.5.3. illustrates the particle loading behaviors of studied melt-blown nonwoven filter media with different DCD. It can be found that higher DCD led to a slower pressure drop increase, as shown in Figure.5.3 a. Interestingly, the significant difference in average pore diameter had not led to significant differences in filtration efficiency, but the filter with lower DCD still had a higher efficiency over time according to Figure.5.3 b. Figure.5.3 c shows that filters with higher DCD had the highest quality factor over time. Besides, the filter with the highest DCD had the highest dust holding capacity at 500 Pa.

In conclusion, nonwoven filter media with higher DCD leads to slower pressure drop increase, lower filtration efficiency over time, and higher dust holding capacity at the end.

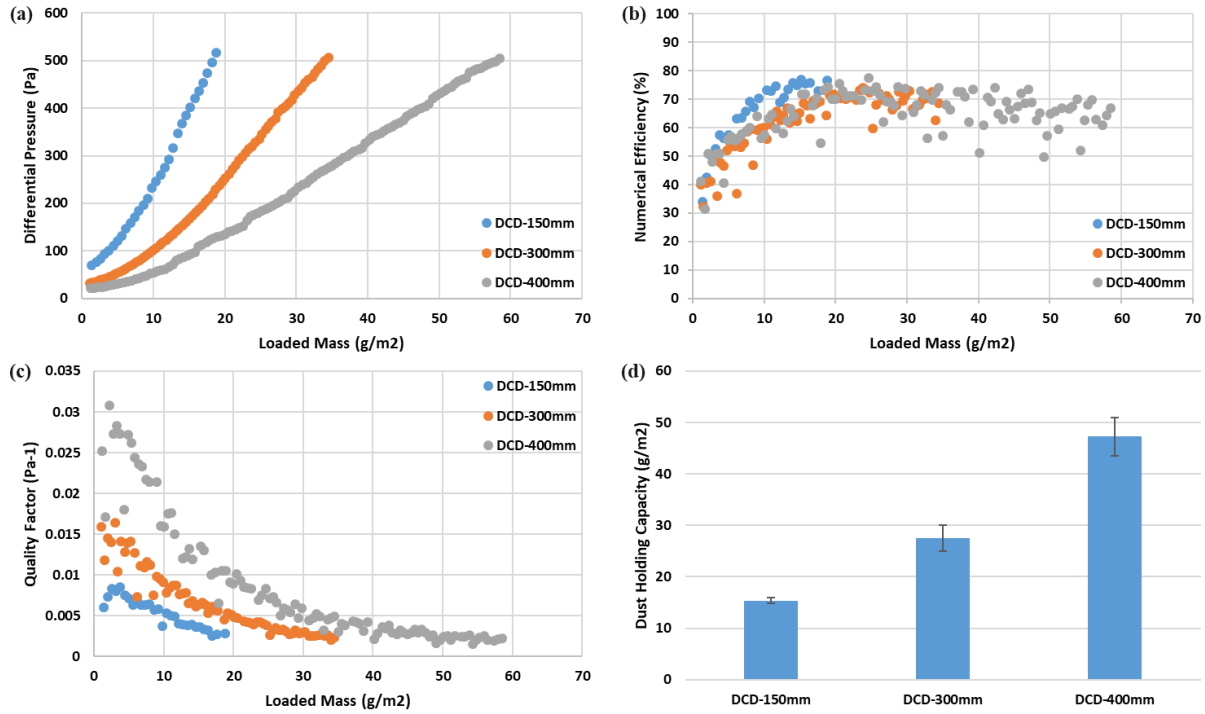

Figure.5.3. Effect of DCD on particle loading behaviors. (a) differential pressure vs. loaded mass, (b) number efficiency vs. loaded mass, (c) quality factor vs. loaded mass, and (d) dust holding capacity at the end of 500 Pa.

5.4. Conclusions

Fine fiber and small DCD result in faster pressure drop increase, higher filtration efficiency, but the lower quality factor, and lower dust holding capacity at the endpoint due to the more compact structure and smaller pore diameter.

References

[1] Hassan, M. A., Yeom, B. Y., Wilkie, A., Pourdeyhimi, B., & Khan, S. A. (2013). Fabrication of nanofiber meltblown membranes and their filtration properties. Journal of membrane science, 427, 336-344.

[2] Leung, W. W. F., & Hung, C. H. (2008). Investigation on pressure drop evolution of fibrous filter operating in aerodynamic slip regime under continuous loading of sub-micron aerosols. Separation and Purification Technology, 63(3), 691-700.

[3] Zhang, H., Liu, J., Zhang, X., Huang, C., Zhang, Y., Fu, Y., & Jin, X. (2019). Design of three-dimensional gradient nonwoven composites with robust dust holding capacity for air filtration. Journal of Applied Polymer Science, 136(31), 47827.

[4] Zhang, H., Liu, J., Zhang, X., Huang, C., & Jin, X. (2018). Design of electret polypropylene melt-blown air filtration material containing nucleating agent for effective PM2. 5 capture. RSC advances, 8(15), 7932-7941.

CHAPTER 6. Overall Conclusions

- The clogging process of coarse nonwoven filter media is first reported here. At the beginning of the depth filtration stage, most of the particles are captured by the top part. After that, particles are deposited everywhere across the whole filter depth. During the transition from depth filtration to surface filtration, clogging of particle clusters with high solidity is first found in the bottom part. At the end of the transition stage, clogging of particle clusters is found in both the middle and bottom parts. The evolution of particle deposition indicates the bottom-top clogging process inside the structure of coarse nonwoven filter media, unlike the exponential decay of particle deposition of fine filter media.
- The increase of the basis weight of melt-blown nonwoven filter media leads to an increase in pressure drop increase rate, filtration efficiency over time, and a decrease in dust holding capacity at the endpoint. Considering the decrease in quality factor, the benefit of efficiency increase cannot compensate for the increase in resistance.
- Fabric solidity of melt-blown nonwoven with a textured structure is underestimated due to the overestimated thickness. A real fabric solidity with heterogeneous distribution can be obtained from X-ray micro-computed tomographic 3D imaging.
- Despite the basis weight of melt-blown nonwoven filter samples deposited with the same mass of particles, most of the particles are captured by a top part with certain depth (around 250 μm in this study), and the rest of the structure is not contributing to the mass capturing and filter lifetime. Besides, at the same ratio of filter depth, more particles are captured by the filter with a higher basis weight.

CHAPTER 7. Future Recommendations

- It is recommended to study the effect of filter structure properties, e.g. fiber diameter, filter solidity, fiber orientation distribution, pore diameter, etc., of coarse filter media under standard solid particle loading to investigate what determines the pressure drop increase rate in the depth filtration, transition, and surface filtration stages.
- The effect of the number of layers of coarse pre-filter and the protective effect of coarse pre-filter for gradient filters are studied in the Appendix. What is the role of filter structure properties of coarse filter media in this case? For these multilayered structures, every layer is capturing particles. What is the particle size distribution across the filter depth for a gradient filter, and how do the filter structural properties affect it?
- Electrostatic charging can increase the filtration efficiency of a filter without sacrificing its pressure drop. It is known that charging works effectively on small particles. Then would the electrostatic charging change the particle solidity distribution and particle size distribution across the filter depth?
- Electrospun nonwovens have been gradually commercialized. Should we apply it on top of the filer to work as a surface coating to enhance surface filtration? Can we use it on the bottom of the filter to increase the overall filtration efficiency?

APPENDIX

Characterization of the Loading Behaviors of Gradient Filter with Multilayered Pre-Filters

The particle loading experiments discussed in this section were carried out using the same equipment, Palas MFP 3000, as what was used in Chapter 3 and Chapter 4. The same testing conditions were also used with 20 cm/s air face velocity, 120 L/min airflow and 200 mg/m^3 particle concentration. However, unlike the Fine Test Dust (the A2 dust) used in Chapter 3 and Chapter 4, the standard dust particles used in this study were replaced with ISO 12103-1 Arizona Ultrafine Test Dust (the A1 dust).

In this study, carded/through-air bonded coarse filter (Pre-filter TA) and fine melt-blown filter (Filter MB) were produced and stacked together to fabricate gradient filters composed of multilayered coarse pre-filter(s) and one single layer of high-efficiency fine filter. The Pre-filter TA here is the Filter TA used in chapter 3 with a fiber diameter of 11.6 μm PP/14.3 μm Binder (70/30) and 5.36% fabric solidity. The Filter MB here is AF-1200m^3/hr used in Appendix section 1 with 4.40 μm average fiber diameter and 10.68% fabric solidity. The particle loading characteristics of Pre-filter TA and Filter MB are shown in Figure.A.1. As expected, comparing with coarse Pre-filter TA, fine Filter MB had a much faster pressure drop increase, much higher efficiency in both number and mass, but a much lower quality factor for the dynamic filtration properties. Besides, Filter MB had much lower dust holding capacity at the same differential pressure.

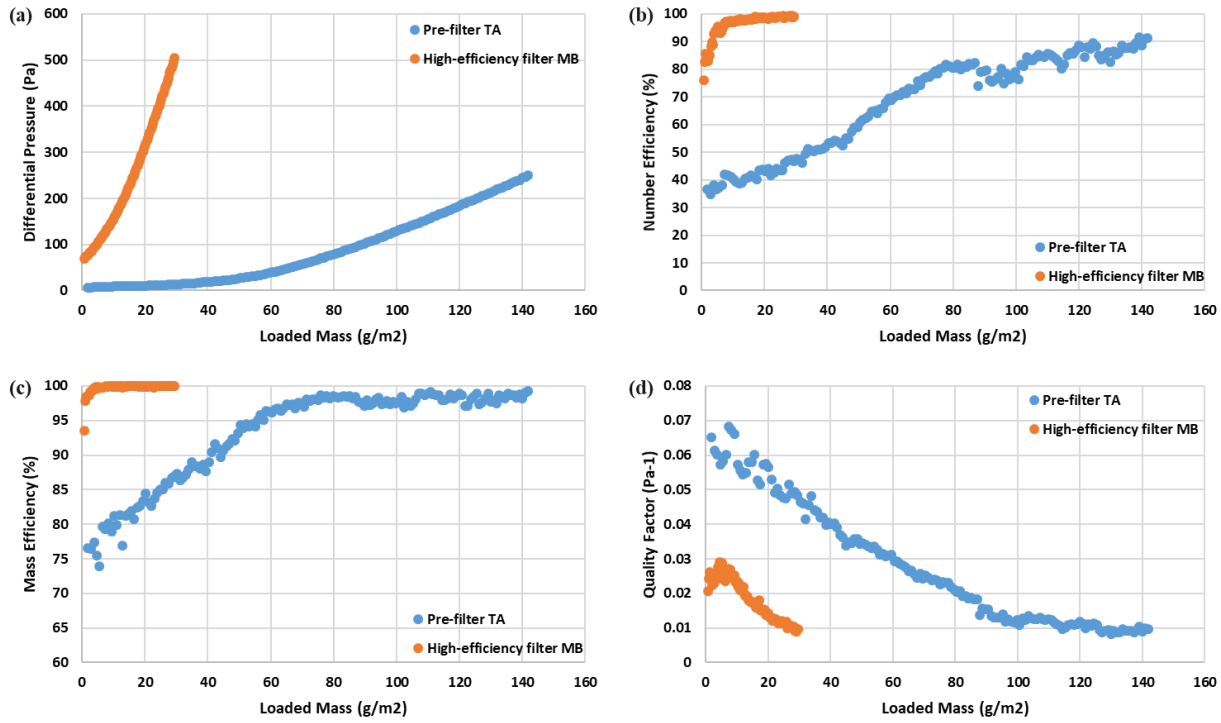

Figure.A.1. Comparison of the loading behaviors between single layer Pre-filter TA and Filter MB nonwoven filter media, (a) differential pressure vs. loaded mass, (b) number efficiency vs. loaded mass, (c) mass efficiency vs. loaded mass, (d) quality factor vs. loaded mass (based on number efficiency).

Then multilayered (2~4 layers) Pre-filter TA were stacked together, and their loading behaviors were displayed in Figure.A.2. Interestingly, the pressure drop increase rates were about the same for composite filters with a different number of layers. This can be explained by the mass captured by each layer. For 2-layer, 3-layer, and 4-layer composite filters, the dust holding capacity at 250 Pa were 107.4 gsm, 109.5 gsm, and 110.6 gsm respectively, which were about the same. Meanwhile, the top layer of each composite filter captured 90.52%, 90.09%, and 90.61% of the total loaded mass, while the whole structures respectively captured 94.29%, 95.22%, and 97.10%

of the total loaded mass. This indicates the fact that the top layer captured most of the particles and the layers on the bottom didn't play an important role in the dust holding capacity and filter lifetime. However, those layers on the bottom were still contributing to the efficiency in both number and mass, as presented in Figure.A.2 b and Figure.A.2 c. Besides, no significant difference in quality factors can be observed.

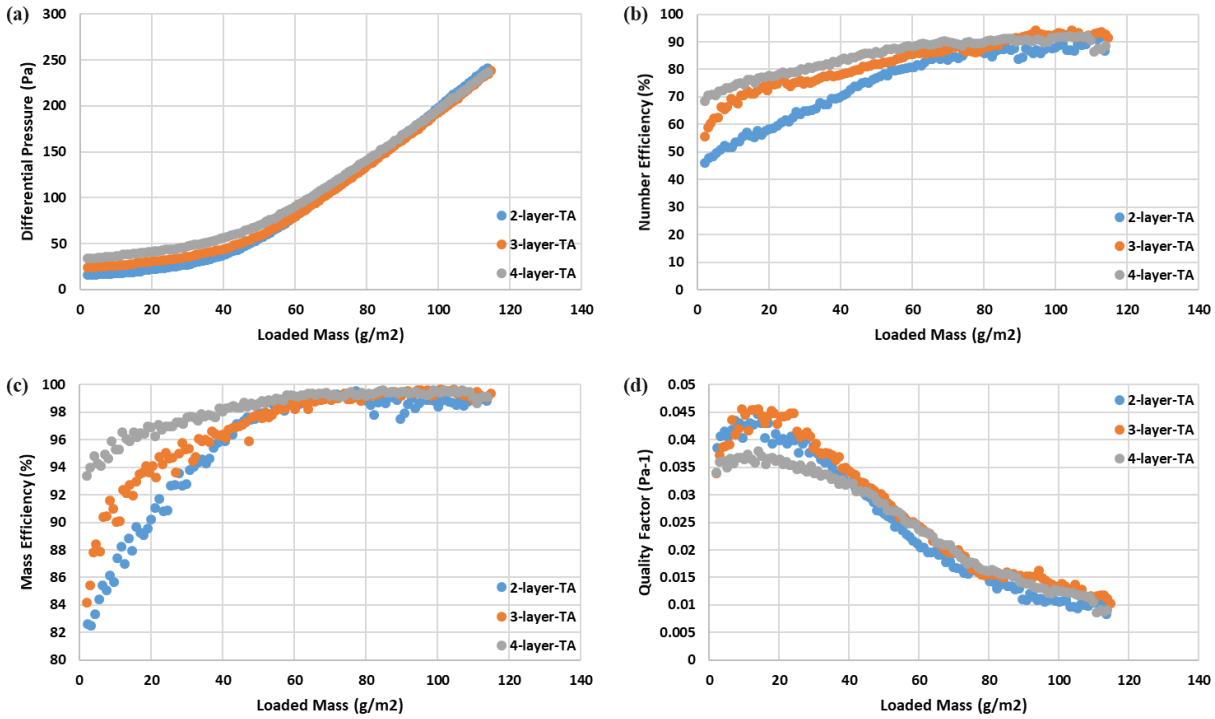

Figure.A.2. Loading behaviors of multilayered pre-filter TA, (a) differential pressure vs. loaded mass, (b) number efficiency vs. loaded mass, (c) mass efficiency vs. loaded mass, (d) quality factor vs. loaded mass (based on number efficiency).

Furthermore, the gradient filters composed of various layers of coarse Pre-filter TA and one single layer of fine Filter MB were fabricated and their particle loading behaviors were presented in

Figure.A.3. It is assumed that more layers of Pre-filter TA can increase both the initial filtration efficiency and pressure drop. However, the dynamic filtration properties during particle loading didn't work in the same way. Figure.A.3 indicated that gradient filter with more layers of Pre-filter TA had slower pressure drop increase, lower filtration efficiency, but higher dust holding capacity at 500 Pa. This can be explained by the protection role of a coarse Pre-filter TA. More layers of Pre-filter TA can capture more particles, as proved by Figure.A.2 b, then fewer particles were captured by the Filter MB in the bottom, which caused less clogging in Filter MB, leading to a slower pressure drop increase of the gradient filter. It also led to a lower filtration efficiency of the gradient filter, because the clogging of Filter MB could contribute a lot more than the clogging of Pre-filter TA to the efficiency. As a result, the gradient filter with only one-layer of Pre-filter TA had the lowest dust holding capacity due to the fastest clogging and pressure drop increase.

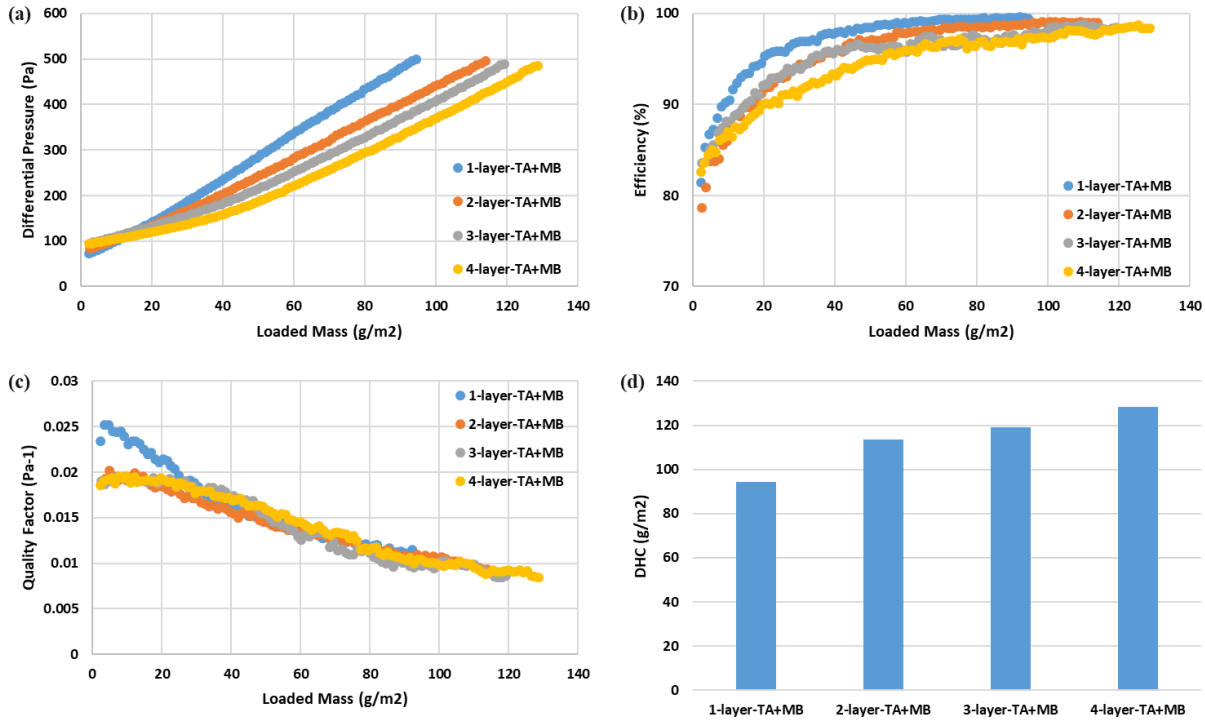

Figure.A.3. Loading behaviors of gradient filters composted of multilayered pre-filter TA and one single layer of MB, (a) differential pressure vs. loaded mass, (b) number efficiency vs. loaded mass, (c) mass efficiency vs. loaded mass, (d) quality factor vs. loaded mass (based on number efficiency).

Conclusions

For composite filter composed of multilayered coarse pre-filters, the number of layers of pre-filter has almost no influence in pressure drop increase, quality factor, and dust holding capacity, but it can increase the filtration efficiency in both number and mass. The top layer can capture most of the particles, and the layers on the bottom don't play an important role in the dust holding capacity and filter lifetime.

For gradient filter composed of multilayered coarse pre-filters and one single layer of fine melt-blown nonwoven, an increase of the number of layers of pre-filter leads to a decrease in pressure drop increase and filtration efficiency during particle loading but increase in dust holding capacity. This results from the protective effect of pre-filter while reducing the protection with a smaller number of layers of pre-filter lead to more particles being captured by the melt-blown and thus causing a higher degree of clogging.